

ENEA Ricerca Sistema Elettrico	Sigla di identificazione ADPFISI – LP2 - 107	Distrib.	Pag.	di
L	1	63		

Titolo

Advances in the development of the code FRENETIC for the coupled dynamics of lead-cooled reactors

Ente emittente Politecnico di Torino (CIRTEN)

PAGINA DI GUARDIA

Descrittori

Tipologia del documento: Rapporto Tecnico

Collocazione contrattuale: Accordo di programma ENEA-MSE su sicurezza nucleare e reattori di IV generazione

Argomenti trattati: Generation IV reactors

Sicurezza nucleare

Analisi di sicurezza

Sommario

The simulation of the dynamic behavior of lead-cooled fast reactors (LFRs) is a key step in the development of this innovative nuclear technology. To this aim, computational tools for the coupled neutronic/thermal-hydraulic description of the reactor core need to be developed. This task can be carried out at different levels of complication. Some codes are characterized by a highly detailed description of the system components, but they also require a high computational cost.

At Politecnico di Torino, the research group of nuclear engineering is developing the FRENETIC code for the dynamic simulation of LFR cores with closed hexagonal fuel elements at a reduced computational cost, suitable for parametric evaluations and simulations of safety-related transients. The code separately solves the neutronic and thermal-hydraulic model equations, with neutronic/thermal-hydraulic feedback introduced through a coupling procedure.

The work carried out during this year activity is focused on the following topics:

- further development and validation of the thermal-hydraulic module by introducing additional models for the treatment of hexagonal fuel assemblies of a specific geometry (the so-called "box-in-the-box" configuration) and the radial conduction in the fuel pin;
- development of the neutronic module by introducing a new decay-heat model;
- first coupled neutronic/thermal-hydraulic validation of the code against the shutdown heat removal tests performed on the Experimental Breeder Reactor-II of Argonne National Laboratory.

Note

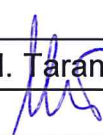
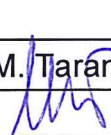
Riferimento CIRTEN: **CERSE-POLITO RL 1572/2015**

Autori:

Roberto Bonifetto, Dominic Caron, Sandra Dulla, Valerio Mascolino,
Piero Ravetto, Laura Savoldi, Domenico Valerio, Roberto Zanino (**POLITO-CIRTEN**)

Copia n.

In carico a:

2			NOME			
			FIRMA			
1			NOME			
			FIRMA			
0	EMISSIONE	24/09/15	NOME	M. Tarantino	NA	M. Tarantino
			FIRMA			
REV.	DESCRIZIONE	DATA	CONVALIDA	VISTO	APPROVAZIONE	



CIRTEL

Consorzio Interuniversitario per la Ricerca TEcnologica Nucleare

**UNIVERSITÀ
POLITECNICO DI TORINO**

Advances in the development of the code FRENETIC for the coupled dynamics of lead-cooled reactors

Autori

Roberto Bonifetto, Dominic Caron, Sandra Dulla, Valerio Mascolino,

Piero Ravetto, Laura Savoldi, Domenico Valerio, Roberto Zanino

CERSE-POLITO RL 1572/2015

TORINO, Agosto 2015

Lavoro svolto in esecuzione dell'Attività LP2. C1

AdP MSE-ENEA sulla Ricerca di Sistema Elettrico - Piano Annuale di Realizzazione 2014
Progetto B.3.1 “Sviluppo competenze scientifiche nel campo della sicurezza nucleare e collaborazione ai programmi internazionali per il nucleare di IV generazione”

Indice

Abstract	3
1 Introduction	4
2 Description of the EBR-II reactor and of the analyzed transients	5
2.1 The EBR-II reactor	5
2.2 The Shutdown Heat Removal Tests	8
2.2.1 SHRT-17	9
2.2.2 SHRT-45R	13
3 Development and validation of the thermal-hydraulic module	16
3.1 Implementations in the thermal-hydraulic module	18
3.1.1 Box-in-the-box model	21
3.1.2 Pin radial model	23
3.2 Results and discussion	25
3.2.1 Boundary conditions sets	26
3.2.2 Box-in-the-box results	29
3.2.3 Radial pin model results	39
3.3 Conclusions	44
4 Development of the neutronic module	45
4.1 Introduction	45
4.2 Decay heat model and methods of solution	45
4.3 Representative results	46
4.4 Conclusions	49
5 Preliminary validation of the coupled modules of FRENETIC	49
5.1 Steady state analysis	50
5.2 Transient results	53
5.3 Parametric study with the quasi-static method	55
5.4 Conclusions	58
6 Conclusions	58
7 References	59
8 Breve CV del gruppo di lavoro	61

Abstract

The simulation of the dynamic behavior of lead-cooled fast reactors (LFRs) is a key step in the development of this innovative nuclear technology. To this aim, computational tools for the coupled neutronic/thermal-hydraulic description of the reactor core need to be developed. This task can be carried out at different levels of complication. Some codes are characterized by a highly detailed description of the system components, but they also require a high computational cost.

At Politecnico di Torino, the research group of nuclear engineering is developing the FRENETIC code for the dynamic simulation of LFR cores with closed hexagonal fuel elements at a reduced computational cost, suitable for parametric evaluations and simulations of safety-related transients. The code separately solves the neutronic and thermal-hydraulic model equations, with neutronic/thermal-hydraulic feedback introduced through a coupling procedure.

The work carried out during this year activity is focused on the following topics:

- further development and validation of the thermal-hydraulic module by introducing additional models for the treatment of hexagonal fuel assemblies of a specific geometry (the so-called "box-in-the-box" configuration) and the radial conduction in the fuel pin;
- development of the neutronic module by introducing a new decay-heat model;
- first coupled neutronic/thermal-hydraulic validation of the code against the shutdown heat removal tests performed on the Experimental Breeder Reactor-II of Argonne National Laboratory.

1 Introduction

Several activities are ongoing in Europe and in particular in Italy around the development of the GenIV lead-cooled fast reactor (LFR) [1]. The main concepts which evolved over the years are those of the ELFR (the first-of-a-kind EU reactor) [2], of ALFRED (the EU demonstrator) [3] and of MYRRHA (the EU technology pilot plant) [4]. Indeed, Ansaldo Nuclear, ENEA and the Institute of Nuclear Research of Romania have signed at the end of December 2013 an agreement for the establishment of the Falcon Consortium (Fostering Alfred Construction), whose objective is to construct ALFRED in Romania.

Within that framework, the FRENETIC (Fast REactor NEutronics/Thermal-hydraulICs) code has been recently developed for the simulation of coupled neutronic/thermal-hydraulic transients in LFRs with the core arranged in hexagonal assemblies (HAs), enclosed in a duct [5]. The code has the ambition to provide fast approximate solutions for core design and/or safety analysis, and this thanks to the fact that the 3D problem is solved with a simplified approach. The neutronic (NE) module in FRENETIC solves the multigroup neutron diffusion equations with delayed neutron precursors using a nodal discretisation in space and a quasi-static discretisation in time. The thermal hydraulic (TH) module of FRENETIC solves the 1D (axial) mass momentum and energy conservations laws of the coolant, together with the 1D (axial) heat conduction equation in the fuel pins, in each assembly. The assemblies are then thermally coupled to each other on each horizontal cross section of the core, resulting in a quasi-3D model.

The work carried out in 2014 continues the development of this computational tool, following the previous steps carried out starting from the year 2011 [5, 6, 7, 8, 9]. The historical progress to the beginning of the period covered by the present report is summarised in Figure 1, while Figure 2 sketches the coupling strategy that has been adopted from the beginning of the project, allowing the possibility to perform separately the development and validation of the NE and TH modules.

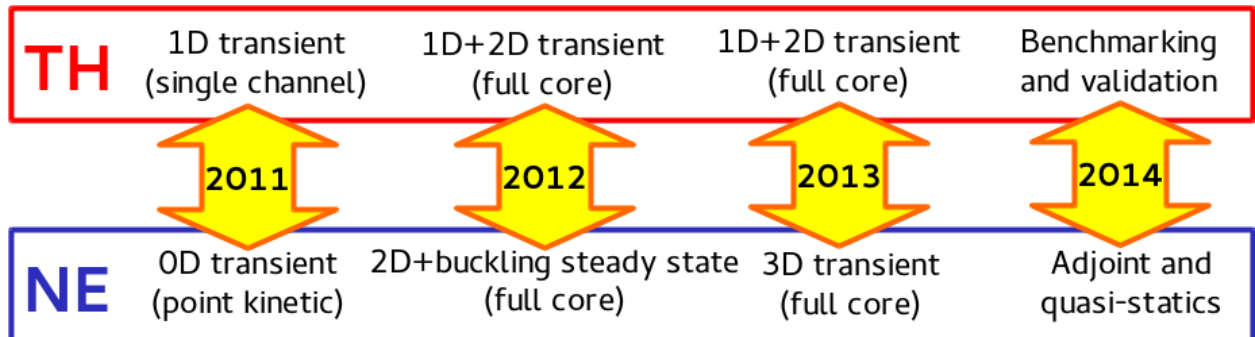


Figure 1. Evolution of the modelling capabilities of the FRENETIC code.

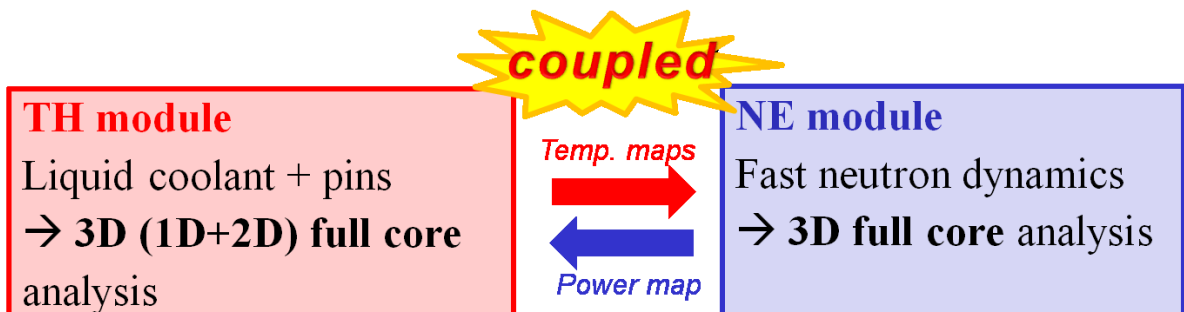


Figure 2. Coupling of the FRENETIC thermal-hydraulic and neutronic modules.

The work carried out during this year activity is focused on the following topics:

- further development of the thermal-hydraulic module by introducing additional models for the treatment of hexagonal fuel assemblies of a specific geometry (the so-called "box-in-the-box" configuration) and the radial conduction in the fuel pin, and prosecution of the validation activity [10, 11, 12] using data from the sodium-cooled Experimental Breeder Reactor-II (EBR-II) of Argonne National Laboratory;
- development of the neutronic module by introducing a new decay-heat model;
- first coupled neutronic/thermal-hydraulic validation of the code against the shutdown heat removal tests performed on the EBR-II.

In order to validate the FRENETIC code and due to the lack of experimental data from lead-cooled reactors, a series of transients regarding the EBR-II (sodium-cooled) reactor were analyzed within the framework of a multi-party benchmarking exercise coordinated by the IAEA [13].

2 Description of the EBR-II reactor and of the analyzed transients

The following section presents a brief description of the Experimental Breeder Reactor-II (EBR-II) and two of the Shutdown Heat Removal Tests (SHRTs), as these transients are assessed with the FRENETIC code in later sections of this report.

2.1 The EBR-II reactor

During 1944, scientists of the caliber of Fermi, Szilard and Wigner discussed the possibility of using nuclear energy not only for military purposes but also to light their cities [14]. It was not completely clear, at that time, what was the available quantity of fissile material on Earth. This coupled with the need of use as much as possible Uranium to develop atomic bombs, led this team of scientists to think of the possibility of designing a nuclear reactor able to produce more fissile materials than it consumed.

The chain of events led, in the frame of Argonne National Laboratories, to the birth of EBR-I in 1951. This reactor showed the feasibility of the breeding reactor concept and the possibility to control a chain reaction with a fast spectrum reactor with no moderation and sodium as a coolant.

The EBR-II was then conceived and the innovative features of the reactor were already clear at that time: the possibility to close the fuel cycle, coupling the reactor with a suitable reprocessing plant; the proliferation resistance of fuel irradiated in fast reactors, due to its very high radioactivity concentration.

The EBR-II reactor was a 62.5 MW_{th} (~20 MW_{el}) pool type sodium cooled reactor: all the primary components were submerged in the primary tank, containing approximately 340 m³ of sodium [13]. The upper plenum is at the same pressure for the whole reactor, while the inlet plenum is at different pressures with the inner core receiving sodium from the high-pressure plenum (~85 % of the total flow rate) while the outer blanket region received sodium from the low pressure plenum. Hot sodium mixes in the common upper plenum before going to the Intermediate Heat Exchanger (IHX) through a Z-shaped pipe (the so-called “Z-pipe”). Sodium exiting from the IHX feeds pumps again.

The intermediate loop conveys heat to the secondary system, to produce steam into a traditional Rankine cycle to feed a turbine and ultimately produce electricity. The system is shown and schematized in Figure 3 and Figure 4.

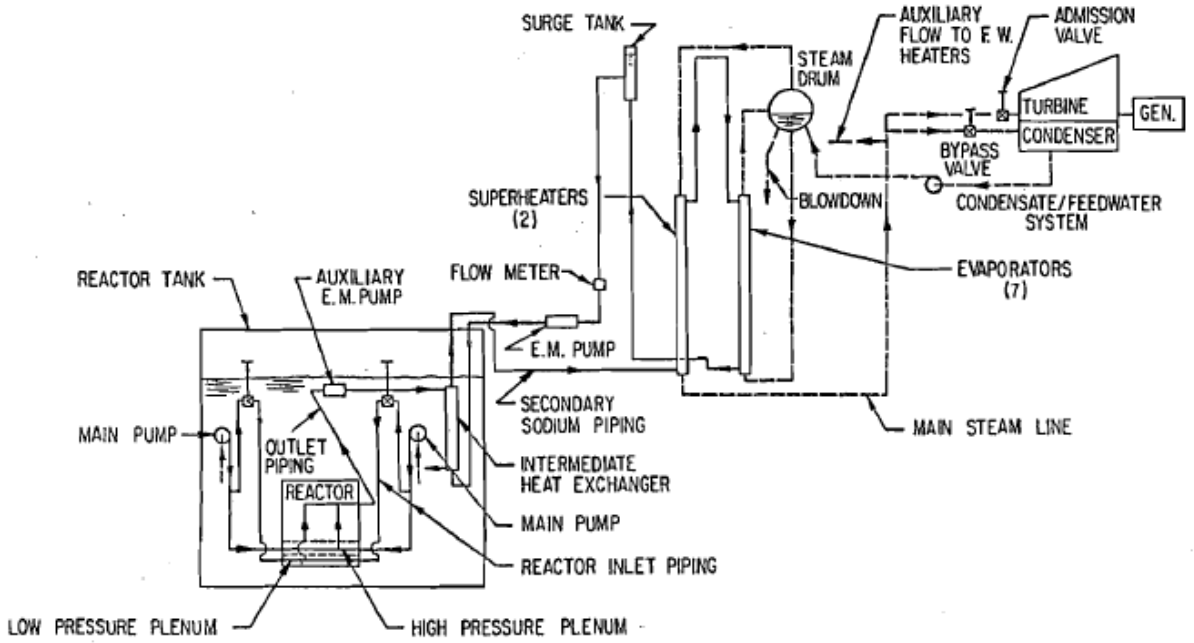


Figure 3. EBR-II plant schematic [13].

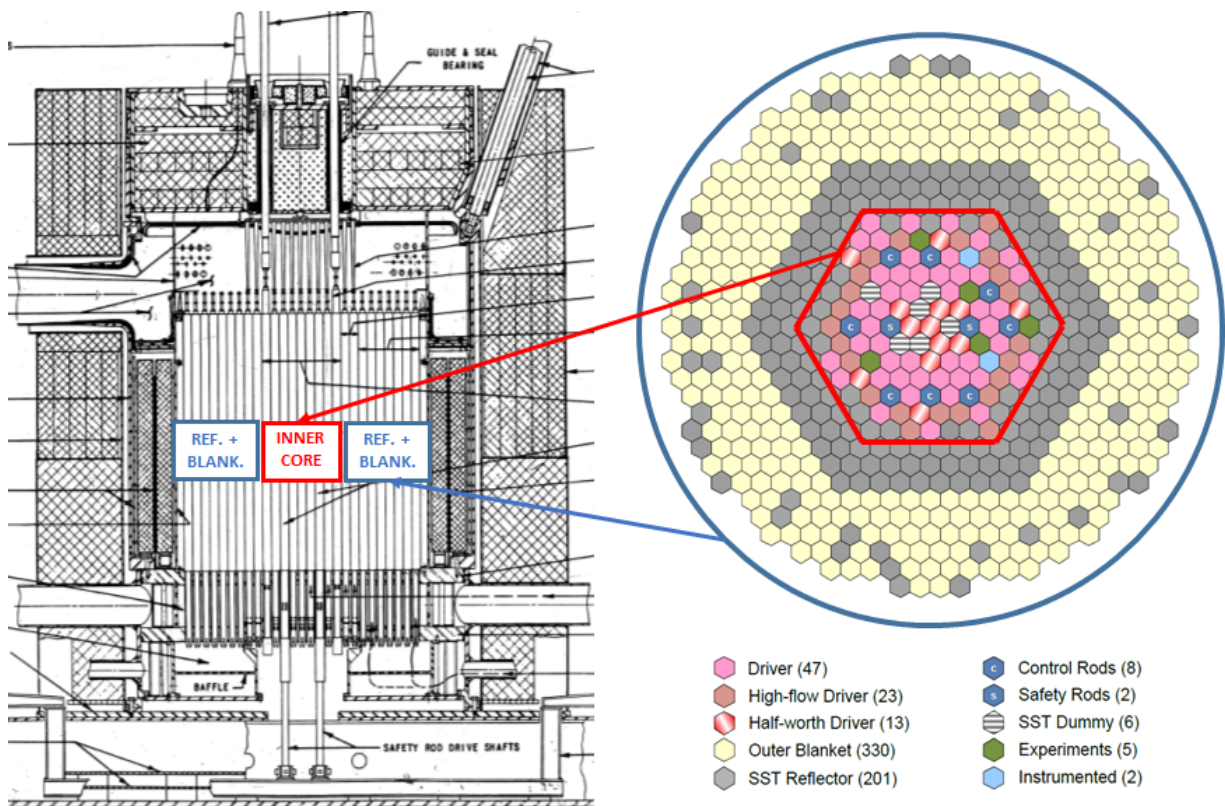


Figure 4. EBR-II reactor pool with HAs (left) and core pattern of the SHRT-45R transient (right) [15].

The core of the EBR-II is composed of 637 hexagonal assemblies (HAs), clearly divided in two zones: the inner core zone in which the fuel elements are present, and the outer core zone composed by reflector and breeding blanket elements. The flow to the inner core HAs, as stated above, is fed by a high-pressure inlet plenum, while the reflector and blanket flows are fed through the low-pressure inlet plenum.

The fuel elements are composed of a metallic alloy of uranium uniquely used for the EBR-II reactor called U-5Fs. U-5Fs is composed 95% (in weight) by metallic uranium and for the remaining 5% by fissium, which is a mixture of alloying elements composed by in 2.4% Mo, 1.9% Ru, 0.3% Rh, 0.2% Pd, 0.1% Zr and 0.01% Nb [16]. The uranium enrichment in the fuel is equal to the 67% weight content of ^{235}U .

All the constructive drawings and compositions of the different types of hexagonal assemblies present inside the reactor are reported in detail in the ANL benchmark specifications [13]. The pin lattice is triangular, as usual for hexagonal assemblies, with no spacer grids: the spacing function is carried out by a spacer wire which, in some instrumented assemblies, also acts as a thermocouple (Figure 5). Only part of the assembly height is active; above and below the fuel region, an axial reflector is present.

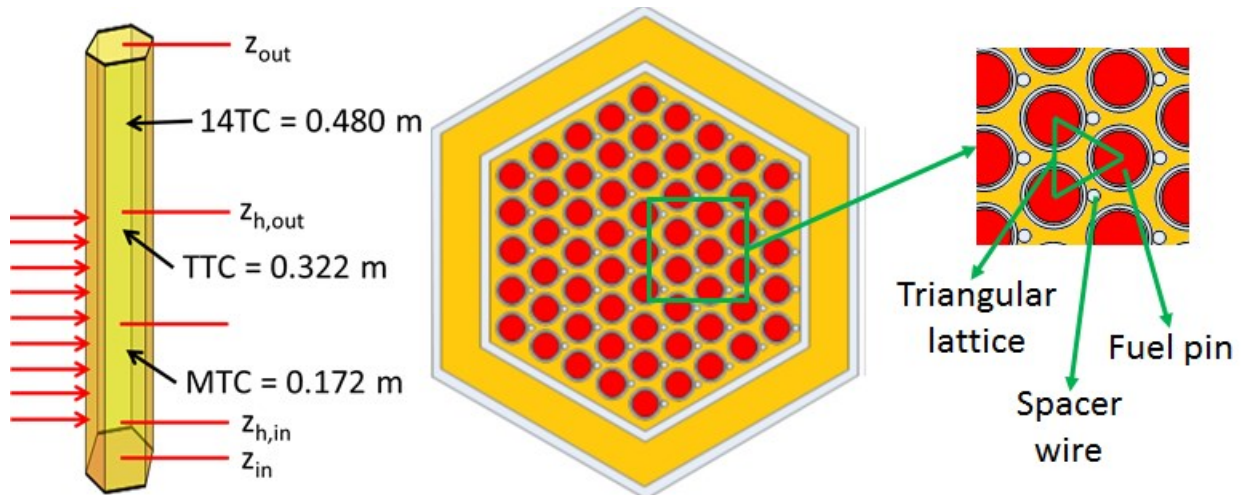


Figure 5. Axial view, horizontal section and lattice detail of HA of the BIB type [15].

Some of the assemblies have a smaller hexagonal box inside the main one (Figure 6). These assemblies are referred to as the “Box-in-the-box” (BIB) type. In the space between the two stainless steel boxes, referred to as “thimble”, a certain fraction of sodium is flowing.

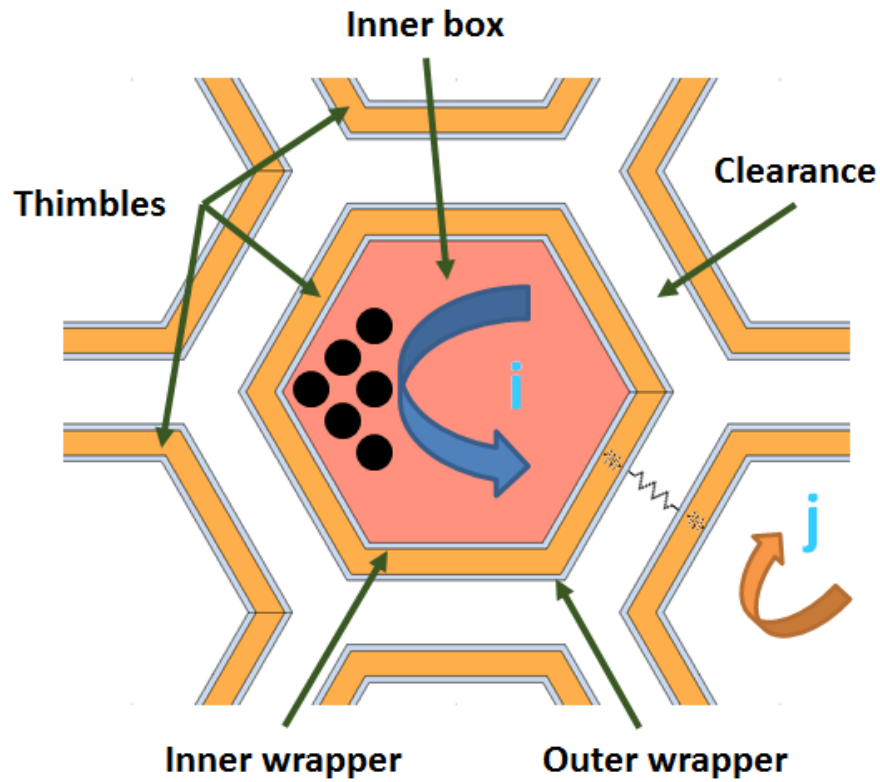


Figure 6. Schematics of BIB HAs and pre-existing inter-assembly heat transfer model

2.2 The Shutdown Heat Removal Tests

During the time EBR-II operated, a certain number of tests have been conducted in order to prove the inherent safety features of pool-type SFRs. The IAEA benchmark consists in the study of two of these transients in order to develop and improve experience on both neutronic and thermal-hydraulic modeling of transients of major safety concern, to provide both expertise and computational tools for the future GenIV reactors design and safety assessments.

Among these transients are the SHRT-17 and SHRT-45R, where SHRT stands for Shutdown Heat Removal Test. These tests were performed in 1984 and 1986 respectively, and both involved the trip of the pumps, therefore leading the reactor to work under natural circulation conditions, initially supported by the coast down of the immersed sodium pump.

The IAEA benchmark participants studied and modeled the whole reactor system, including pumps, heat exchangers and pipes from both primary and secondary (intermediate) loops (Figure 7).

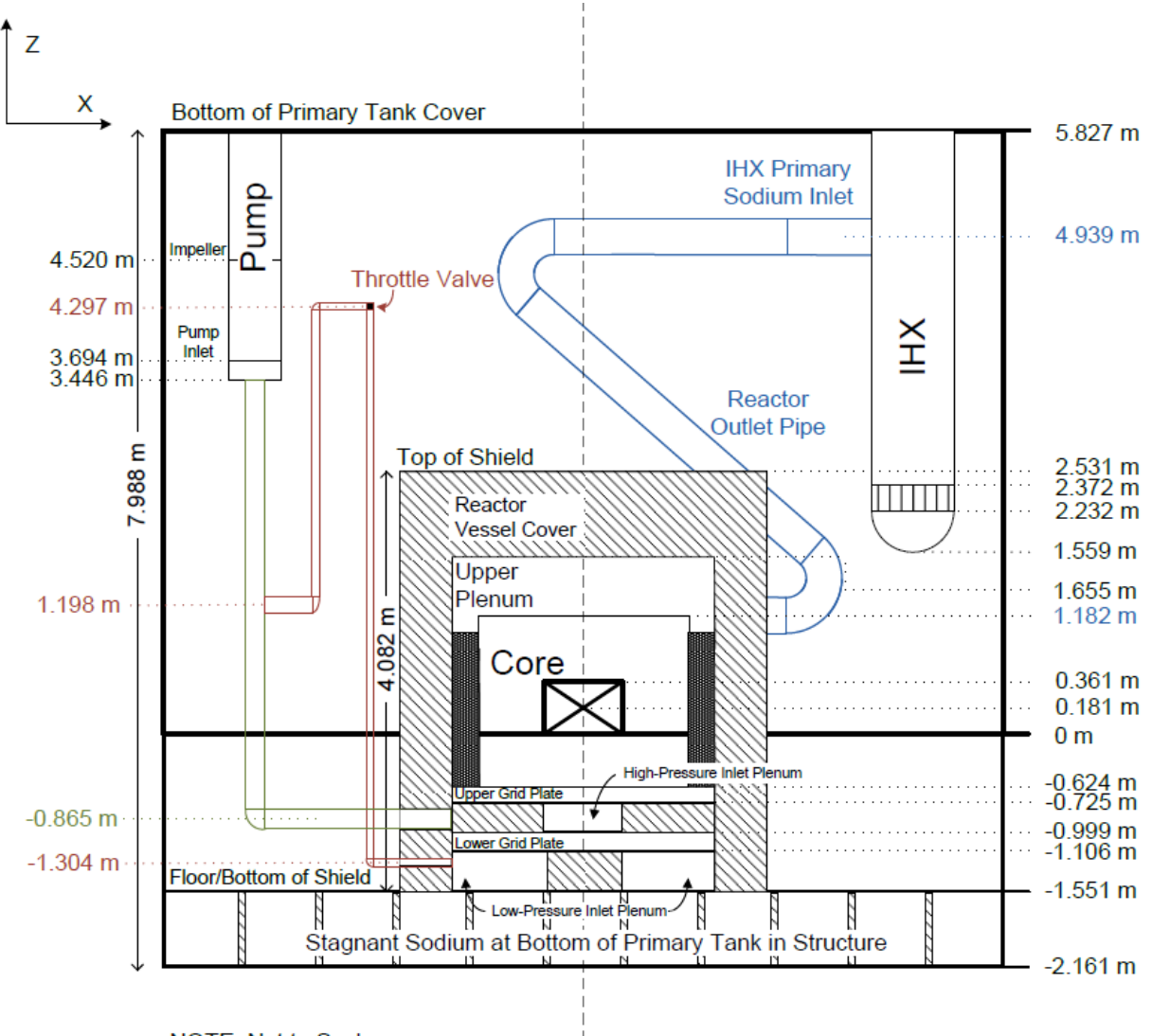


Figure 7. Benchmark model of primary vessel components, elevation view [13].

During the SHRT tests the reactor was equipped with two experimental HAs (XX09, a fuel assembly; XX10, a dummy assembly). Experimental data from these assemblies were provided for both SHRT after the first blind phase of the benchmark.

For the purposes of the benchmarking activity, the SHRT-17 transient is intended to be a purely thermal-hydraulic study, with the time-dependent power distribution provided as input by ANL. Instead, the SHRT-45R transient treats the time-dependent power distribution as an unknown quantity, requiring the participants to perform coupled neutronic/thermal-hydraulic analyses. Each of the transients is now described in further detail.

2.2.1 SHRT-17

The SHRT-17 was carried out on 20 June 1984. The reactor was operating at full power before the start of the transient and had reached an initial equilibrium state. The equilibrium operation lasted for two hours, in order to limit the decay heat after the SCRAM. The transient was initiated by a trip of the primary and intermediate pumps. The Plant Protection System was not bypassed, therefore the SCRAM occurred, and the source of heat inside the reactor was limited to the decay heat of the fission products. The two pumps were equipped with two different pump drive units that led them to follow different coastdown curves. The auxiliary electromagnetic

pump was not activated, while normally it would receive power from battery backups during a station blackout. After the start of the test no automatic or operator action took place until the test had concluded.

Data on decay heat power were available from ANL, and the assumption of uniform axial heating was made in making the calculations. ANL provided to participants also the model for pumps behavior in the Benchmark Specifications [13] and the constructor data concerning them, as well as the coastdown curves retrieved by means of this model. Data on pumps experimental flow rates were subsequently released by ANL in the post blind phase, but unfortunately only data for one of the two pumps were actually recorded; this lack of experimental data will impact on the analysis performed here. Coolant and fuel properties libraries were also provided by ANL [13, 17].

In Figure 8, the core-loading pattern for SHRT-17 is reported. A number denotes each hexagonal assembly, fully described in the Benchmark Specifications [13].

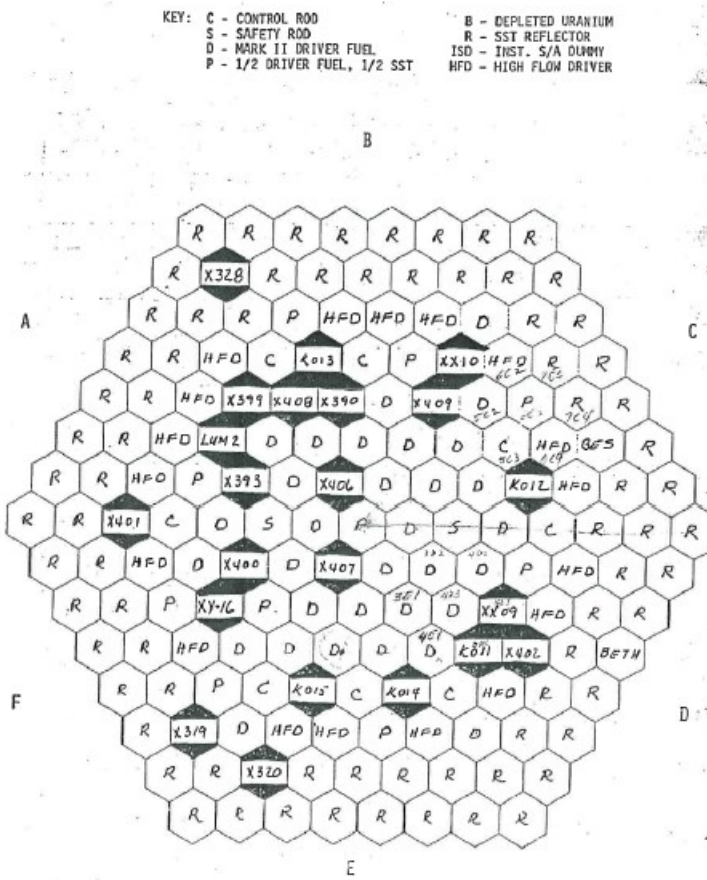


Figure 8. SHRT-17 core loading pattern for the first eight rings [13].

Figure 9 shows the power evolution in the first 60 seconds of the transient. The SHRT-17 transient started from an initial equilibrium configuration that was rated at a power of $57.3 \text{ MW}_{\text{th}}$ rather than the nominal $62.5 \text{ MW}_{\text{th}}$. The complete power distribution was provided by ANL in tabular form for the entire duration of the transient (900 s). The decay heat power was calculated based on the ANS decay heat standard for Light Water Reactors, because no experimental data are available for EBR-II (neither are they available for SFRs in general).

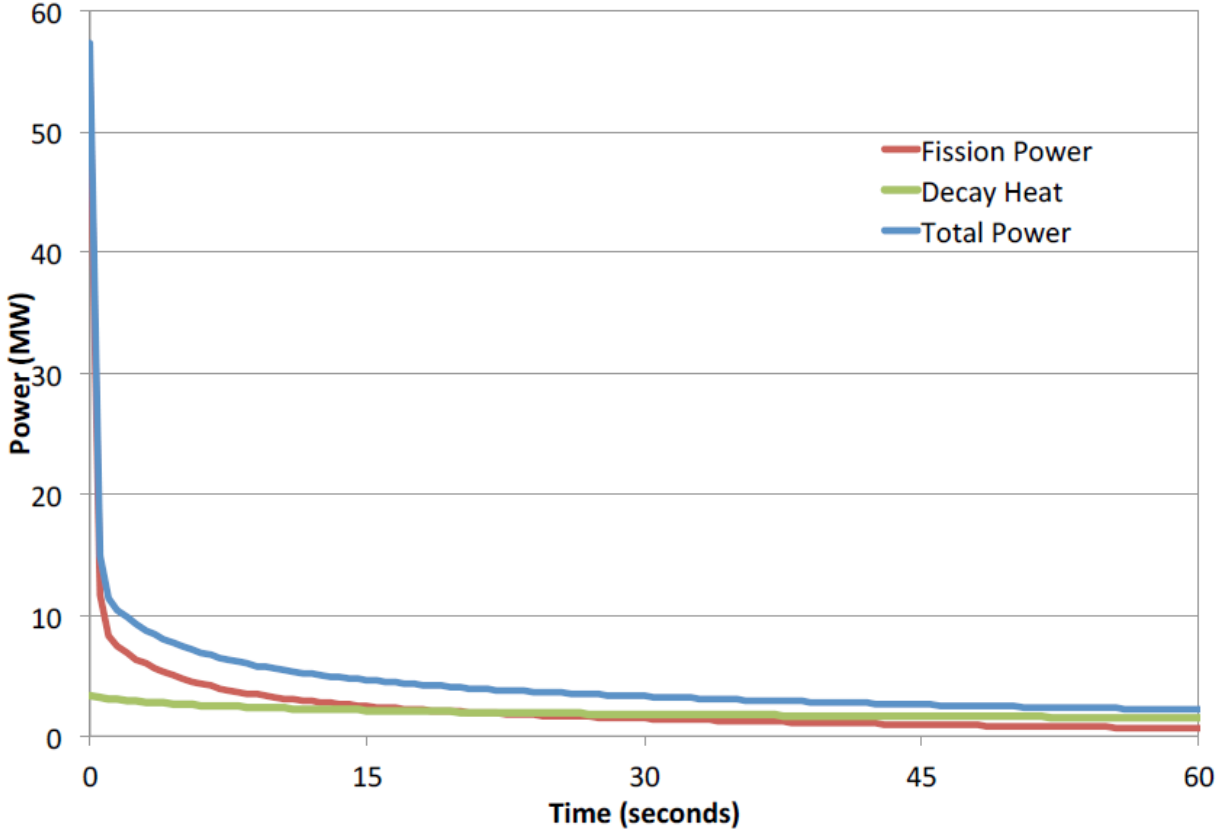


Figure 9. Power evolution as given by ANL [13].

The initial conditions of the transient were provided as well. Initial (steady state) flow rates have been calculated by ANL by means of the EBRFLOW code. This code was optimized on the EBR-II plant instrument data. Power at time $t = 0$ s in each HA, instead, was evaluated through the two dimensional discrete ordinates transport code DOT-III, developed by Oak Ridge National Laboratory: this code calculated both neutron and gamma flux distributions within each assembly. These data are reported on the Benchmark Specifications [13] as well.

In Figure 10 the experimental flow rates from primary pumps are reported. These data have been provided by ANL after the first blind phase of the benchmark. As stated before, the flow rate of one of the primary pumps (pump #1) was not registered. Participants to the benchmark used the experimental flow rates from pump #2 to better describe their pumps models and therefore to provide more accurate core inlet flow rates data to the core calculations.

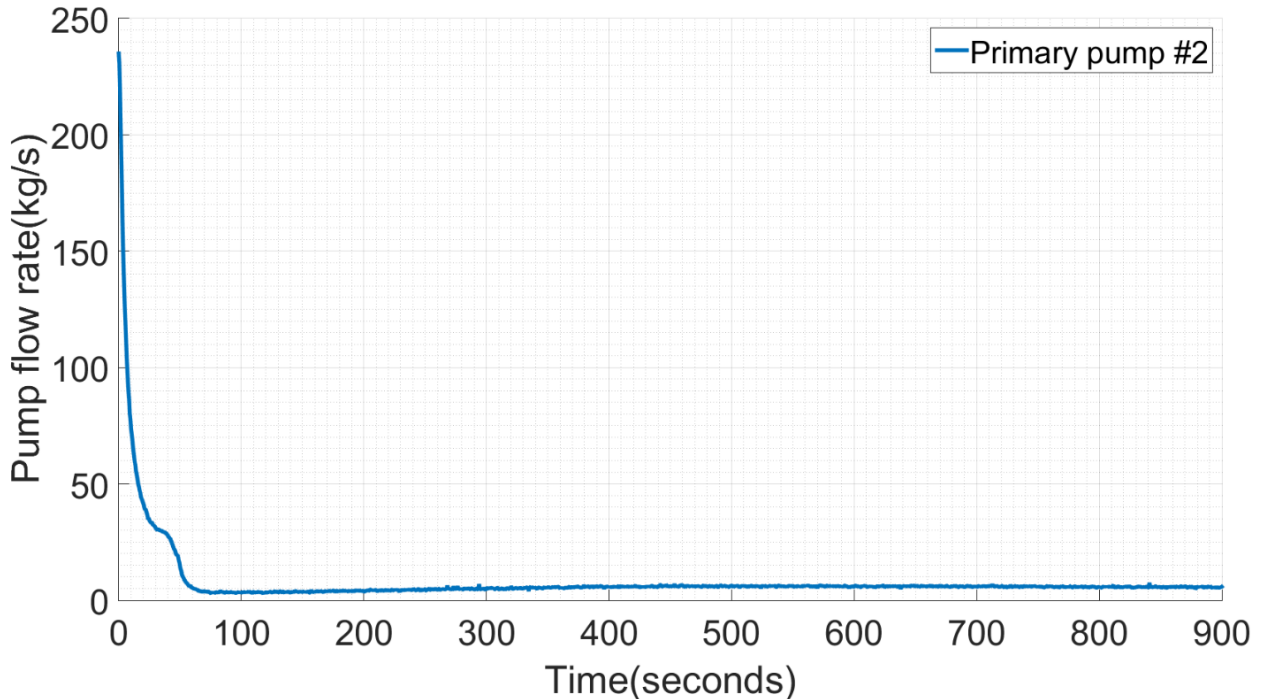


Figure 10. SHRT-17 experimental pump flow rates (post-blind phase) [18].

In addition, experimental results concerning the instrumented assemblies XX09 and XX10 were also provided after the blind phase concluded. These constitute the main reference to evaluate the performances of the participants' codes with the respect to the analysis of the core region, and therefore the only one of interest for FRENETIC calculations since the core is the only part of the system modeled, see below. The data provided consisted in the measurements coming from the assembly flowmeters and those from thermocouples at different element heights and locations in the hexagon cross section. Figure 11 shows an example of these results, for the temperature at the top of the core measured by the spacer wire thermocouple near the central pin.

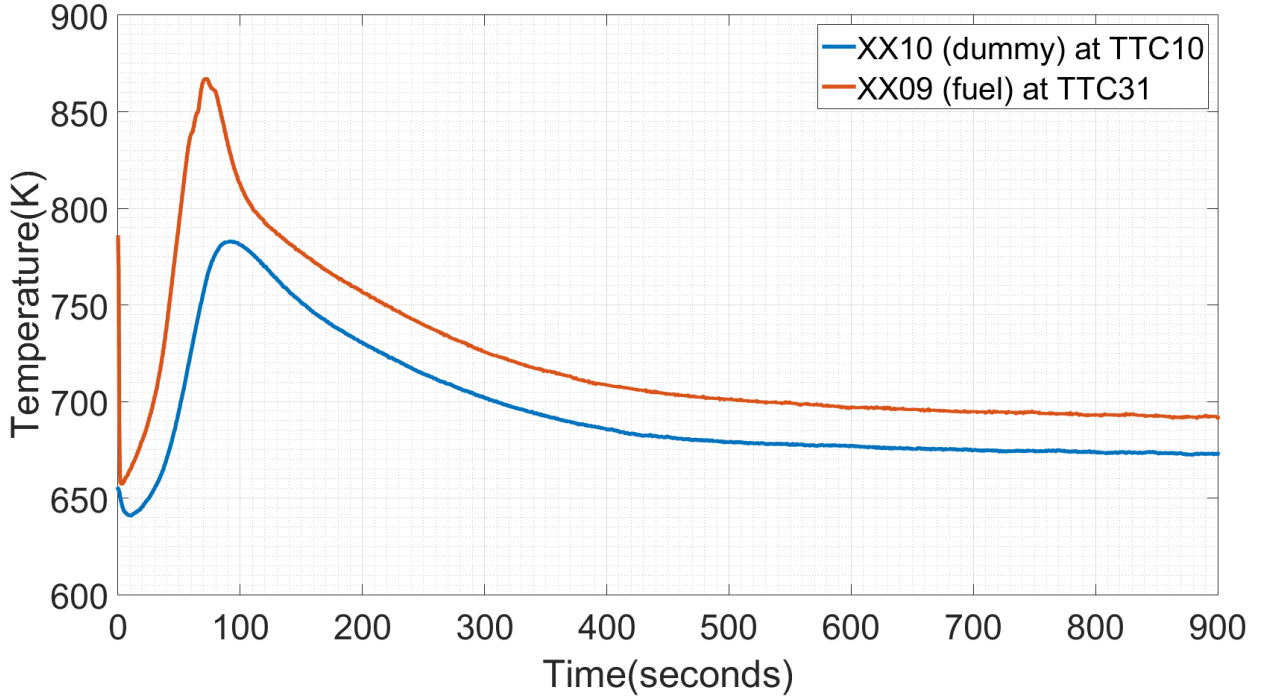


Figure 11. SHRT-17 example of experimental data on instrumented assemblies. TTC10 and TTC31 are thermocouple locations in the two assemblies [18].

Post-blind experimental results released by ANL also involved inlet and outlet plena average temperatures and data related to the rest of the primary components, such as the temperature drop across the Intermediate Heat Exchanger (IHX). They are not reported here since they are not used for comparison.

2.2.2 SHRT-45R

The SHRT-45R transient was carried out on April 3, 1986, to demonstrate the effectiveness of passive reactivity feedbacks in the EBR-II (and in all pool-type SFR). The Core Loading pattern, shown in Figure 12, is different from the one of SHRT-17. The Plant Protection System was disabled to avoid the SCRAM. As in SHRT-17, both the primary and intermediate coolant pumps were tripped, and the auxiliary pumps were inhibited in starting operation, therefore the only flow promoter in the reactor was the natural circulation and the pumps coastdown. As for SHRT-17, the two pumps were equipped with two different pump drive units that led them to follow different coastdown curves.

PROPOSED RUN 1308 (SHRT)

KEY: C - CONTROL ROD B - DEPLETED URANIUM
 S - SAFETY ROD R - SST REFLECTOR
 D - MARK II DRIVER FUEL ISD - INST. S/A DUMMY
 P - 1/2 DRIVER FUEL, 1/2 SST HFD - HIGH FLOW DRIVER

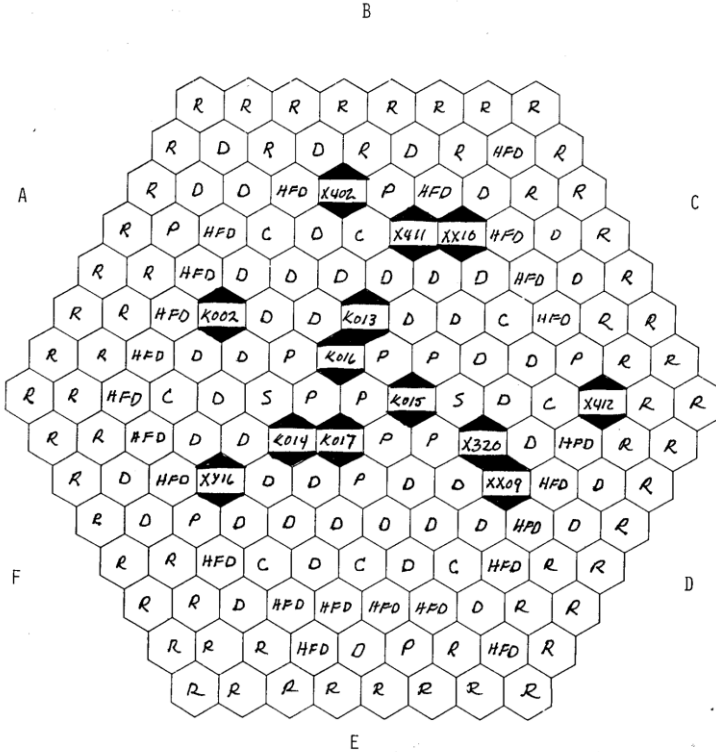


Figure 12. SHRT-45R core loading pattern for the first eight rings [13].

After the start of the transient, no human action was taken before its end.

Contrarily to SHRT-17, this time no source data on power were provided by ANL: the aim of the benchmark exercise with respect to SHRT-45R was, in fact, the setup of a coupled simulation in which neutronic calculations were made to retrieve the assemblies power. The reactor is, in fact, not scrammed in this case, so the chain reactions is still proceeding and power is still being generated during the loss-of-flow. Pumps coast down curves were given also for this transient.

Initial conditions for the simulations were again evaluated by means of the EBRFLOW code for what concerns steady state flow rates and the DOT-III to produce steady state power. A history of irradiation occurred before the start of the transient was also provided to compute the fission power time evolution.

Experimental data provided by ANL also for the SHRT-45R transient after the first blind phase, include the pumps and instrumented subassemblies measurements and the lower and upper plena average temperature data as well as the temperature drop across the IHX as in SHRT-17, but also the time evolution of the reactor power, that this time had to be computed by participants to the benchmark. Figure 13 to Figure 15 show the subset of experimental data relevant in the framework of the FRENETIC validation exercise.

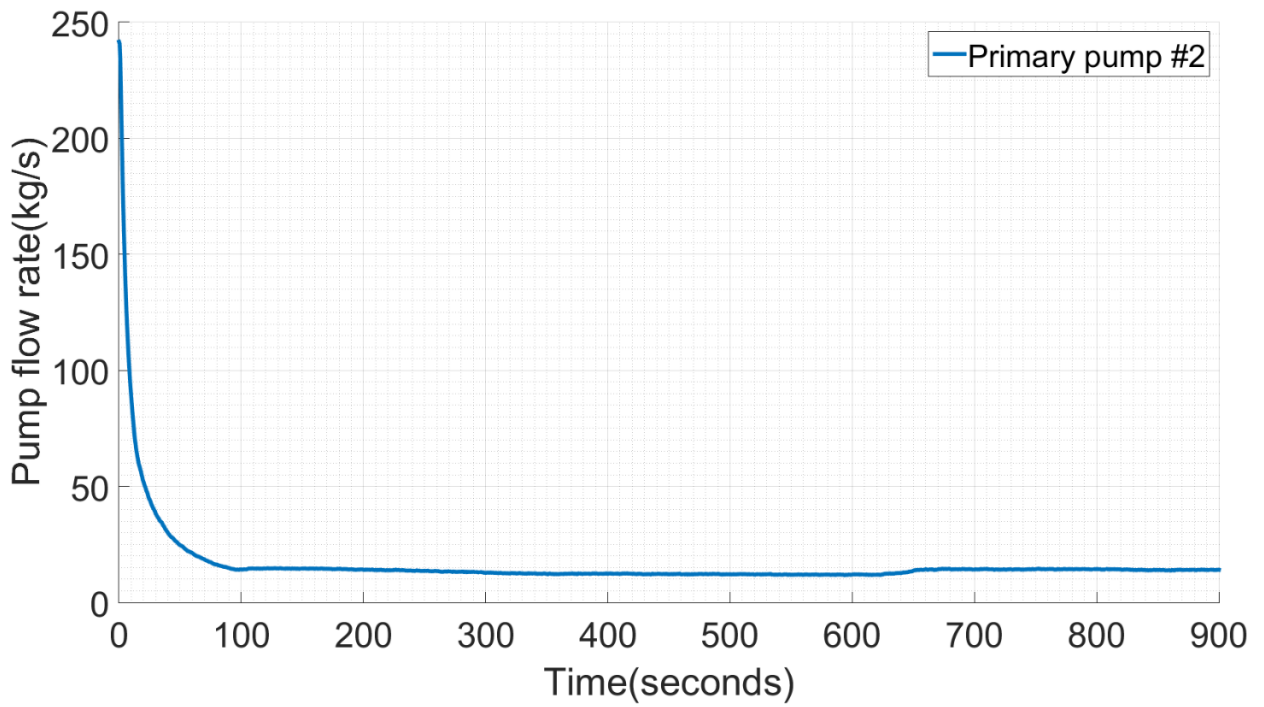


Figure 13. SHRT-45R experimental pump flow rates (post-blind phase) [18].

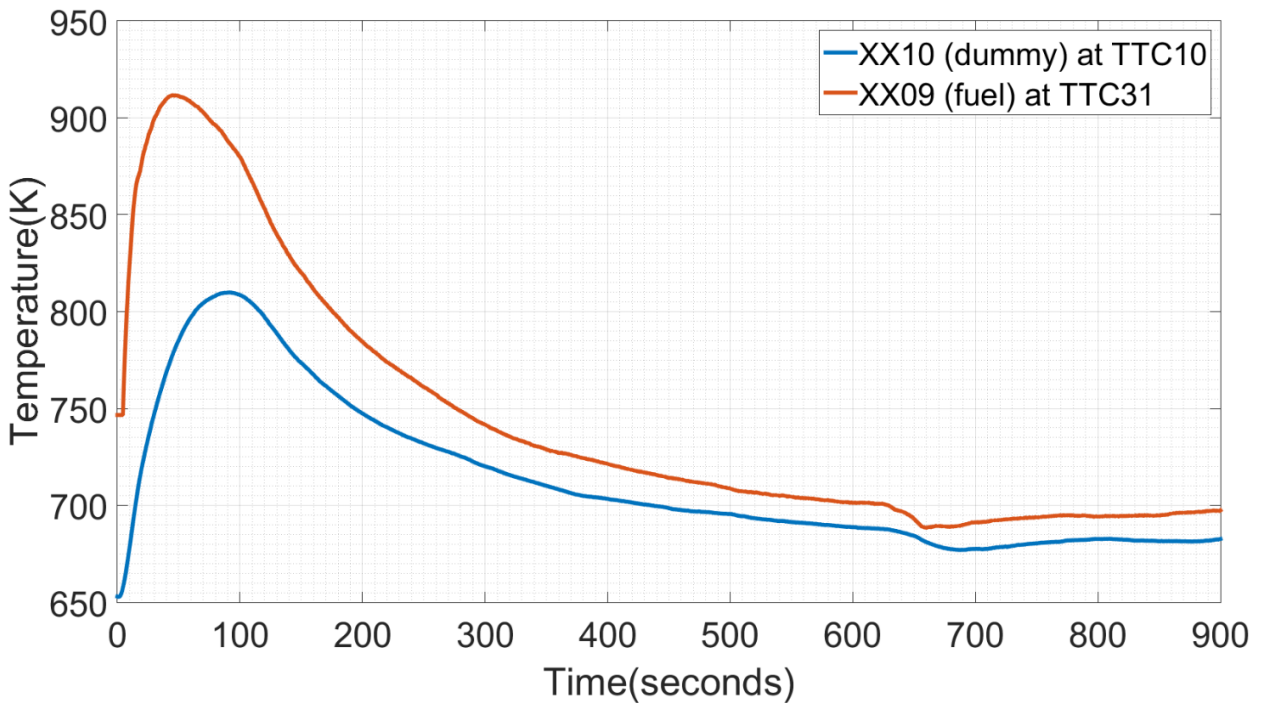


Figure 14. SHRT-45R example of experimental data on instrumented assemblies. TTC10 and TTC31 are thermocouple locations in the two assemblies [18].

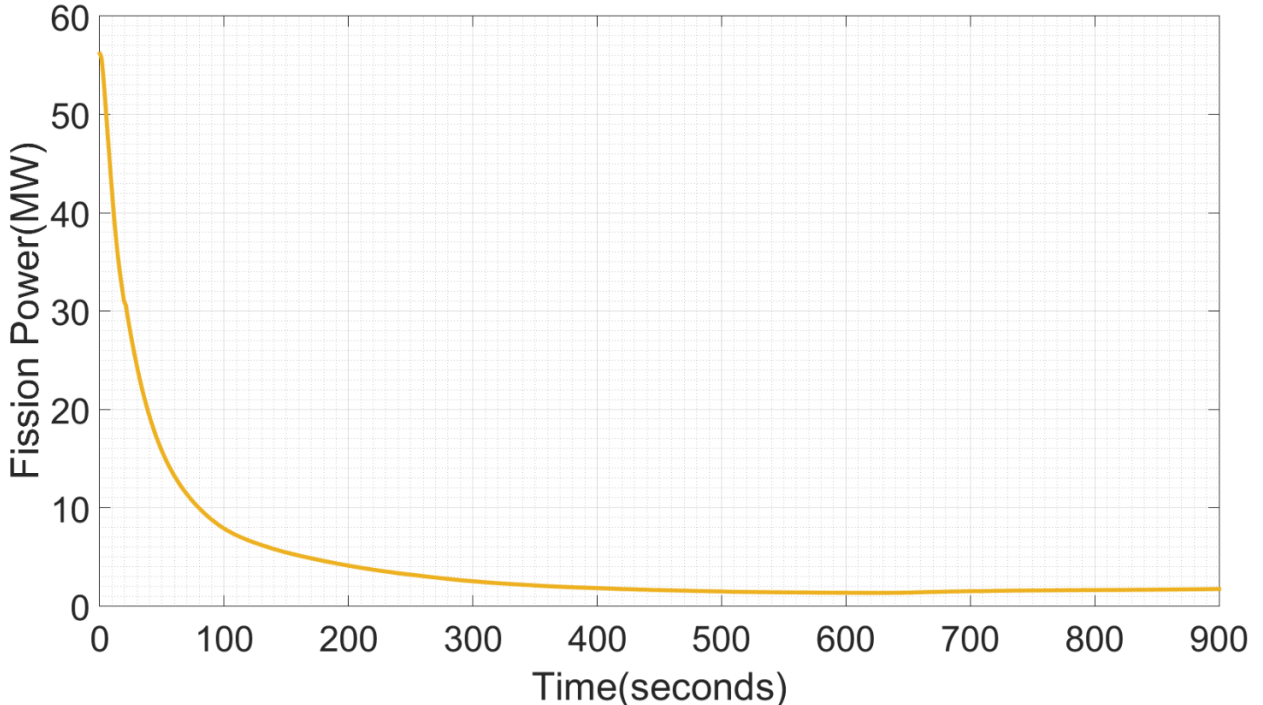


Figure 15. SHRT-45R time evolution of the EBR-II reactor power [18].

The same considerations made on SHRT-17 about instrumented assemblies experimental data and data concerning the rest of the primary system are still valid for this transient.

3 Development and validation of the thermal-hydraulic module

In order to validate the TH module of FRENETIC for the inter-HA simplified heat exchange model [5], the FRENETIC calculations were benchmarked against the results obtained with the RELAP5-3D© code [12, 19] in the framework of the IAEA benchmark [13]. Thanks to the availability of post-blind phase experimental results within the benchmark exercise activity, also RELAP5-3D© simulations were re-run and new and updated boundary conditions have been used as FRENETIC input with respect to the work presented last year.

In order to perform an analysis representing as close as possible the experimental setting and geometry of the reactor, two new features were added to the FRENETIC code:

- “Box-in-the-box” model: modeling of flow rates in HA so-called “thimbles” (this fraction of coolant was considered stagnant before). This modification directly accounts for the particular geometry of the HAs of the EBR-II sodium cooled reactor.
- 1D radial conduction model: substituting the pre-existing simplified 1D axial conduction model. This is a principle modification implemented due to the significantly higher temperature gradients in the radial direction rather than in the axial one, and to align FRENETIC to the existing state-of-the-art codes for fission reactors simulations.

These new models have been applied in particular to the SHRT-17 transient of the EBR-II, considered as a purely thermal-hydraulic transient because it is a protected loss of flow and thus after the scram the neutron flux is negligible.

The work is organized as follows: first the above described new models are presented, showing the difference between them and the existing ones; then the improvements of the SHRT-17 simulation due to the new implementation is reported, using different sets of boundary conditions to assess the sensitivity of the code to data.

A brief description of the computational domain of the SHRT-17, as already shown in [12], is hereby given:

- Axially, only a region of 0.6108 m is considered, starting from the bottom of the active core and ending just above it, below the upper plenum (Figure 16). The heated length of the core is 0.3429 m.
- Radially, only the seven innermost hexagonal rings of the core are considered, since the blanket and reflector regions have little thermal-hydraulic interest in this transient. The core loading pattern of these rings is reported in Figure 17. The subassembly types are described in the Benchmark Specifications [13].

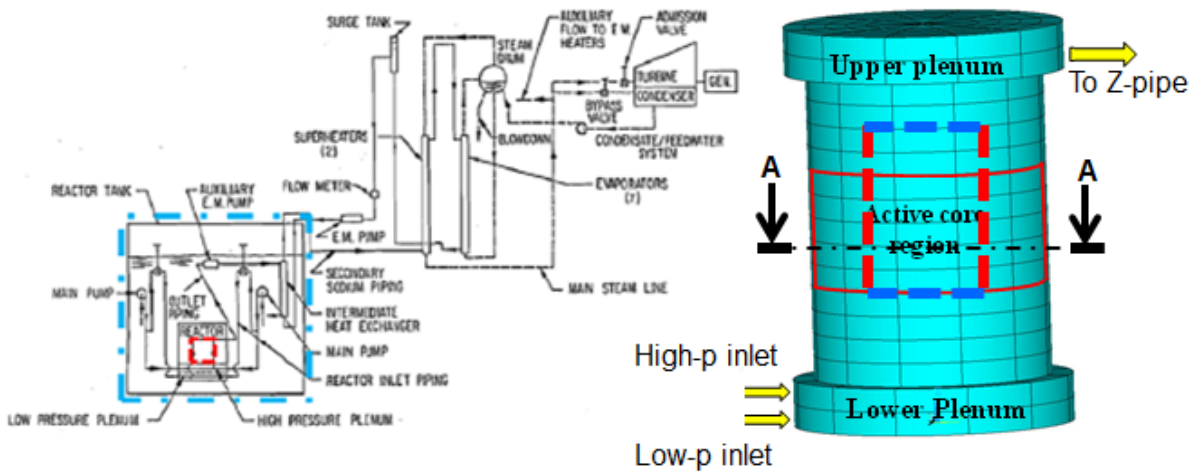


Figure 16. Computational domain of FRENETIC simulation (red-dashed line, left) vs. computational domain of RELAP5-3D© simulation by ENEA (blue-dashed line, left) and representation of axial computational domain of FRENETIC (right).

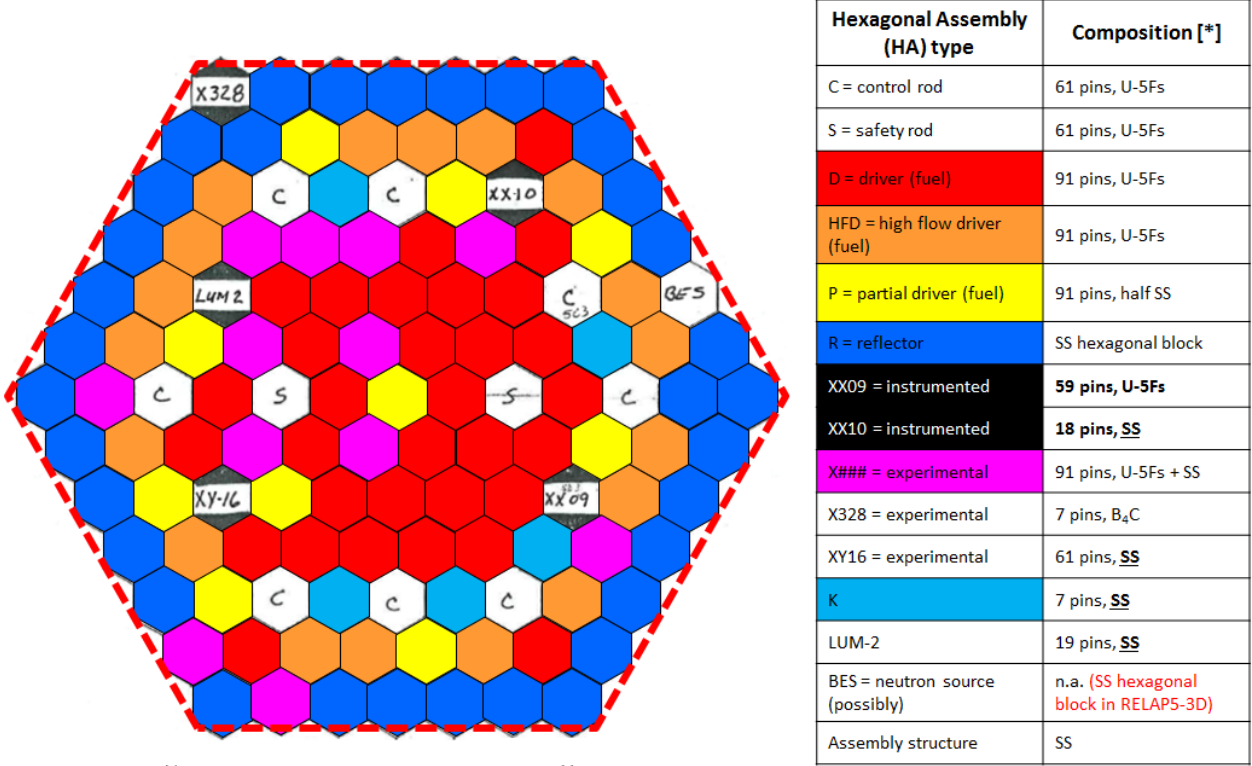


Figure 17. Core loading pattern of SHRT-17 transient: portion of the core considered in the FRENETIC calculations.

3.1 Implementations in the thermal-hydraulic module

As mentioned above, two different models have been added to the TH module of the FRENETIC code, coming from different considerations.

“Box-in-the-box” (BIB) model: this new feature has been added specifically to validate the model in the framework of the IAEA Benchmark. Indeed, some of the EBR-II HA are made by two nested stainless steel boxes. The sodium contained between the inner and outer stainless steel hexagonal boxes was originally considered a stagnant thermal resistance in order to evaluate heat transfer in the horizontal plane. This approximation, however, is not representative of the real physics, since the flow rates in the thimbles may be comparable to those of the inner channels in BIB-HAs and thus they cannot be considered small. This condition is clearly visualized in Figure 18, where both the thimble and inner channel flow rates are plotted for the instrumented assemblies XX10 and XX09 during the SHRT-17 transient. It must be noted that, while the inner channels flow rates refer to experimental data provided by ANL after the blind phase of the benchmark exercise, the thimble flow rates are those computed with RELAP5-3D© by the ENEA group. This is because the flowmeters in the instrumented assemblies XX09 and XX10 only measure the innermost box flow, so only that fraction of the flow rate that experiences direct contact with fuel pins. The fact that in some cases (e.g. XX10 HA) the thimble flow is non negligible or even of the same order of magnitude of the inner box flow led to the consideration that a model for the thimbles in “Box-in-the-box” assemblies was fundamental to properly describe the heat transfer phenomena in the EBR-II reactor.

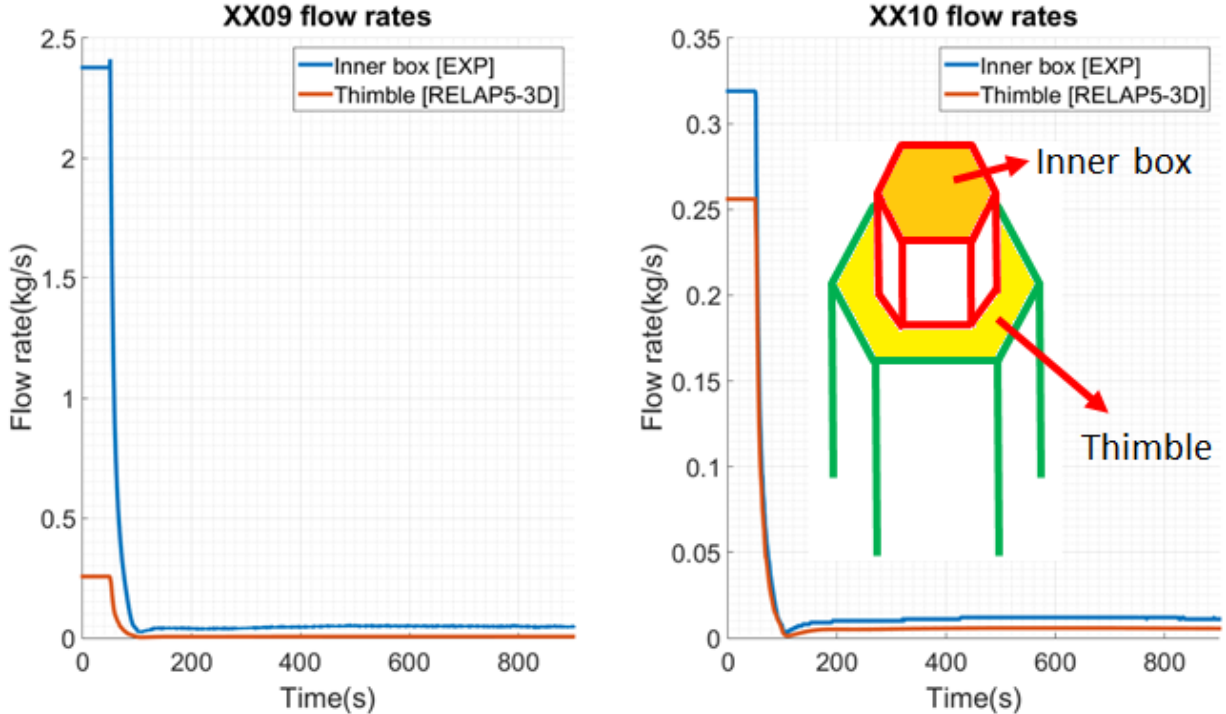


Figure 18. Comparison between inner box and thimble flow rates in XX09 and XX10 instrumented assemblies during SHRT-17 transient. Inner box flow rates are the experimental flow rates provided by ANL in the post-blind phase of the CRP; no experimental data is available for thimble flow rates that come from RELAP5-3D©.

1D radial conduction model: Due to the fact that the FRENETIC TH model originates from the Mithrandir code [20] for fusion application superconductors, the heat conduction in the pins was initially modeled with a 1D axial approach: this feature is neglected in most of the nuclear fission reactor codes (such as CATHARE© and RELAP5-3D©) since it accounts for a small effect with respect to the radial heat transfer phenomenon. To justify such a 1D simplified model, literature on heat transfer exploits the dimensional analysis of the involved quantities. In [21] it is possible to find when a lumped parameter capacitance model can be justified: the Biot number (Bi), which takes the physical meaning of the ratio of convection over conduction, must be less than 0.1: $Bi = \frac{hL_c}{k} < 0.1$, where h is the convective heat transfer coefficient of the coolant (sodium), k the thermal conductivity of the solid (pin) and L_c is the characteristic length of temperature variation in the solid (the radius of the pin). This condition would imply that temperatures inside the solid are very homogeneous because of the high weight of conduction with respect to convection, and therefore spatial effects inside the solid may be neglected. Figure 19 shows the Biot number for both a fuel and dummy reference assembly coming from a preliminary analysis of the SHRT-17 transient. RELAP5-3D© data were used as Boundary Conditions (BC) and the ANL library of thermophysical properties of sodium was used to determine coolant properties as indicated in the ANL Benchmark Specifications [13].

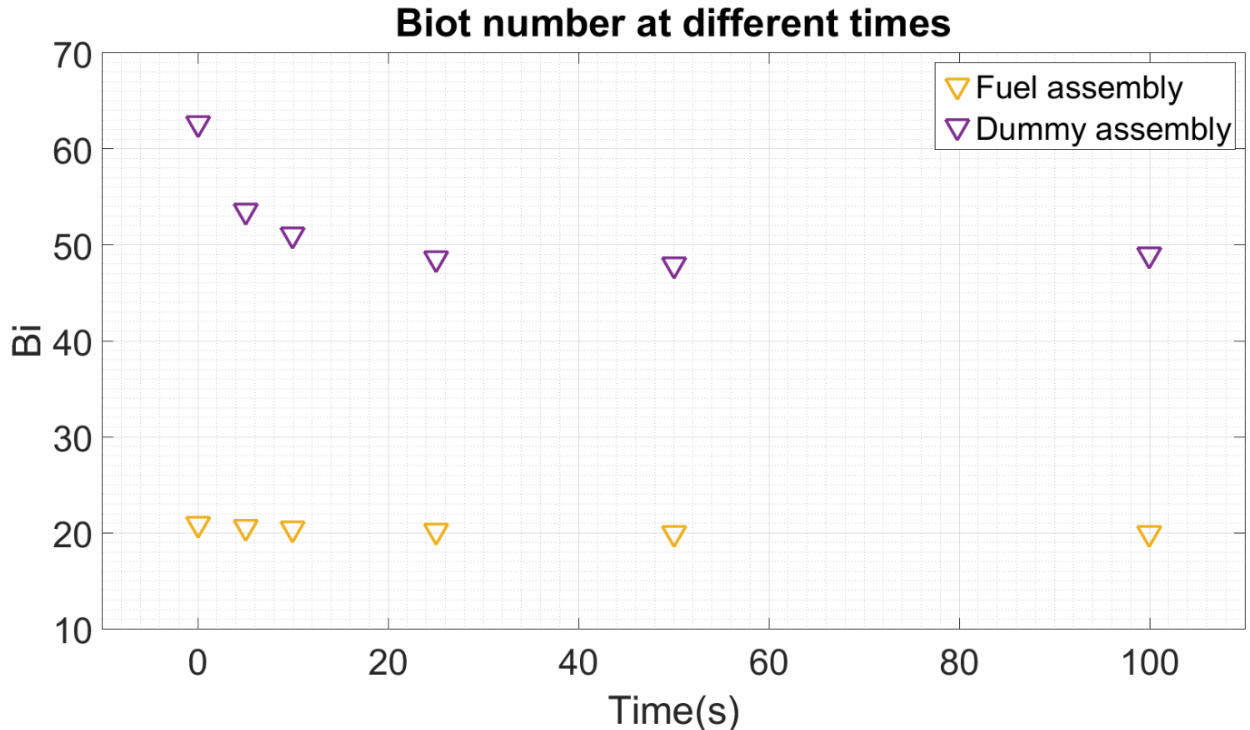


Figure 19. Biot number analysis in the SHRT-17 transient for representative hexagonal assemblies (dummy and fuel).

Since $\text{Bi} \gg 0.1$ during the first 100 s of the transient, going approximately from the steady state condition to the temperature peak situation, it is clear that a model that averages the temperature over the pin horizontal section is not suitable to describe them. What has been done so far to cope with this situation was to assume a parabolic behavior of the temperature distribution along the radial coordinate, virtually inserting in the model the geometrical effect. In such a way, the surface temperature of the pin to be considered for the convection heat transfer with the coolant was directly derived by the pin average temperature and the power generated in the pin [5]. This assumption, true at steady state, can be a too rough assumption during transients when redistribution of heat stored in the pin occurs.

In addition, the Biot number is somewhat a “static”, steady state, dimensionless number, and since SHRT are not steady situations but transients, a means by which to take into account the evolution of quantities in time is also to be considered. The Fourier number, another dimensionless parameter, is an indication of the speed of the heat diffusion process due to conduction. Transients characterized by characteristic times smaller than the conduction one cannot be suitably described by the existing simplified model and will surely need better modeling. To have a good description of transients by means of a lumped capacitance model, the following should therefore be verified:

$$Fo = \frac{\alpha}{L_c^2} \cdot \tau_{transient} > 10 \rightarrow \tau_{transient} > 10 \frac{L_c^2}{\alpha} = \begin{cases} 62.1 \text{ s} & (\text{Fuel HA}) \\ 4.2 \text{ s} & (\text{Dummy HA}) \end{cases} \quad (1)$$

where k , ρ and c_p are respectively the thermal conductivity, the density and the specific heat of the solid (pin), while $\alpha = \frac{k}{\rho c_p}$ is its thermal diffusivity. This clearly defines the need of the FRENETIC code for a better radial model to properly describe faster transients.

3.1.1 Box-in-the-box model

The pre-existing model (schematized in Figure 20) considered the coolant in the thimble to be stagnant, and treated it as a steady-state “slab-type” conductive thermal resistance, as well as the coolant in the clearance between the outer boxes of neighboring HAs and the steel boxes themselves (both outer and inner in the case of BIB HAs).

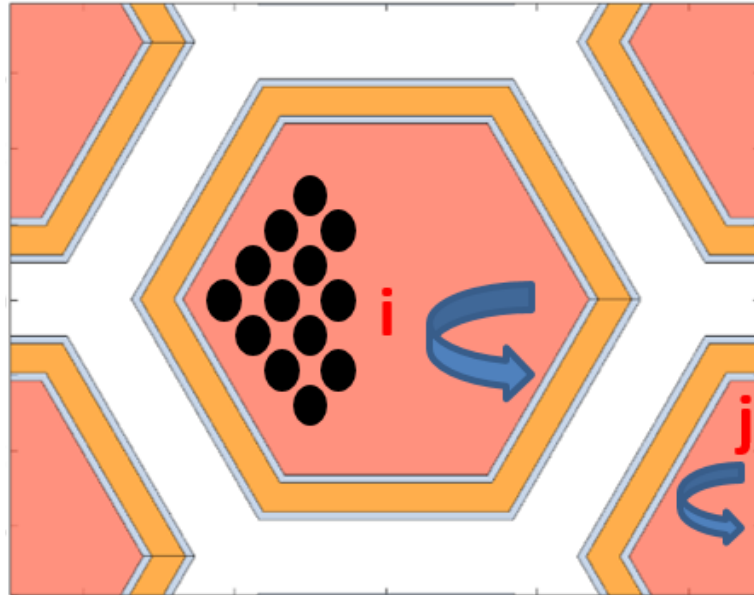


Figure 20. Old (pre-BIB) heat transfer model between neighboring assemblies.

No effect of the flowing of sodium inside the thimble was considered in the old model for the heat transfer, and it has been shown that this may play a major role during the study of some transients.

The convective heat transfer coefficient for sodium has been evaluated in these simulations by the Seban-Shimazaki formula, developed for hexagonal boxes, for turbulent fully developed flows at constant wall temperatures

$$Nu_i = 5 + 0.025 \cdot Pe_i^{0.8} \quad (2)$$

where Nu is the Nusselt number and Pe the Peclet number.

The fluid in each HA exchanges with the six surroundings through the sides of the SS wrappers, the stagnant clearance and the thimbles as if each of these layers were an infinite slab of thickness equal to the real thickness of the layer considered. The global heat removed or received by the coolant in the i -th assembly is simply the algebraic sum of the contributions coming from the six edges.

With respect to the above presented existing model, mass flow rate of the coolant in the thimble of BIB HAs is accounted in the new BIB model as a 1D flow in the same way as it is done for the non-BIB HAs and for the inner boxes of BIB assemblies. This is done in order to have a more detailed evaluation of the actual inter-HAs heat exchange, because the flow rate in the thimble was proved to be non-negligible with respect to the one in the inner channel. The model is as follows:

- The inner channel of the BIB HAs only exchanges heat with the surrounding thimble (Figure 21), through each of the six edges of the inner SS wrapper. The SS layer is modeled as an infinite slab separating the inner channel from its thimble. The overall

thermal resistance between the coolant in the i -th inner hexagon and that in its thimble is then

$$R_{in \rightarrow thimb,i} = \frac{1}{h_{conv,i}} + \left(\frac{s}{k}\right)_{inbox} + \frac{1}{h_{conv,i,thimb}}, \quad \left[\frac{m^2 K}{W}\right] \quad (3)$$

with s being the thickness of the considered layer, k its thermal conductivity and h the convective heat transfer coefficient (HTC) for the coolant flow inside the inner stainless steel hexagonal box.

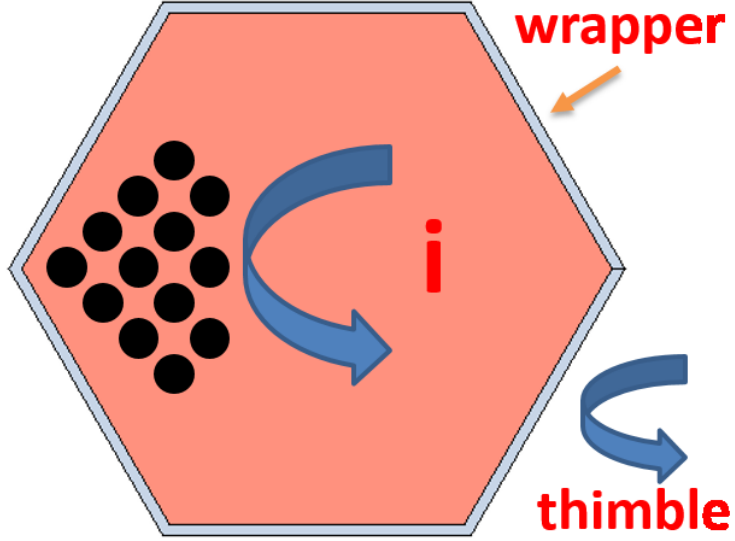


Figure 21. New BIB model schematization of inner hexagons.

The $h_{conv,i}$ and $h_{conv,i,thimb}$ HTCs are again both evaluated through the Seban-Shimazaki formula (2). The heat exchange between the inner and the thimble coolant will be

$$q_{in \rightarrow thimb,i} = \frac{p_{wrap} \cdot (T_i - T_{thimb,i})}{R_{in \rightarrow thimb,i}}, \quad \left[\frac{W}{m}\right] \quad (4)$$

being p_{wrap} the inner perimeter of the inner wrapper.

- The thimble is now treated as a 1D channel where the coolant is flowing. It will exchange heat through the outer SS hexagon with the surrounding assemblies and simultaneously, through the inner SS wrapper, with the coolant in the inner box. The k -th channel shown in Figure 22 can be either the thimble of the k -th assembly (if it is of the BIB type) or the coolant in the inner box of the “standard” (i.e. not BIB) HA. In general, the thermal resistance between the thimble and the k -th channel is evaluated as follows:

$$R_{tot,k} = \frac{1}{h_{conv,i,thimb}} + \left(\frac{s}{k}\right)_{outbox,i} + \left(\frac{s}{k}\right)_{Na\ clearance} + \left(\frac{s}{k}\right)_{outbox,k} + \frac{1}{h_{conv,k,thimb}} \cdot \delta_{BIB} + \frac{1}{h_{conv,k}} \cdot (1 - \delta_{BIB}), \quad \left[\frac{m^2 K}{W}\right]; \quad (5)$$

with $\delta_{BIB} = \begin{cases} 1 & \text{if } k \text{ is BIB} \\ 0 & \text{elsewhere} \end{cases}$

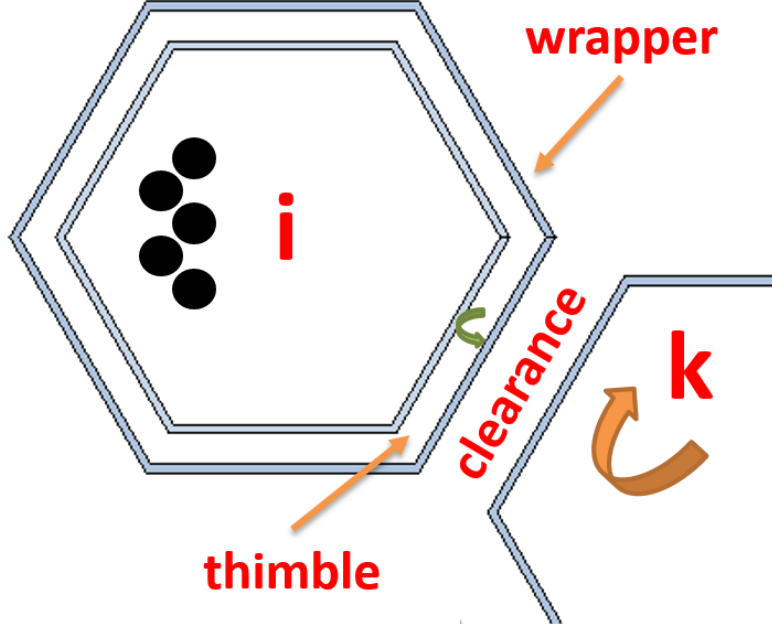


Figure 22. New BIB model schematization of inter-HA exchange on horizontal plane.

The convective heat transfer coefficient for the flowing coolant is evaluated through the Seban-Shimazaki formula also in the new model. For what concerns the total linear power exchanged by the thimble through both its SS wrappers (inner and outer), this will be composed by two terms:

- The opposite of the power evaluated for the inner channel of the i -th assembly
- The term taking into account the exchange of the thimble with the surrounding channels (whether not-BIB HAs or thimbles of BIB HAs)

The linear power will be therefore evaluated through the following formulation:

$$q_{thimb} = q_{thimb \rightarrow surrounding,i} - q_{in \rightarrow thimb,i} = \\ = \sum_{k=1}^6 \frac{l_{edge} \cdot (T_{thimb,i} - T_k)}{R_{tot,k}} - q_{in \rightarrow thimb,i}, \quad \left[\frac{W}{m} \right] \quad (6)$$

l_{edge} is the outer edge of the outer stainless steel wrapper.

3.1.2 Pin radial model

The FRENETIC code, so far, considered the fuel pins inside the hexagonal assemblies to be collapsed in a single point per each axial node, preserving mass and so thermal inertia of the cross section of the pin, in a so called “lumped capacitance” approach. In addition, the assumption was made that the temperature distribution along the radial coordinate of the fuel pin is of parabolic shape:

$$T(r) = T_{fuel,s} + \frac{q_v^2}{4k} (r^2 - r_p^2) \quad (7)$$

This assumption, which comes from the analytical steady state temperature distribution in case of volumetric heat generation, and therefore it is exact when there are only small variations of the source or conditions at the boundary ($T_{coolant}$ and/or h), may be wrong in a transient application, therefore a new model had to be developed to properly analyze the evolution of physical quantities with time.

For the sake of simplicity and to still allow fast and reliable transient evaluations of LMFBR, which is the main goal of the FRENETIC code, the new model had to drop the axial conduction in favor of the radial conduction model. Anyhow, this is not a major concern since its contribution with respect to the other heat transfer mechanisms is negligible. For the same reason, well-known nuclear codes such as RELAP5-3D© and CATHARE© do not include this feature as well. In fact, the heat transfer time characteristic of heat diffusion through conduction in the pin in the axial direction for a length ΔH is significantly larger than the sum of the advection and convection characteristic times:

$$\frac{\Delta H^2}{\alpha_{pin}} \gg \frac{\Delta H}{v_{Na}} + 2 \frac{D_{pin}}{4h} \rho_{pin} c_{p,pin} \quad (8)$$

Calculations bring to an order of magnitude of 10^1 s for axial conduction (left-hand side of the inequality) against 10^{-1} s for convection (right-hand side).

Since the coolant inside a single HA is considered by FRENETIC to be at a uniform temperature, velocity and pressure at each axial element z , and since to each pin of the same HA the same linear power is assigned, the model cannot distinguish among the different pins inside each HA, and therefore just one radial problem is solved per HA at a certain height z . The heat transfer surface per unit length through which the fuel is coupled to the pin is equal to $S = 2\pi r_p$, where r_p is the pin diameter.

The physical problem to be solved is the 1D radial transient heat conduction equation in the following form:

$$\rho_{fuel} c_{fuel} \frac{\partial T}{\partial t} - \frac{1}{r} \frac{\partial}{\partial r} \left(r k_{fuel} \frac{\partial T}{\partial r} \right) = q_v \quad (9)$$

where q_v is the volumetric heat generation inside the pin, and can easily be expressed as follows:

$$q_v = \frac{q_{lin}}{N_{pins} A_{pin}} = \frac{q_{lin}}{N_{pins} \pi r_p^2} \quad \left[\frac{W}{m^3} \right] \quad (10)$$

The new model approximates space derivatives with a 1D linear finite element approach, which corresponds to the central difference methods. The forward marching in time is approximated by an implicit Crank-Nicholson algorithm. The model comes from a similar one, previously implemented in a thermal hydraulic code [22] for fusion application where it served as heater wrapped around the superconducting magnets. In that case, the heater was a hollow cylinder while the FRENETIC code needed a full cylinder model to simulate the pin. The possibility to simulate hollow cylinders, anyhow, has been left in the code to allow the possible application to new-conception hollow fuel pins, to which the nuclear industry is expressing interest.

As visually reported in Figure 23, the pin is subdivided in a certain number of elements, which are concentric cylindrical shells starting from the center of the pin to its outer surface. Each element is delimited by two nodes, in such a way that $N_{nodes} = N_{elements} + 1$. The first node of the first element corresponds to the center of the pin, while the second node of the last element represents the pin surface, facing the coolant.

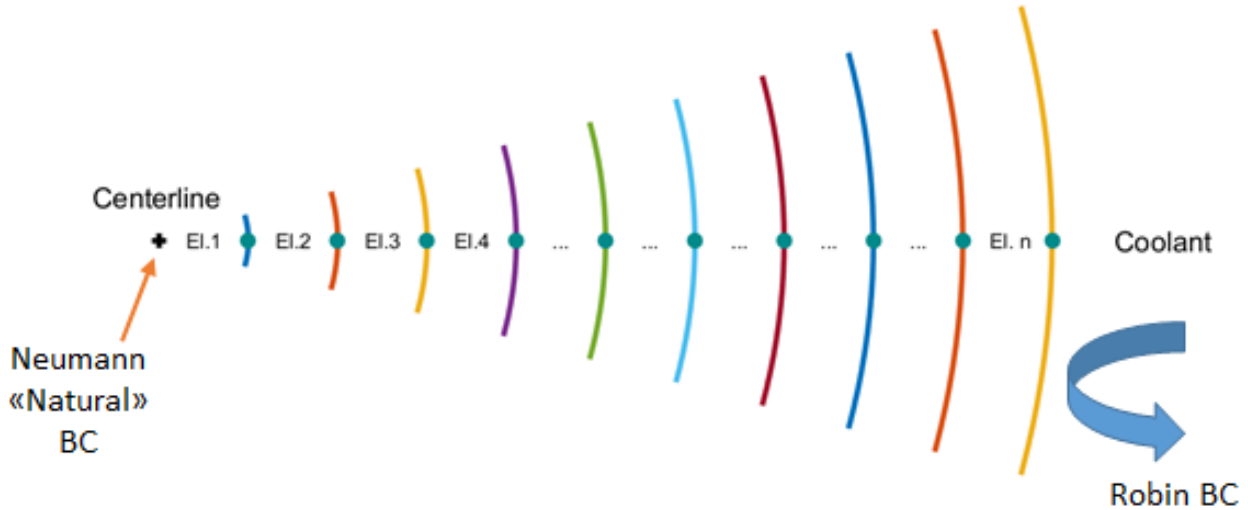


Figure 23. Finite element pin radial model schematics.

Being the model problem represented by a second order partial differential equation in space, two boundary conditions are needed to solve it:

- **INNERMOST NODE:** an adiabatic (Neumann natural) BC is prescribed, due to the symmetry of the problem:

$$\left. \frac{dT}{dr} \right|_{r=r_{in}} = 0 \quad (11)$$

- **OUTERMOST NODE:** the liquid sodium flowing inside the hexagonal assembly cools the node corresponding to the outer surface of the pin. The most suitable boundary condition to be applied to this node is therefore the Robin BC, which relates the surface temperature of the pin to the heat exchanged with the coolant. Being h the convective heat transfer coefficient of the sodium and T_{Na} its temperature:

$$-k \left. \frac{dT}{dr} \right|_{r=r_p} = h(T(r_p) - T_{Na}) \quad (12)$$

The equation is solved once per each axial node per each subassembly at every time t . The surface temperature is then used in the subsequent time step in the equation for the temperature of the coolant, using therefore an explicit coupling.

With this model, the geometrical radial distribution of the temperature inside the fuel pin is no longer forced to be parabolic but can assume a shape more representative of the state of the reactor, following the real transient evolution of the temperature profile in the pins: it is very likely, for example, that once the power driver has fell significantly after the chain reaction stop due to the reactor SCRAM, the energy stored in the pin redistributes, flattening the pin temperature profile.

3.2 Results and discussion

This section is divided in three parts: in the first one, the sets of boundary conditions used for the simulations is presented; in the second one, the improvements of the code thanks to the BIB model are shown; in the last one the improvements obtained with the pin temperature 1D radial model are described.

Both steady state and transient results are reported, referring to the Shutdown Heat Removal Test SHRT-17 of the EBR-II reactor, involving the loss-of-flow due to the trip of the primary and intermediate pumps, suddenly followed by a SCRAM (protected loss-of-flow).

3.2.1 Boundary conditions sets

The first SHRT-17 simulations after the implementation of the BIB model have been run before the experimental data of the post-blind phase of the Benchmark Exercise were made available by ANL. After that, the various participants to the Benchmark, including the ENEA, have been tuning and improving their models to better describe the phenomena involved in the transient, as the experimental measurements of physical quantities were made available.

Therefore, the FRENETIC simulations were re-run after the new, updated BCs were provided. The new run showed significant improvement in the behavior of one of the instrumented assemblies, the “hot” one, which is the XX09, while the “cold”, dummy one, became significantly worse, as if the heat transfer was overestimated by FRENETIC.

The huge difference between the two simulations showed the very high sensitivity of the solution to the accuracy of the BC data, in particular mass flow rates. For this reason, since XX09 and XX10 experimental flow rates were made available by ANL and RELAP5-3D© had also computed them, it was decided to make a study of the relative error of RELAP5-3D© results (used in FRENETIC as BCs) with respect to the experimental data to quantify the sensitivity of the FRENETIC results to the BCs.

Figure 24 and Figure 25 show that the XX10 and the XX09 flow rates computed by RELAP5-3D© are affected by a certain error with respect to the experimental values. The XX10 assembly, for which the FRENETIC results became worse using the update BCs, is the one for which the flow rate computed by the RELAP5-3D© code presents the maximum error; in the first part of the transient, between the trip of the pumps and the temperature peak (~100 s), the error gets well above 50%. In addition, being XX10 a dummy assembly (pins are made of stainless steel), flow rates absolute values are well below those of XX09, which is “hot” (fuel pins inside it): even small variations of these values may lead to huge temperature differences.

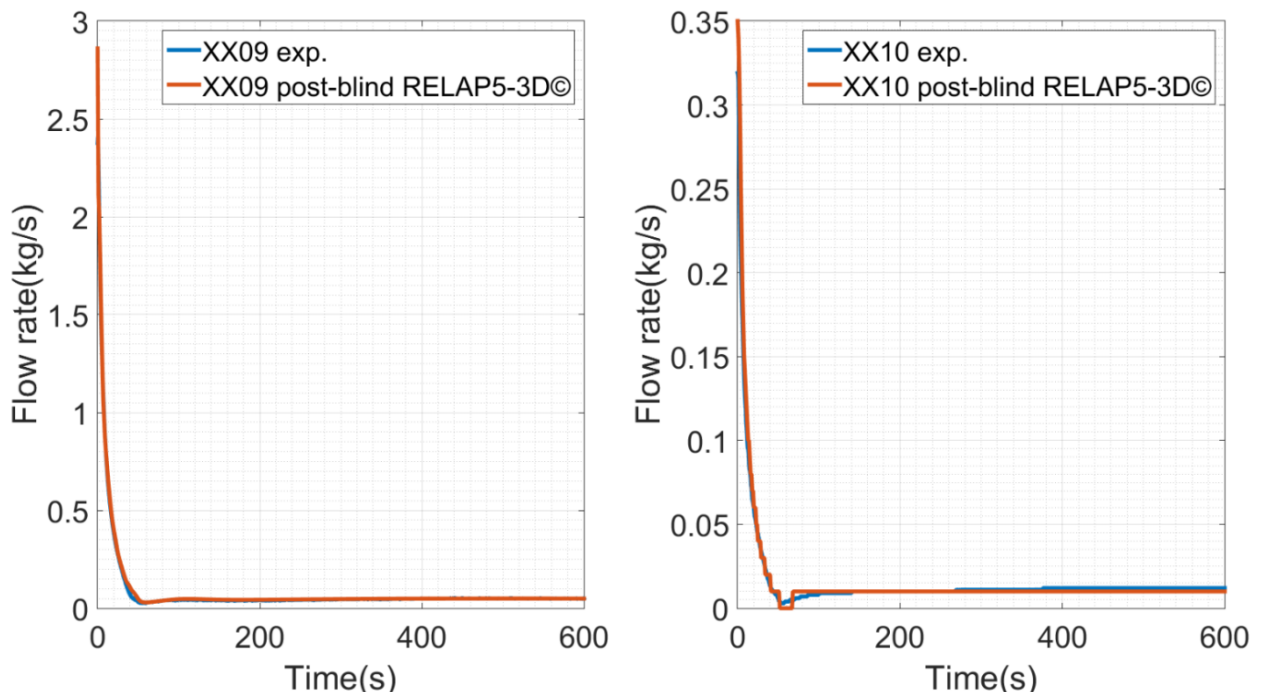


Figure 24. XX10 and XX09 flow rates: experimental values (blue lines) vs. RELAP5-3D© post-blind phase values.

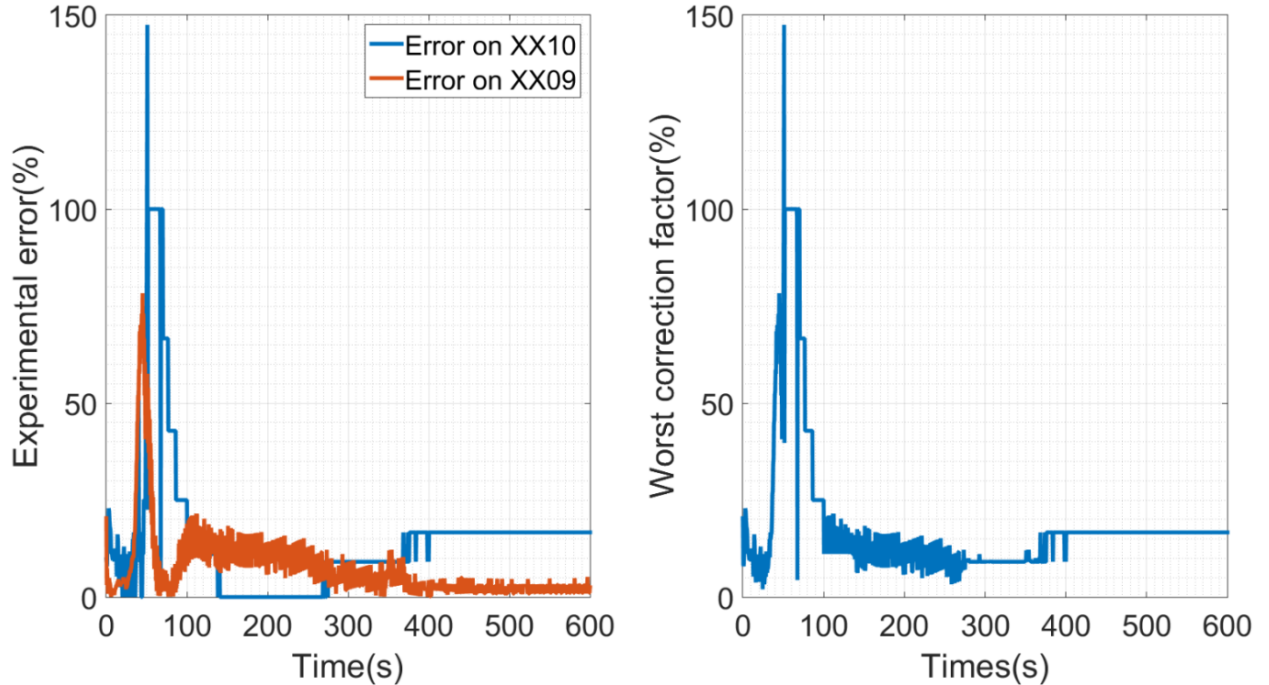


Figure 25. Relative error of RELAP5-3D© flow rates with respect to experimental flow rates in instrumented HAs XX09 and XX10 (left); correction factor used to assess the sensitivity analysis, taken as the worst of the relative errors between XX09 and XX10 (right).

For the above reasons, it became necessary to make a sensitivity analysis of the problem with respect to the flow rates data, by setting two “worst-cases” bounds to the calculation. In these cases, the entire core flow rate was increased or decreased by a certain percentage correction factor, corresponding to the worst relative error among the two instrumented assemblies XX09 and XX10, in the following way:

$$\begin{cases} \dot{m}_i^+(t) = \dot{m}_{i,RELAP5-3D\circledcirc}(t) \cdot CF(t) \\ \dot{m}_i^-(t) = \dot{m}_{i,RELAP5-3D\circledcirc}(t) \cdot CF(t) \\ CF(t) = \max \left\{ 1 - \frac{|\dot{m}_{XX09,exp}(t) - \dot{m}_{instrRELAP5-3D\circledcirc}(t)|}{\dot{m}_{XX09,RELAP5-3D\circledcirc}(t)} \right\} \end{cases} \quad (13)$$

The hypothesis lying at the base of the sensitivity analysis assessed with the above flow rates sets is that no information is known on the accuracy of the distribution of the total flow rate among the different HAs, and therefore a computed misdistribution of the flow rate of the same entity could have happened in the HAs around the instrumented ones as well. Total mass flow rates used as maximum and minimum bounds for the sensitivity study are shown along with the RELAP5-3D© non-corrected one in Figure 26.

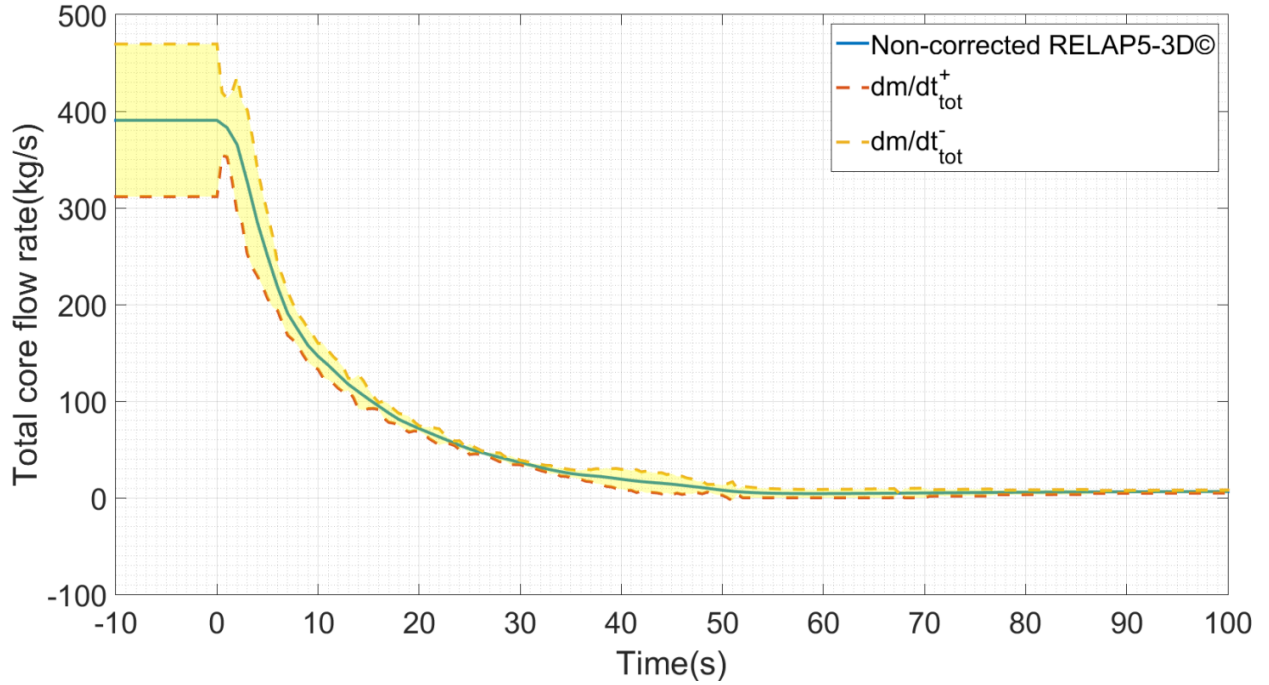


Figure 26. Comparison between the post-blind RELAP5-3D© flow rates and the corrected flow rates for sensitivity analysis m_i^+ and m_i^- .

The expected output, should the hypothesis prove correct and the misdistribution of flow rates is similar to the instrumented assembly in the neighboring zone, is to gain an improvement in XX10 behavior. The XX09 temperature profile, already well described using RELAP5-3D© BCs, may instead be worsened.

These are the different sets of BCs used in the following sections:

- **BC-1**, corresponds to the blind phase RELAP5-3D© flow rates, rescaled by the error of the RELAP5-3D© pump#2 total flow rate with respect to the experimental one. When this set was used, experimental data were already available, but RELAP5-3D© calculations had not been re-performed yet (Nov 2014). For a more detailed description of these flow rates data and their detailed results when used with FRENETIC before the BIB model implementation please refer to [12].
- **BC-2**, corresponds to the post-blind phase RELAP5-3D© flow rates without any correction.
- **BC-3**, refers to the above mentioned \dot{m}_{in}^+ , where the post-blind phase RELAP5-3D© flow rates have been increased by a correction factor that takes into account the error of RELAP5-3D© with respect to experiments on instrumented assemblies.
- **BC-4**, refers to the above mentioned \dot{m}_{in}^- , where the post-blind phase RELAP5-3D© flow rates have been reduced by a correction factor that takes into account the error of RELAP5-3D© with respect to experiments on instrumented assemblies.

The experimental flow rates are superimposed in each of the cases in XX09 and XX10 HAs. The above flow rates boundary conditions sets are summarized in Table 1.

Table 1. Summary of the flow rates data sets used for the various FRENETIC simulations.

Name	Flow rates description
BC-1	dm/dt_{in} from RELAP5-3D© (Blind phase) rescaled according to the ratio between experimental and RELAP5-3D© for pump#2
BC-2	dm/dt_{in} from RELAP5-3D© (Post-Blind phase)
BC-3	dm/dt_{in} from RELAP5-3D© (Post-Blind phase) increased by the maximum relative difference between the experimental and RELAP5-3D© data in instrumented HAs
BC-4	dm/dt_{in} from RELAP5-3D© (Post-Blind phase) decreased by the maximum relative difference between the experimental and RELAP5-3D© data in instrumented HAs

3.2.2 Box-in-the-box results

In the following section, steady state and transient results are reported separately. In the last subsection a heat transfer interpretation of the model effectiveness is presented.

Results refer to XX09 and XX10 instrumented assemblies of the EBR-II reactor that were present in the core at the time of the test, the first being a fuelled assembly and the second being a dummy (stainless steel pins) one for which experimental data were made available within the framework of an international IAEA Benchmark.

3.2.2.1 Steady state

The steady state ($t = 0$ s, before the start of the transient) distributions of temperature along the axial coordinate of the instrumented assemblies XX09 and XX10 are presented in Figure 27 and Figure 28.

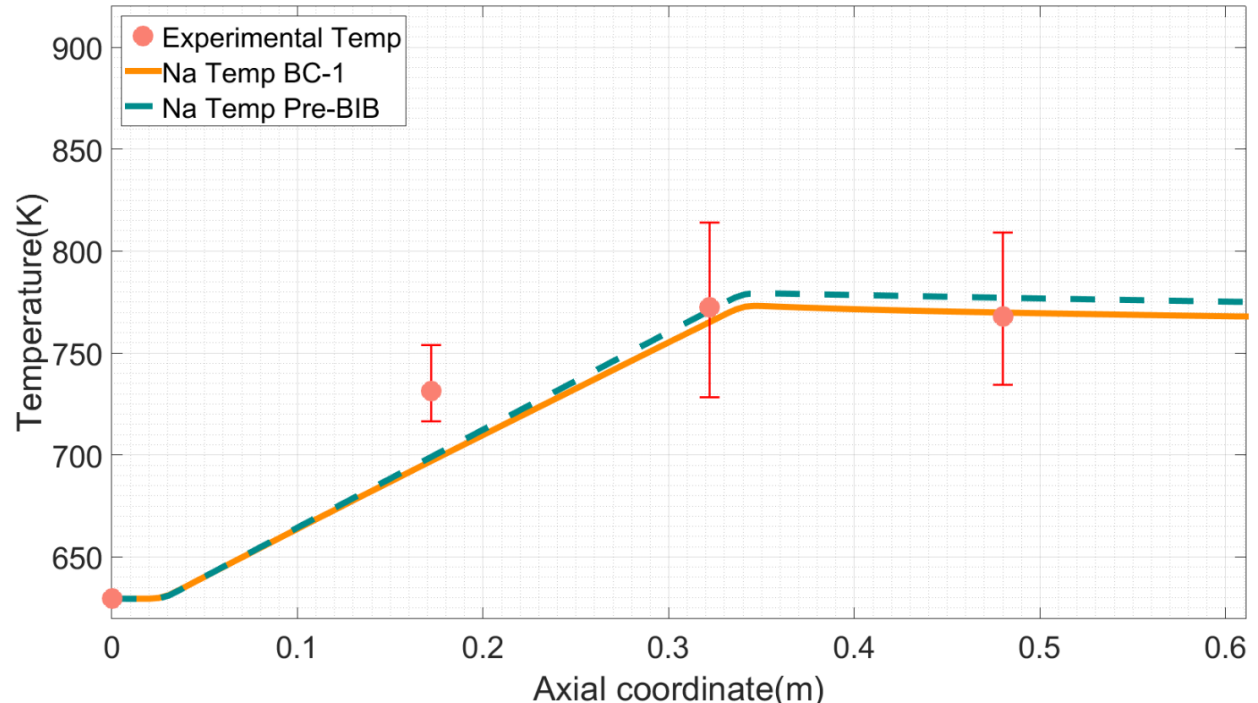


Figure 27. Steady state axial temperature distribution in instrumented assembly XX09: comparison between old (pre-BIB) model and new BIB model, with the same set of flow rates boundary conditions (BC-1).

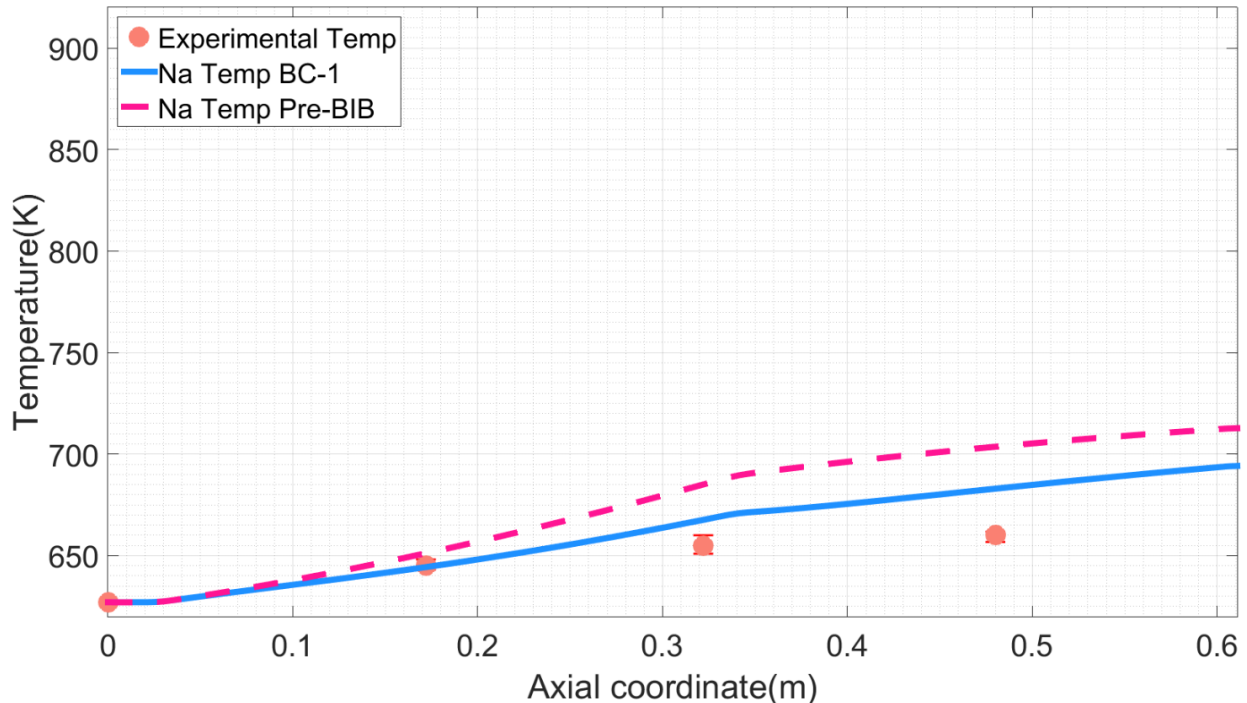


Figure 28. Steady state axial temperature distribution in instrumented assembly XX10: comparison between old (pre-BIB) model and new BIB model with the same set of flow rates boundary conditions (BC-1).

The new BIB model brought a slight improvement in the steady state axial distribution of temperatures in both the assemblies. It must be noted that the underestimation at the mid-core height ($MTC = 0.322$ m) is due to the assumption, suggested by Argonne, that the input power should be uniformly distributed over the core active length.

XX10 is more affected than XX09 by the presence of the thimble. This goes into the expected direction considering the following two elements:

- With respect to the old model, a higher flow rate is considered, the one flowing inside the thimbles of XX10 and XX09. A portion of the power generated in the surroundings of XX10 (which is “colder” than its surrounding HAs) and of XX09 (which is somewhat at an average temperature with respect to its surrounding HAs) is extracted from the core by the thimble flow rate, therefore reducing the temperature of both of them. The steady state linear power distribution in the surroundings of instrumented assemblies is shown in Figure 29.

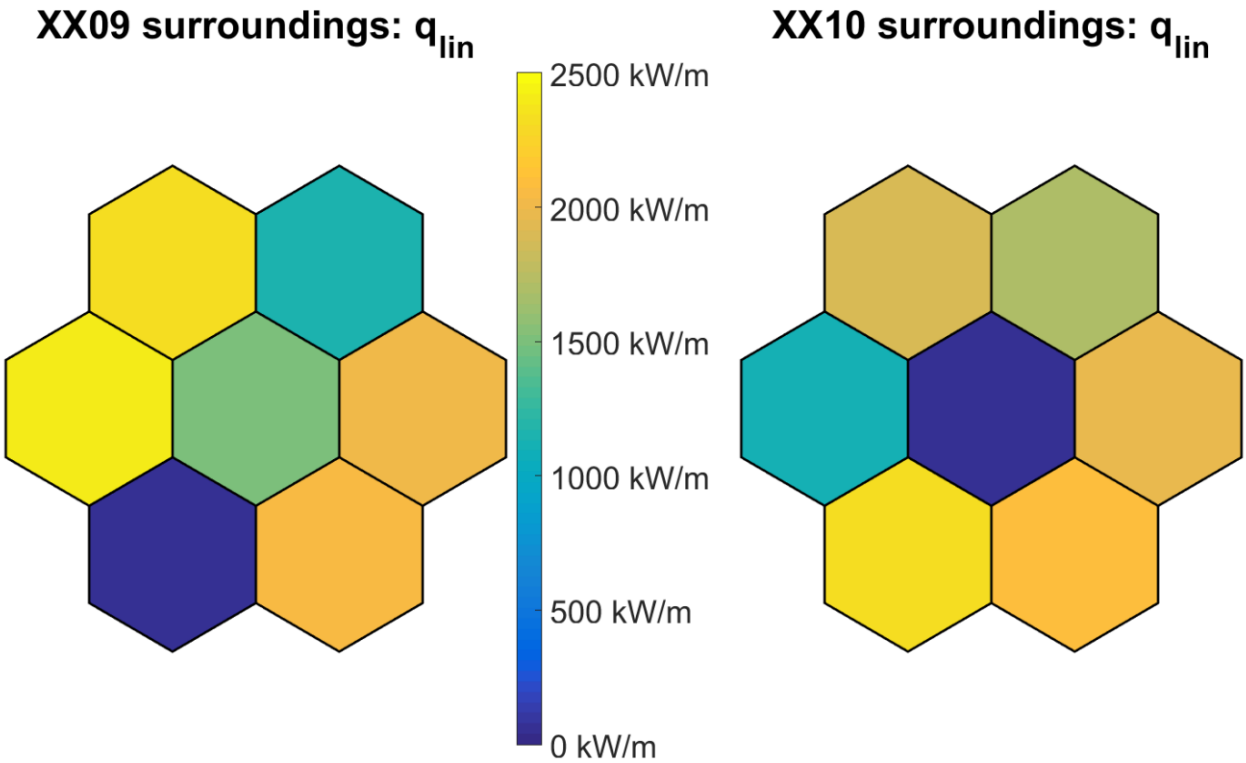


Figure 29. Steady state linear power (kW/m) distribution in the surroundings of instrumented assemblies XX09 and XX10.

- Referring to Figure 18, the relative weight of the thimble flow rate in XX10 assembly is higher than in XX09. For this reason the improvement of XX10 behavior is more evident than that of XX09, which anyhow falls in a very wide range of experimental values coming from the thermocouples.

Even if the situation has got better, the simulated XX10 still reaches a too high temperature both in the active region of the core (where it should be below the experimental one due to the above stated hypothesis of the power uniformly distributed) and in the upper, non-heated, part of the domain.

Once the experimental data were available from ANL, after the blind phase of the IAEA-CRP, the boundary conditions were recomputed by ENEA with RELAP5-3D, and a new simulation on FRENETIC was set, with the so-called BC-2 flow rates. Contrarily to BC-1, where data were rescaled to take into account the relative difference between the experimental and RELAP5-3D© pump behavior (experimental data were already available but new BC had not yet been sent by ENEA), in BC-2 rough data from RELAP5-3D© have been adopted without any rescaling.

These data were tuned on experimental results and therefore are supposed to be more accurate than BC-1 data. BC-2 steady state temperature axial distributions are shown in Figure 30 and Figure 31 for instrumented assemblies XX09 and XX10.

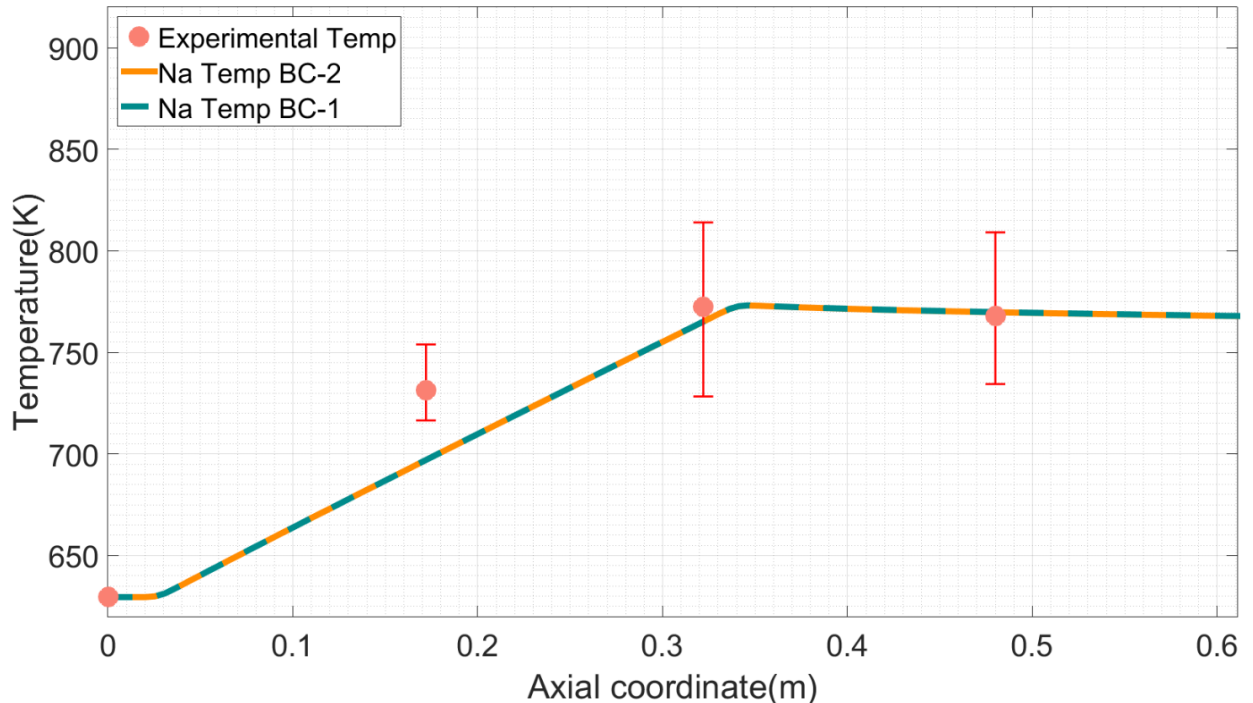


Figure 30. Steady state axial temperature distribution in instrumented assembly XX09: comparison between BC-1 and BC-2 sets of flow rates boundary conditions.

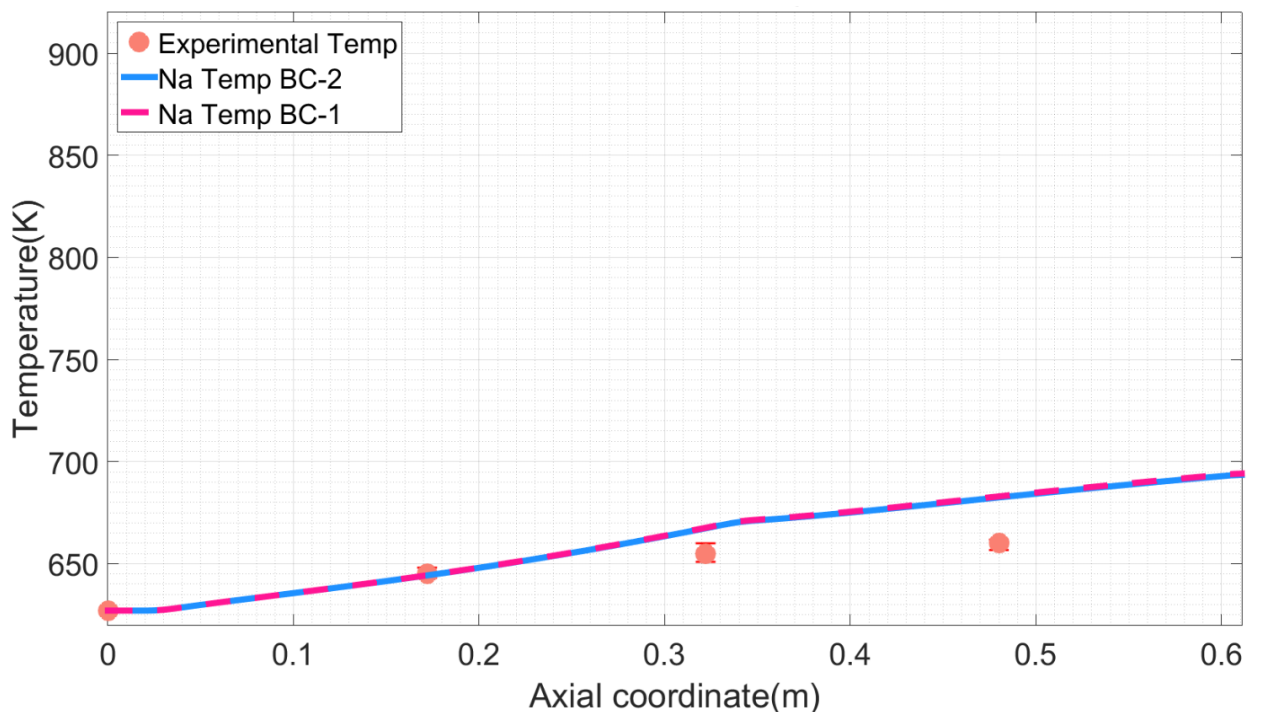


Figure 31. Steady state axial temperature distribution in instrumented assembly XX10: comparison between BC-1 and BC-2 sets of flow rates boundary conditions.

No improvement is actually reached at steady state with the new set of flow rates.

The error made on XX10 with both data sets BC-1 and BC-2 may still be related to an overestimation of heat transferred to the dummy instrumented assembly from its neighboring ones, that are hotter as shown in Figure 29. Providing FRENETIC with BC-2 and comparing the computed results to those of RELAP5-3D© (post-blind phase) it can be noticed that those

assemblies that the worst represented HAs are actually the stainless steel, dummy ones. This situation is summarized by Figure 32 and Figure 33, where FRENETIC results using BC-2 are compared with RELAP5-3D© steady temperatures at the outlet of the core (obviously with the same flow rates).

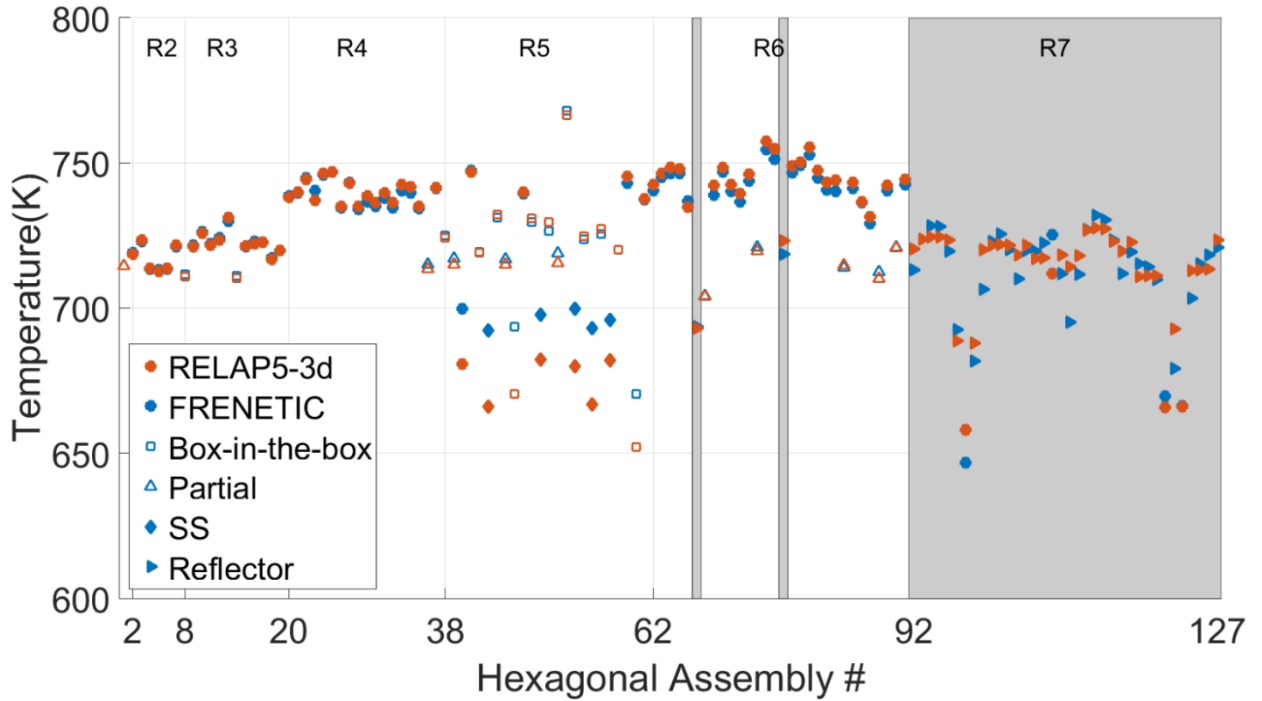


Figure 32. Steady state distribution of outlet temperatures: FRENETIC vs. RELAP5-3D© (BC-2).

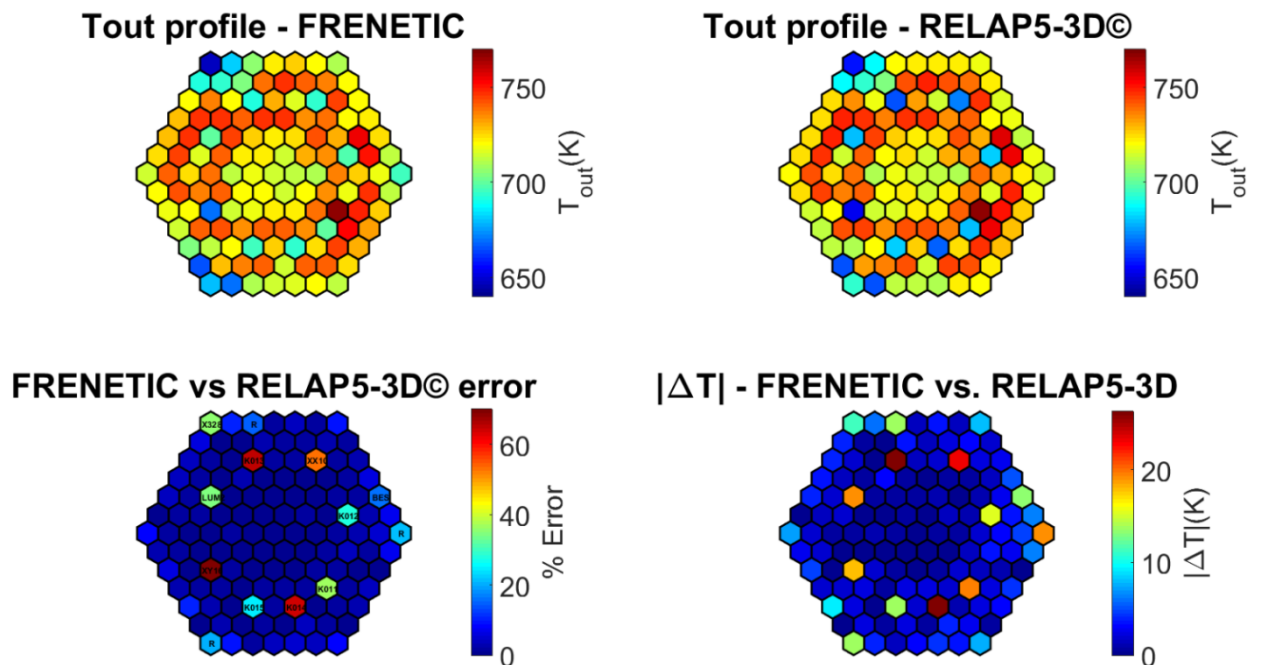


Figure 33. Steady state distribution, % error and absolute ΔT of outlet temperatures on the horizontal plane: FRENETIC vs. RELAP5-3D© (BC-2).

Since, anyhow, the RELAP5-3D© post-blind phase flow rates in the instrumented assemblies showed some inconsistencies with the experimental data provided by ANL and no information on the accuracy of the flow rates calculation can be retrieved for the rest of the core, a sensitivity

analysis has been carried out. Two new BC sets (BC-3 and BC-4) were conceived, that would take into account of the worst error of RELAP5-3D© with respect to known experimental data in both direction (increasing and decreasing the total flow rate). The detailed description of these new sets is provided in Table 1. Results using BC-3 are compared to the ones obtained with BC-2 in Figure 34 and Figure 35.

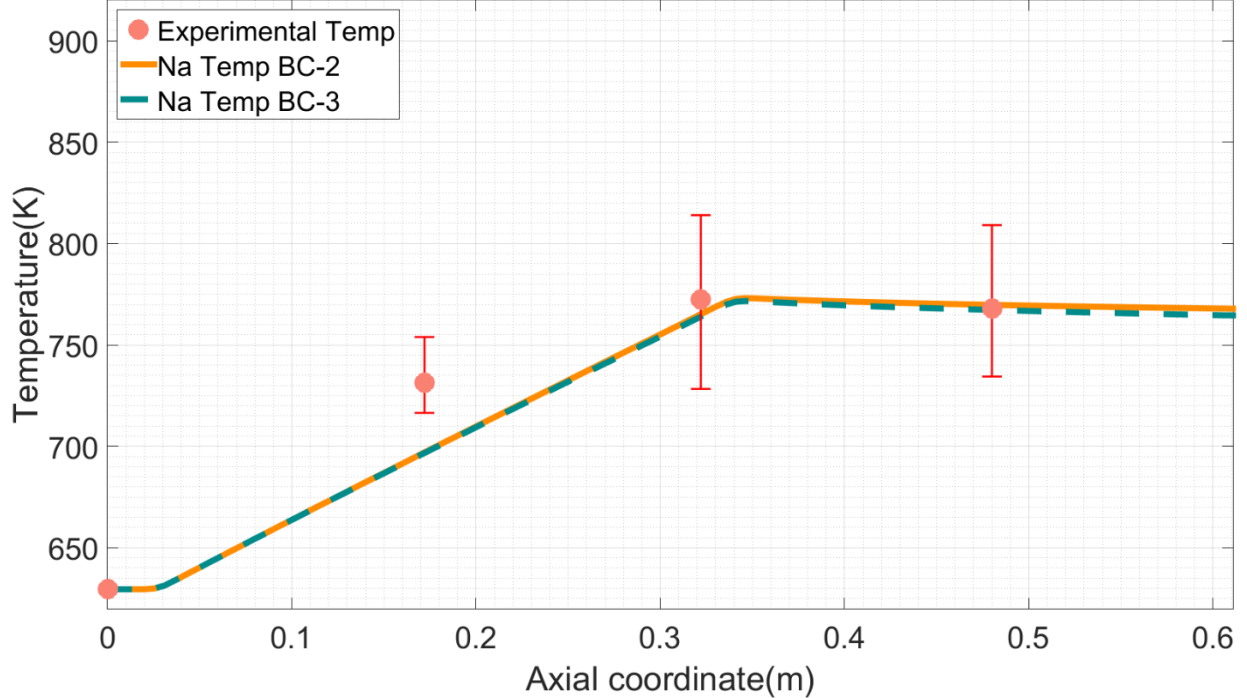


Figure 34. Steady state axial temperature distribution in XX09: comparison between BC-2 and BC-3 sets of flow rates conditions.

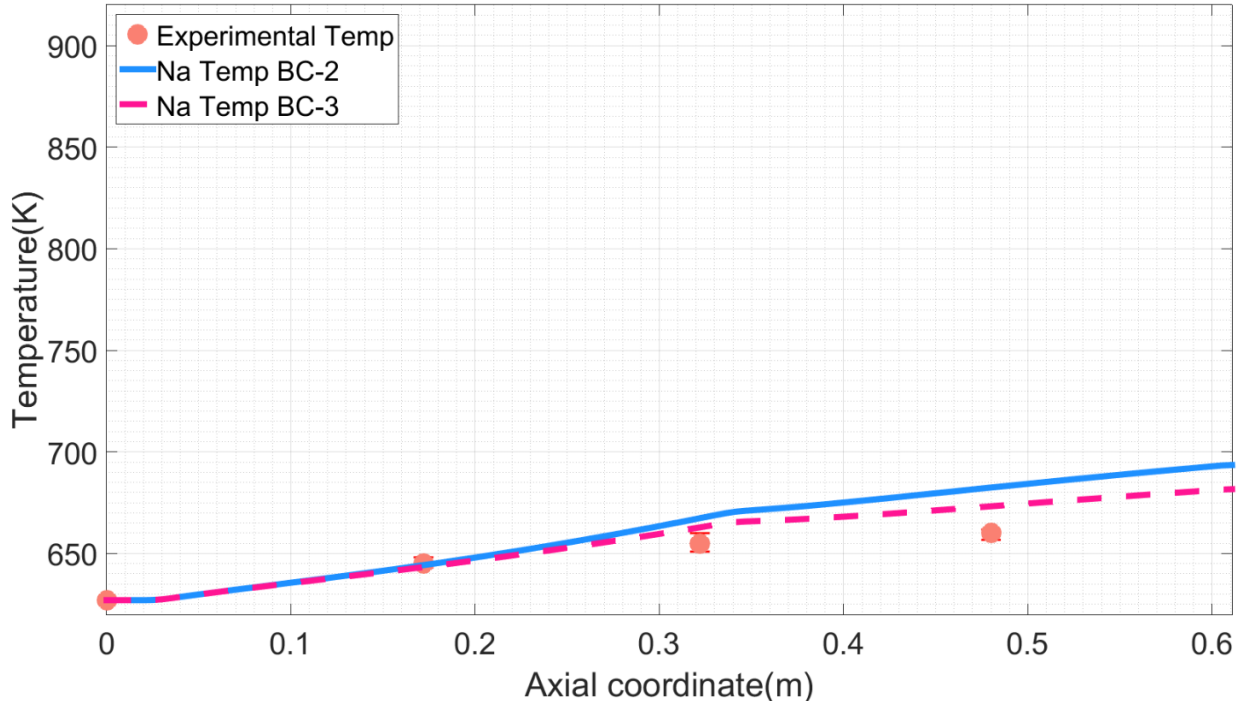


Figure 35. Steady state axial temperature distribution in XX10: comparison between BC-2 and BC-3 sets of flow rates conditions.

The ~20% increase in the flow rates that has been applied to the BC-2 set to obtain BC-3, brought almost no effect to the steady state axial temperature distribution of XX09 while it showed a non-negligible improvement in XX10 behavior. Since the RELAP5-3D© overestimated XX10 flow rate, if the overestimation is due to a misdistribution of flow rates in that region of the core (i.e. due to inlet orifices or the underestimation of other pressure losses) this could mean that the neighboring subassemblies are less cooled than they should, if the total flow rate is kept constant. If this is verified, increasing the neighboring flow rates keeping the XX10 flow rate constant and equal to the experimental one (as did by BC-3) should go in the right direction.

BC-4 results are not reported since the flow rate reduction obviously worsened the temperature profiles, both in steady state and during the transient. This is in line with the above mentioned phenomenological hypothesis.

3.2.2.2 Transient

In this section the transient results will be shown in the same succession as in the steady state chapter. All the figures will show the temperature evolution at a specific axial location, referred as TTC (Top-of-Core, $z = 0.322$ m). Flow rates data sets are identified by plots' legends, Figure 36 and Figure 37 show the differences coming from the introduction of the BIB model using BC-1. As already stated, the flow rates used for the pre-BIB simulation are equal to BC-1 except for neglecting thimble flow rates.

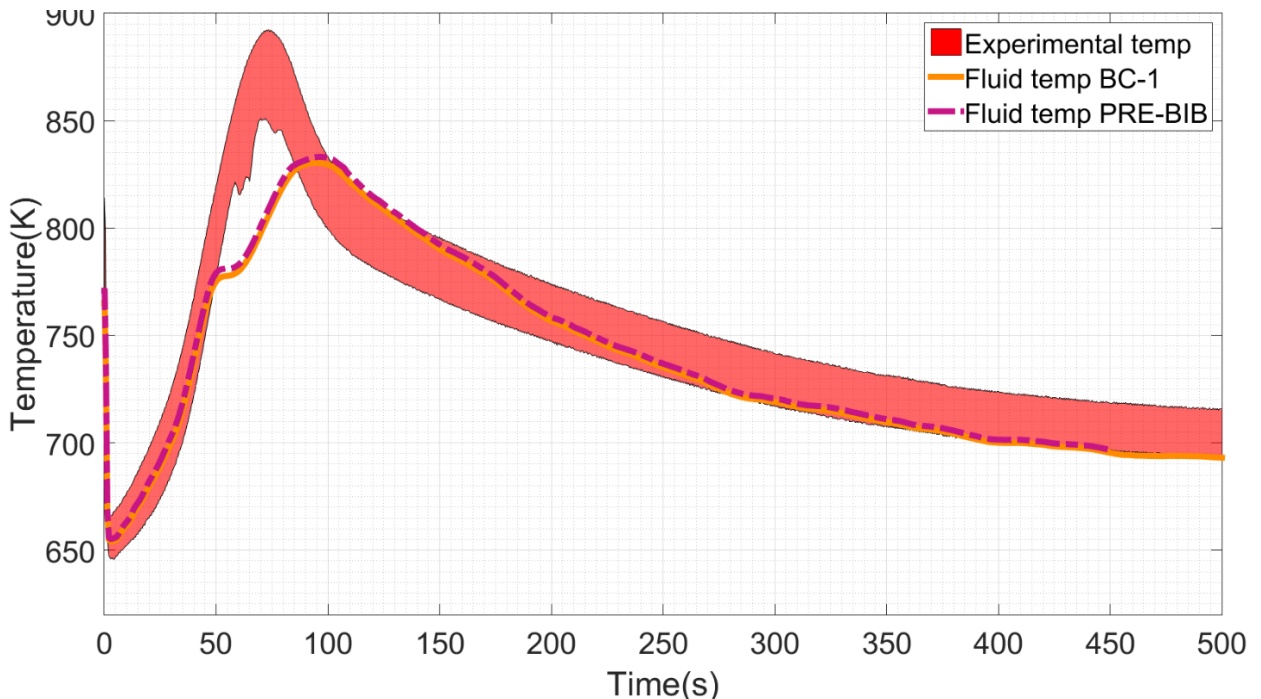


Figure 36. Temperature evolution at Top-of-Core (TTC, $z = 0.322$ m) height in XX09: comparison between pre-BIB model and new BIB model with BC-1 flow rates boundary conditions.

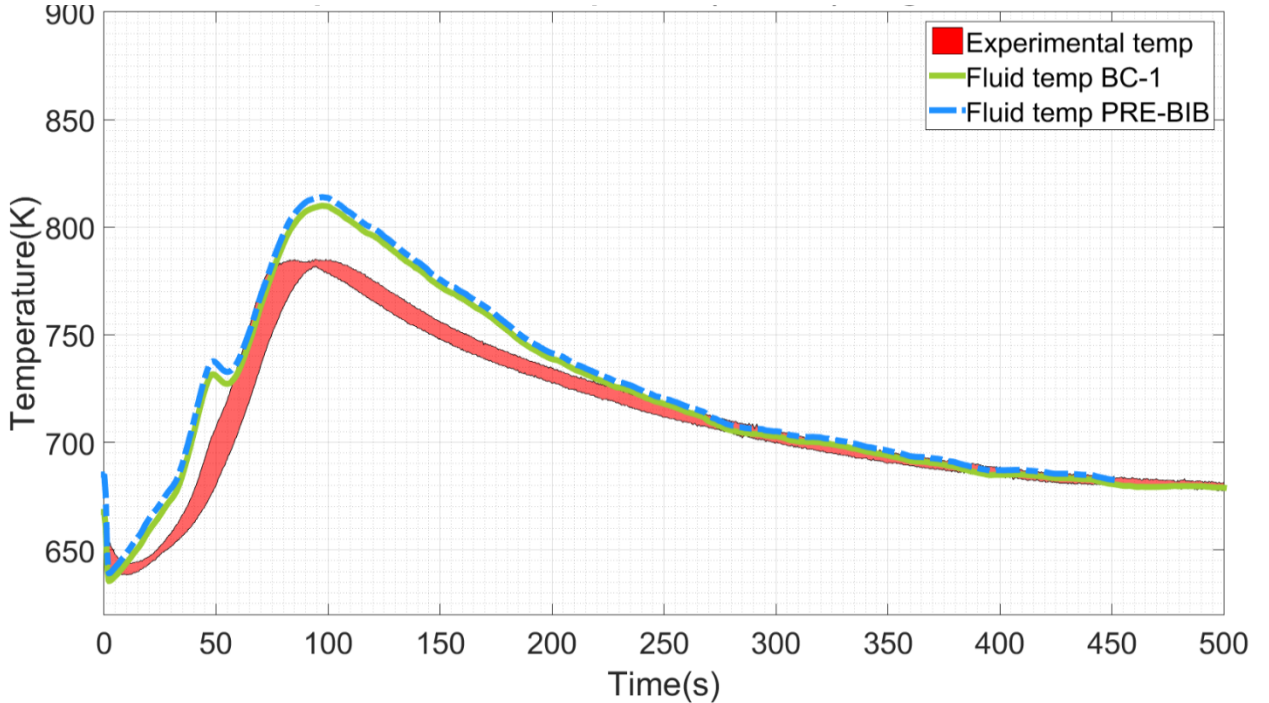


Figure 37. Temperature evolution at Top-of-Core (TTC, $z = 0.322$ m) height in XX10: comparison between pre-BIB model and new BIB model with BC-1 flow rates boundary conditions.

Contrarily to steady state where some improvements were obtained by the implementation of the new BIB model, the transient is practically not affected by the sodium flowing inside the thimble of the instrumented assembly.

The transient, as well as the steady state, has been recomputed after receiving the new data (BC-2) from ENEA, improved thanks to the experimental data made available by ANL. BC-2 results are compared to BC-1 in Figure 38 and Figure 39.

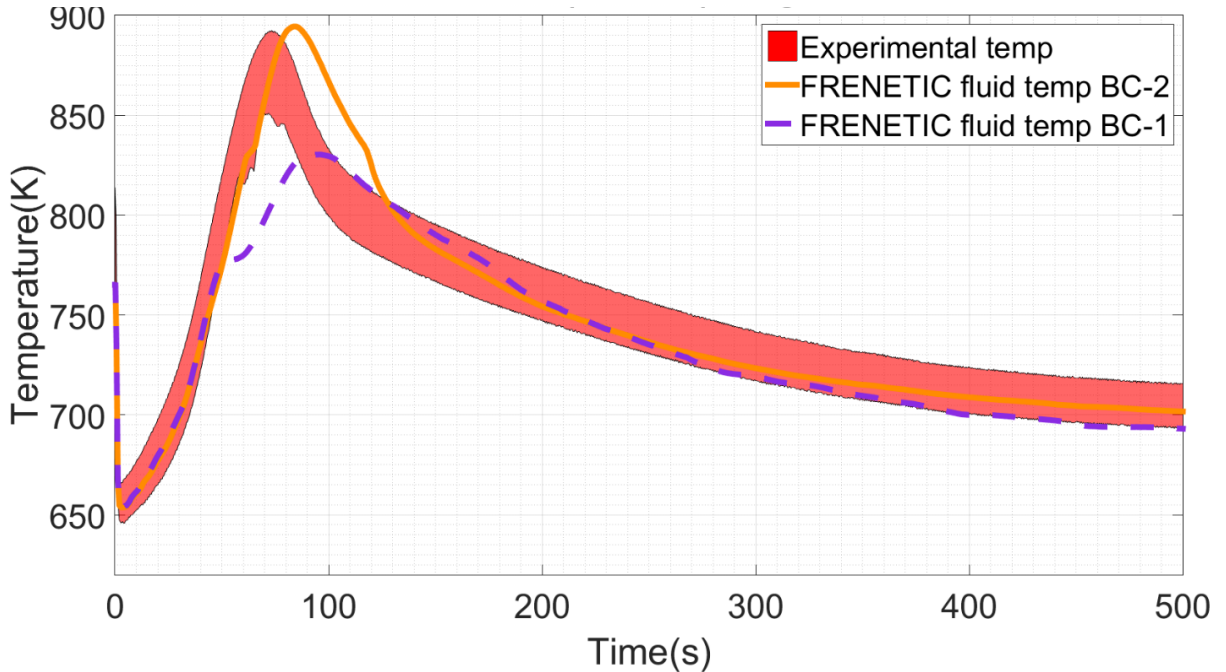


Figure 38. Temperature evolution at Top-of-Core (TTC, $z = 0.322$ m) height in XX09: comparison between BC-2 and BC-1 flow rates.

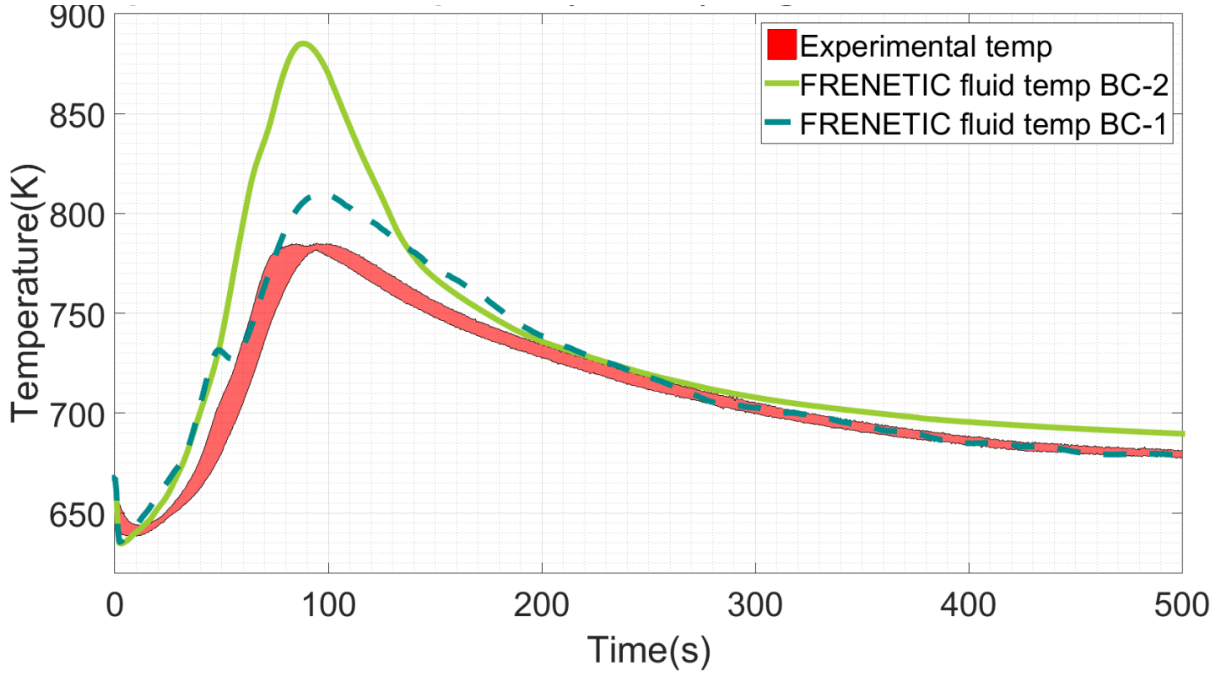


Figure 39. Temperature evolution at Top-of-Core (TTC, $z = 0.322$ m) height in XX10: comparison between BC-2 and BC-1 flow rates.

With the post-blind phase flow rates (BC-2), the instrumented assembly XX09 (which is the fuelled one) is very well represented by FRENETIC: the experimental temperature peak is closely gotten by the computed curve, and in general the curves always stay very close, even if the computed one is a little out-of-phase in hitting the peak and in the descendant part.

XX10 situation is instead worsened, making evident the huge sensitivity of results to flow rates boundary conditions. This is in line with what found beforehand in Section 3.2.1, where it was shown that the BC-2 flow rates computed by RELAP5-3D© made a significant error with respect to experimental ones in particular in the first peak-phase of the transient.

This was at the base of the already described sensitivity study made with BC-3 and BC-4 flow rates (Table 1). The results are shown in Figure 40 and Figure 41.

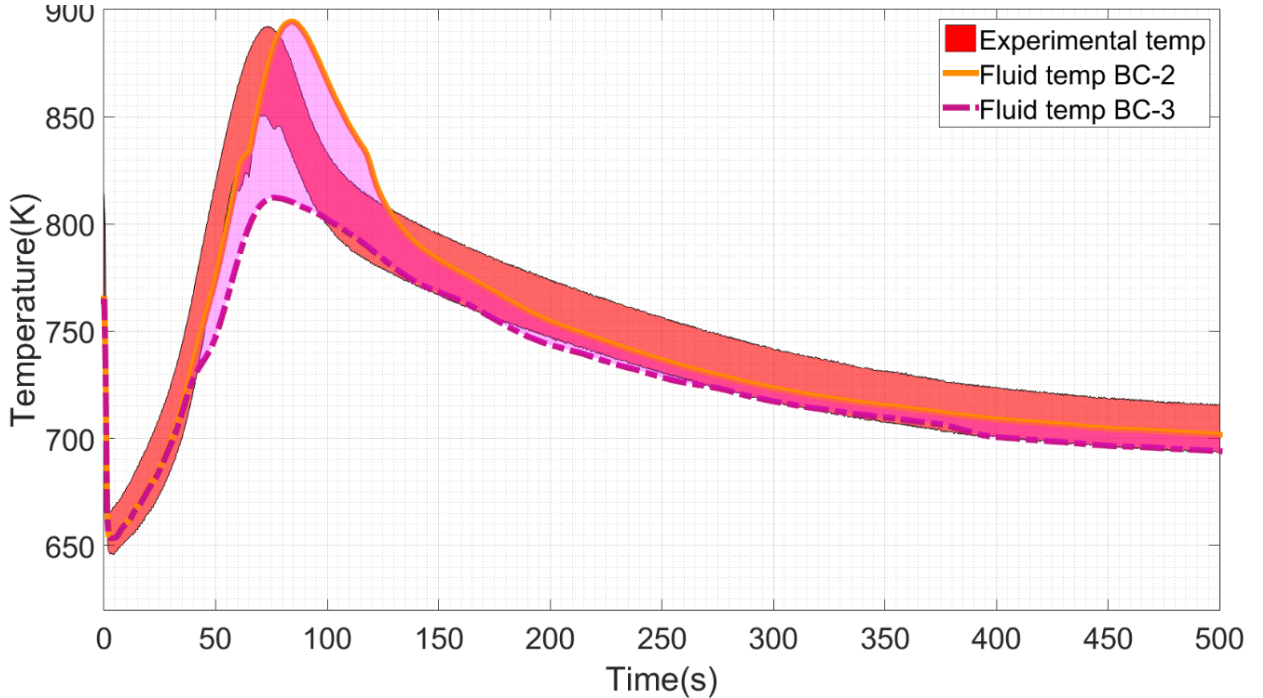


Figure 40. Temperature evolution at Top-of-Core (TTC, $z = 0.322$ m) height in XX09: comparison between BC-3 and BC-2 flow rates.

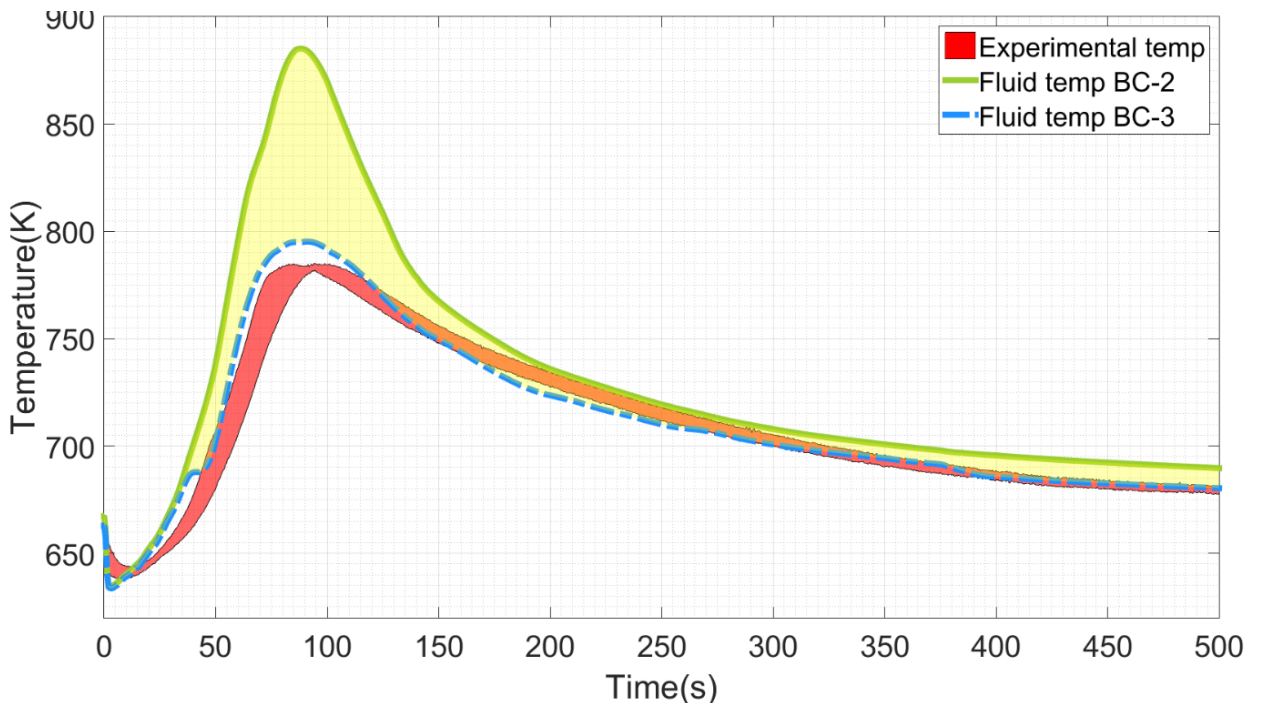


Figure 41. Temperature evolution at Top-of-Core (TTC, $z = 0.322$ m) height in XX10: comparison between BC-3 and BC-2 flow rates.

As expected by the phenomenological discussion on how they were derived, BC-3 flow rates describe XX10 HA very closely. The correction factor applied to BC-2 to obtain BC-3 and BC-4 was, in fact, derived by the maximum experimental error among the ones on XX10 and XX09, which indeed was the one on the “cold” dummy assembly. For the same reasons, since XX09 flow rates were already close enough to the experimental values computed by RELAP5-3D© and since the correction was applied to all the assemblies of the core, XX09 appears too cold in

the BC-3 simulation due to the increase of the flow rates in its neighboring HAs. The experimental values are anyhow almost always bracketed or captured by BC-2 and BC-3 curves.

BC-4 is not reported in the above plots since the results showed an overestimation of the temperature evolution in both the instrumented assemblies. This goes in the expected direction: if the hypothesis and assumptions made in Section 3.2.1 on the nature of the error made by RELAP5-3D© with respect to experimental flow rates proves right, decreasing the flow rate of the assemblies in the surroundings of XX09 and XX10 especially takes the opposite effect in “correcting” the error.

From the above results, it is evident that the quality of the results strongly depends on the flow rates boundary conditions and that the FRENETIC code is able to predict and bracket the evolution of the experimental curves within the uncertainties range of the input.

The lack of difference in the SHRT-17 behaviour simulated with the new BIB model compared to the previous model is due of its great temperature uniformity after the SCRAM has taken place. This effect is due to the very low power driver after the protection system has intervened. However, this is not verified during those transients in which the power does not decrease, for example the SHRT-45R where the reactor is not scrammed. In that situation the difference among the linear power deposited in different channels would lead to a stronger temperature difference among neighboring assemblies and therefore the above mentioned model will still be valid and the thimble would have a non-negligible impact on the solution.

Since in LMFBR full power transients are the most feared and plausible transients due to the positive coolant temperature feedbacks and displacement feedbacks, the BIB model is not a useless feature but an important addition. Reactivity insertion accidents, in fact, usually feature very localized power bursts, that enhance inhomogeneity and for which such a BIB model would better describe the heat transfer phenomena involved.

3.2.3 Radial pin model results

The BC-2 data set has been applied to the simulation with the new pin radial model. The first check that has been made was to verify that, at steady state, the numerical solution behaved as the analytical one considering the geometry of the pin as a full cylinder (Section 3.1.2).

The model has been applied to the steady state situation in this reduced configuration and, after that, data were collected at a specified axial location ($z = 0.16$ m, which is approximately one half of the heated zone): the temperature of the coolant and the convective heat transfer coefficient computed by FRENETIC have been used as input parameters for the analytical solution evaluation.

Starting from the differential heat conduction equation in cylindrical geometry, at steady state

$$\frac{1}{r} \frac{d}{dr} \left(kr \frac{dT}{dr} \right) = -q_v \quad (14)$$

where r is the radial coordinate and q_v is the volumetric heat generation in the pin. Then, considering a constant heat conductivity of the pin, we get

$$T(r) = T_{Na} + \frac{q_v}{4k} (r_{out}^2 - r^2) + \frac{q_v r_{out}}{2h} \quad (15)$$

where r_{out} is the radius of the pin. Since the actual thermal conductivity is a function of temperature, the two analytical curves are reported for the minimum and maximum values of k : if the model performs well, the computed solution should lay between these two curves. The error was evaluated with respect to the curve at maximum conductivity, as follows:

$$\epsilon = \frac{\text{norm}(\Delta T_{\max-\min,an}(r_i) - \Delta T_{\max-\min,comp}(r_i))}{\text{norm}(\Delta T_{\max-\min,an}(r_i))} \quad (16)$$

Computed results against analytical full cylinder solution are shown in Figure 42.

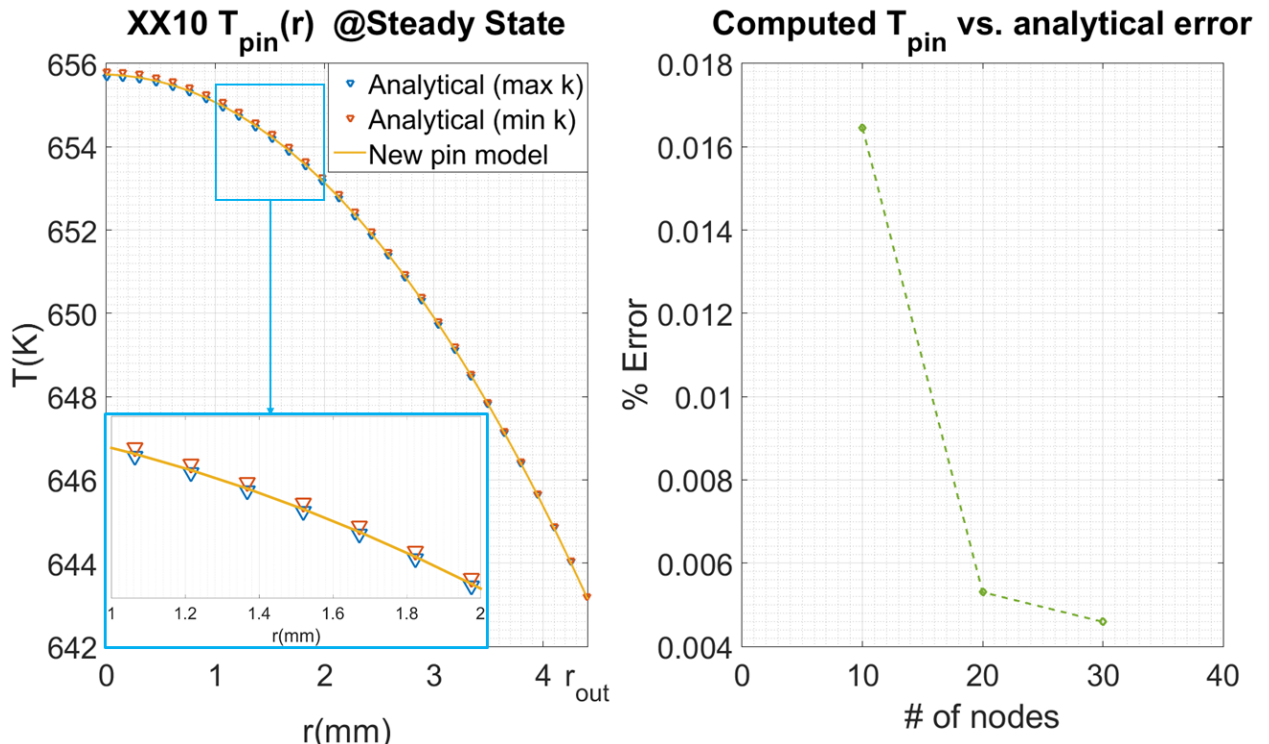


Figure 42. XX10 steady state distribution at a height $z = 0.16$ m with new radial model vs. full cylinder analytical solution and error with respect to analytical solution.

As it can be noticed, the computed curve is perfectly bracketed between the two analytical ones (max k and min k). The error on the analytical solution (max k) reduces rapidly when the number of nodes of the pin radial discretization increases, as expected.

At steady state, the old model performed well because the parabolic profile represents actually the analytical solution of the cylindrical problem. The difference brought by the model lays in transient temperature distributions inside the pin, when the driver is removed and the profile loses its parabolic shape due to the thermal inertia term of the transient equation and the profile tends to flatten (Figure 43).

At time $t = 0$ s (steady state), the two profiles are overlapping. This is what is expected, since the parabolic assumption is true when the transient term of the conduction equation is off. At time $t = 50$ s, being the temperature increasing due to mass flow reduction, the heat has to diffuse through the pin again after the initial redistribution due to the scram. This accumulation of heat in the radial direction was neglected with the old model, and the pin increased its temperature as a whole, therefore the rate of increase was faster (Figure 43).

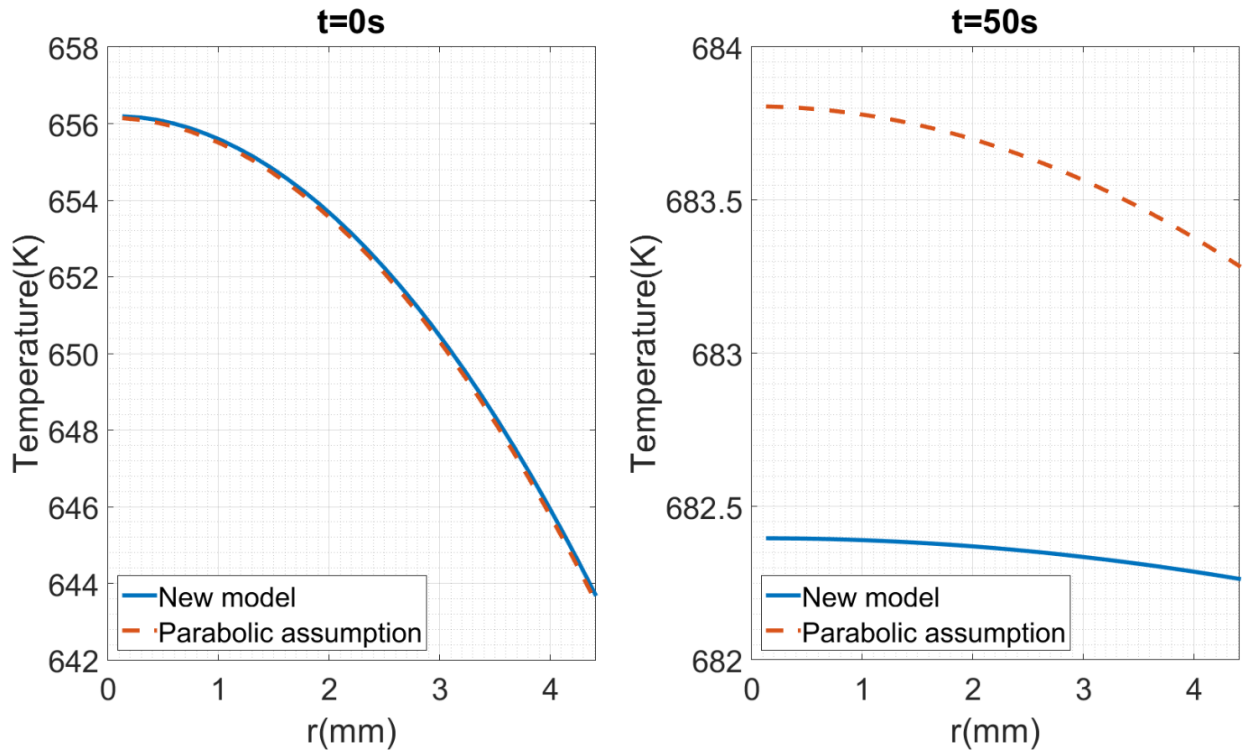


Figure 43. Pin radial temperature distributions at different times w/ and w/o the new FEM radial model (left $t = 0$ s and right $t = 50$ s).

The opposite happens after the peak is reached: the temperature starts to decrease (Figure 44) earlier in the simplified (old) model than in the FEM model (the temperature is lower). The difference in heat diffusion between the two models causes the surface temperatures of the pin to differ in the two models of about 5 K at $t = 100$ s. As time goes by ($t = 150$ s) and temperature keeps decreasing, the distance between the two curves is reduced: this is due to the fact that a new equilibrium situation is being approached. When this will be reached, at the end of the transient, the two curves would eventually overlap again for the already mentioned reasons.

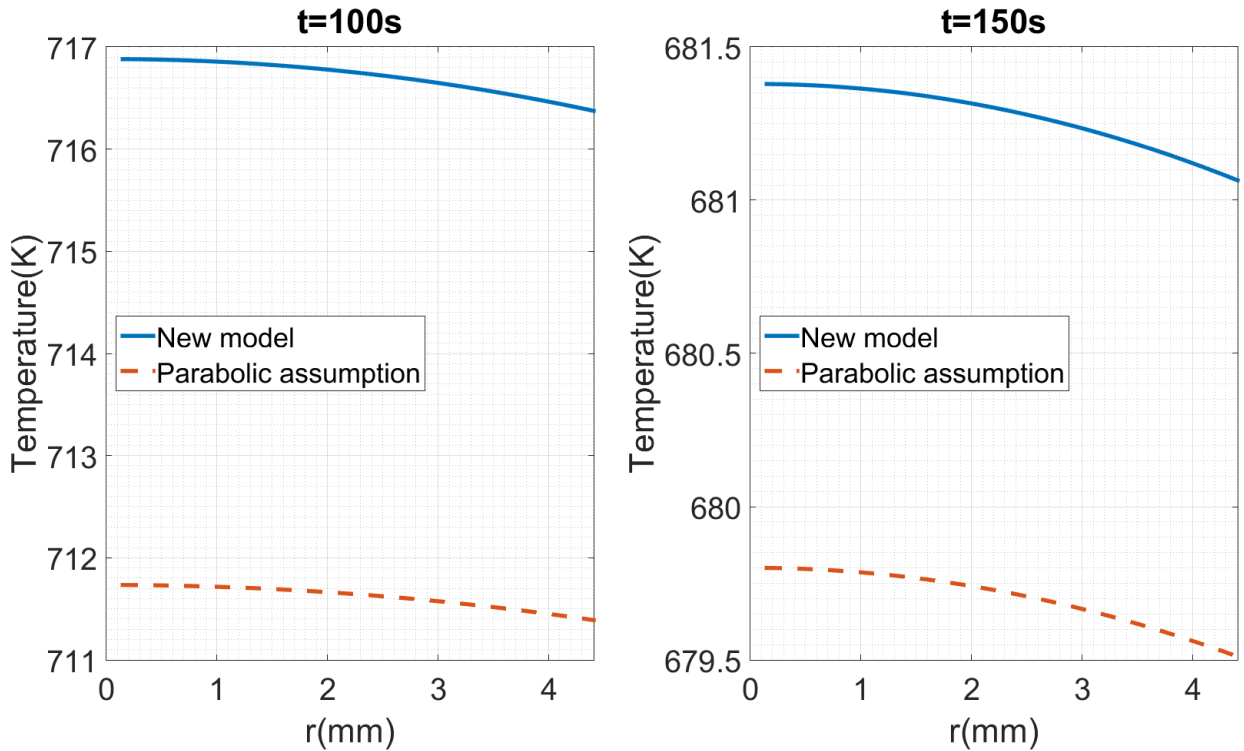


Figure 44. Pin radial temperature distributions at different times w/ and w/o the new FEM radial model (left $t = 100$ s and right $t = 150$ s).

The steady state axial distribution of temperatures and the temperature evolution at Top-of-Core height ($z = 0.322$ m) are reported and compared against the experimental data with and without the new pin radial model implementation in Figure 45, Figure 46, Figure 47 and Figure 48.

As expected, the two solutions almost coincide at steady state: it may be recalled, that this is because the simplified (old) model accounted for a parabolic temperature distribution inside the pin, which is actually the steady state solution of the cylindrical problem. The small differences (~ 1 K) in the two curves are due to the fact that, in this model, the axial conduction along the axial direction of the pin is neglected.

The transient shows a difference of 10-15 K with respect to the previous model: this is due to the weight of heat diffusion through the fuel pin, which was absent before. The slope of the increase in coolant temperature is a little less steep, since heat needs more time to diffuse inside the solid. Since the geometrical diffusion of heat is still ongoing when the peak of temperature is hit and the curve of temperature changes its sign, the maximum temperature is lower than that computed with the previous simplified model. The descendant part of the curve is, again, less steep for the same above reasons, up to the point that the new solution eventually gets over the old one obtained through the simplified model, because a new steady state solution (and therefore represented by a parabolic distribution) is reached.

The relatively small effect obtained by the implementation of the new model is again due to the low power deposition inside fuel pins which is only due to the decay heat. For un-scrammed transients, where the power deposited in the fuel pins during the loss-of-flow is comparable with that of the reactor at full power (such as SHRT-45R), the difference between the two models will be higher.

The solution, no matter how small is the improvement obtained in the application to the SHRT-17 transient, goes in the expected direction since it damps the height of the temperature peak, which was overestimated by the FRENETIC code.

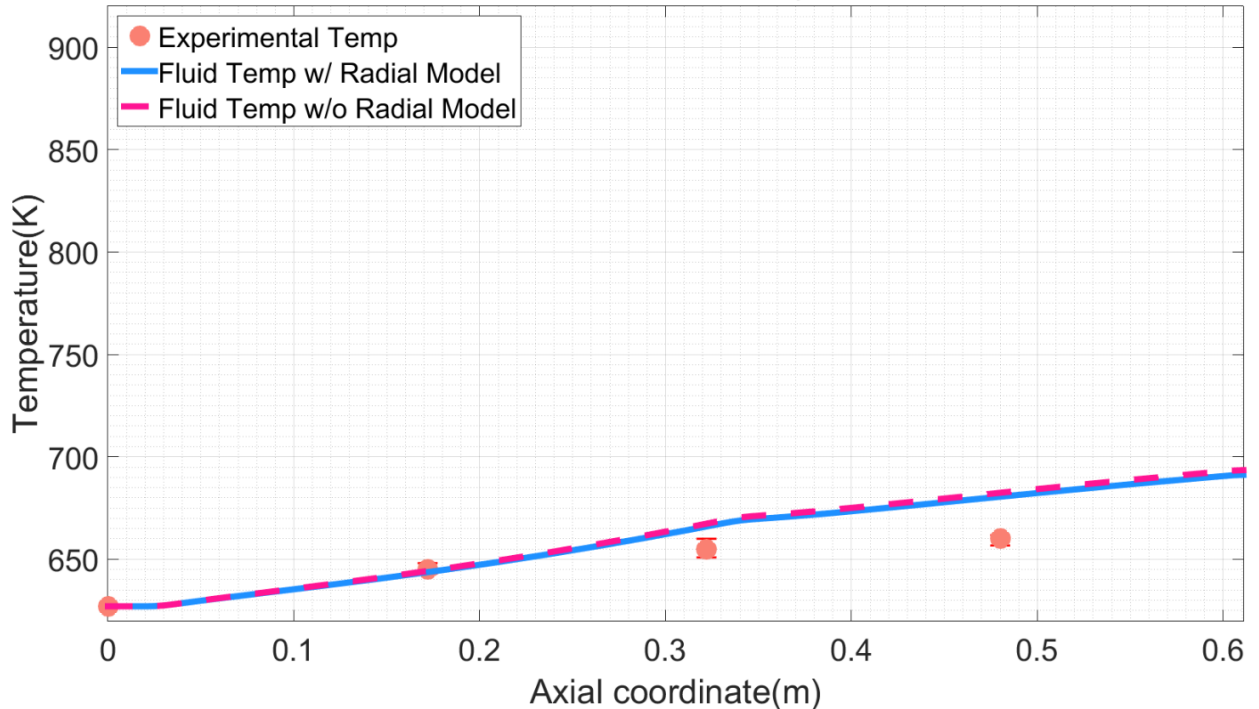


Figure 45. XX10 steady state temperature axial radial distribution: comparison w/ and w/o new radial model.

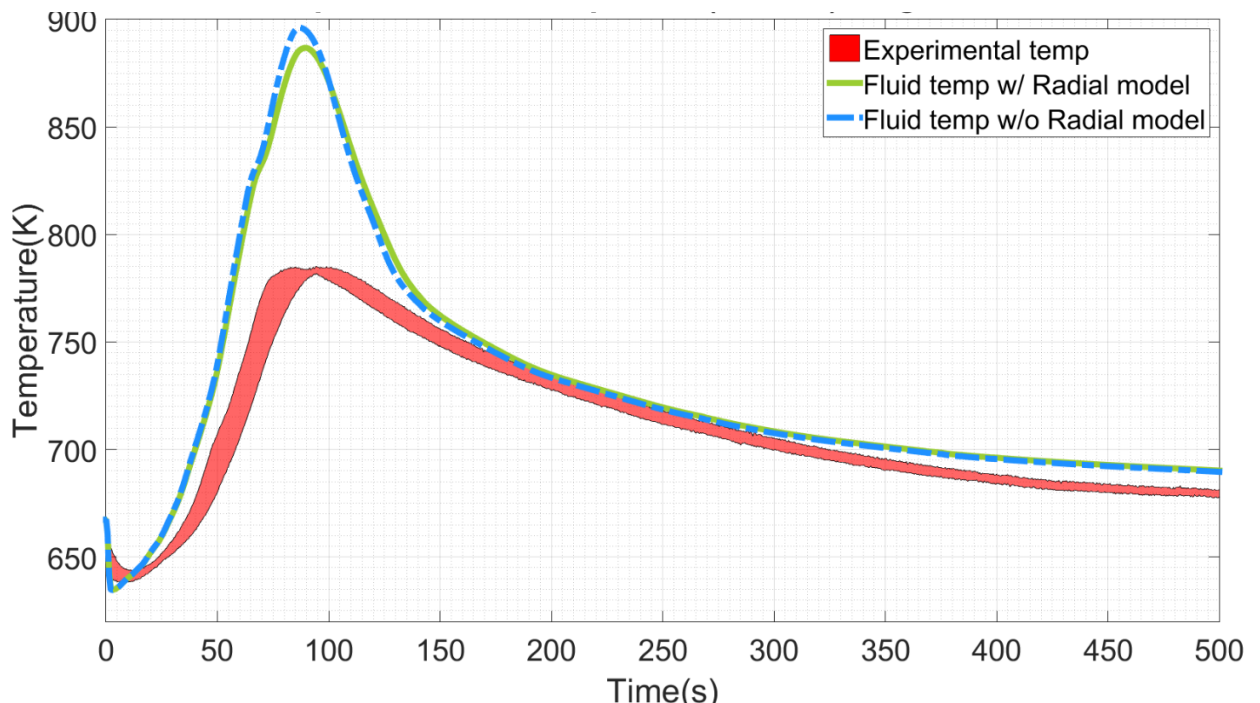


Figure 46. XX10 temperature evolution at Top-of-Core ($z = 0.322$ m): comparison w/ and w/o new radial model.

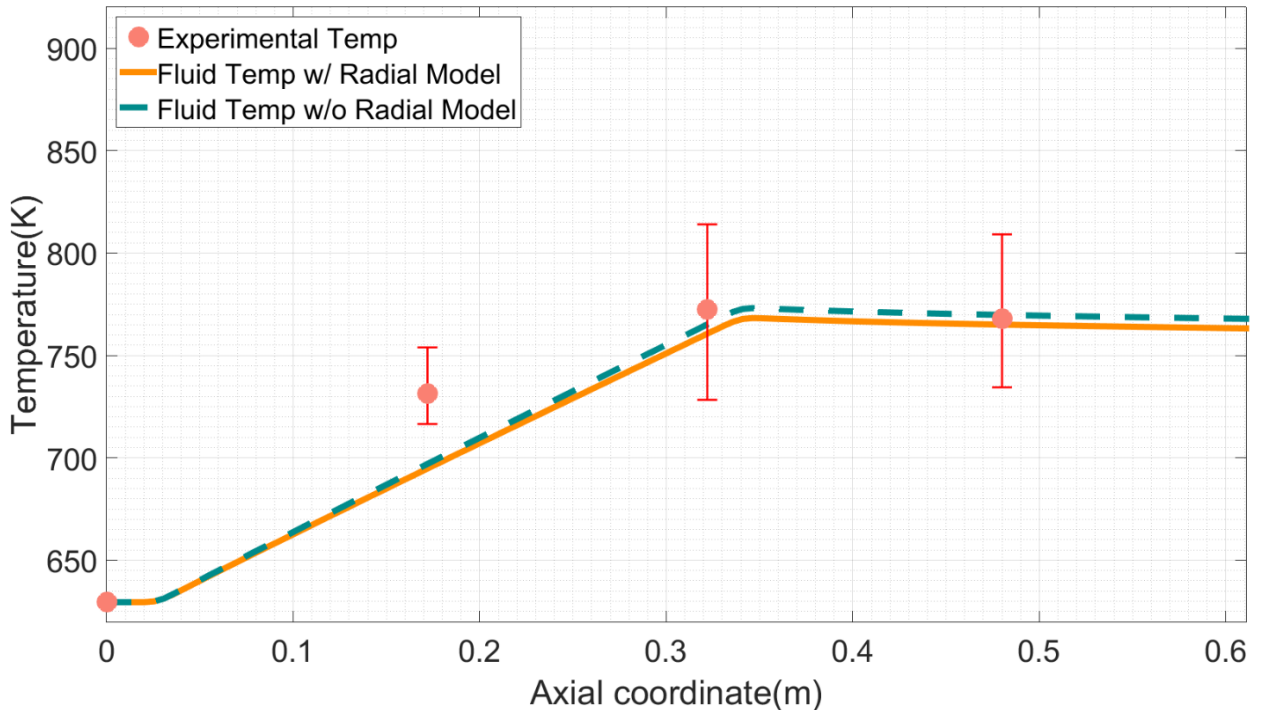


Figure 47. XX09 steady state temperature axial radial distribution: comparison w/ and w/o new radial model.

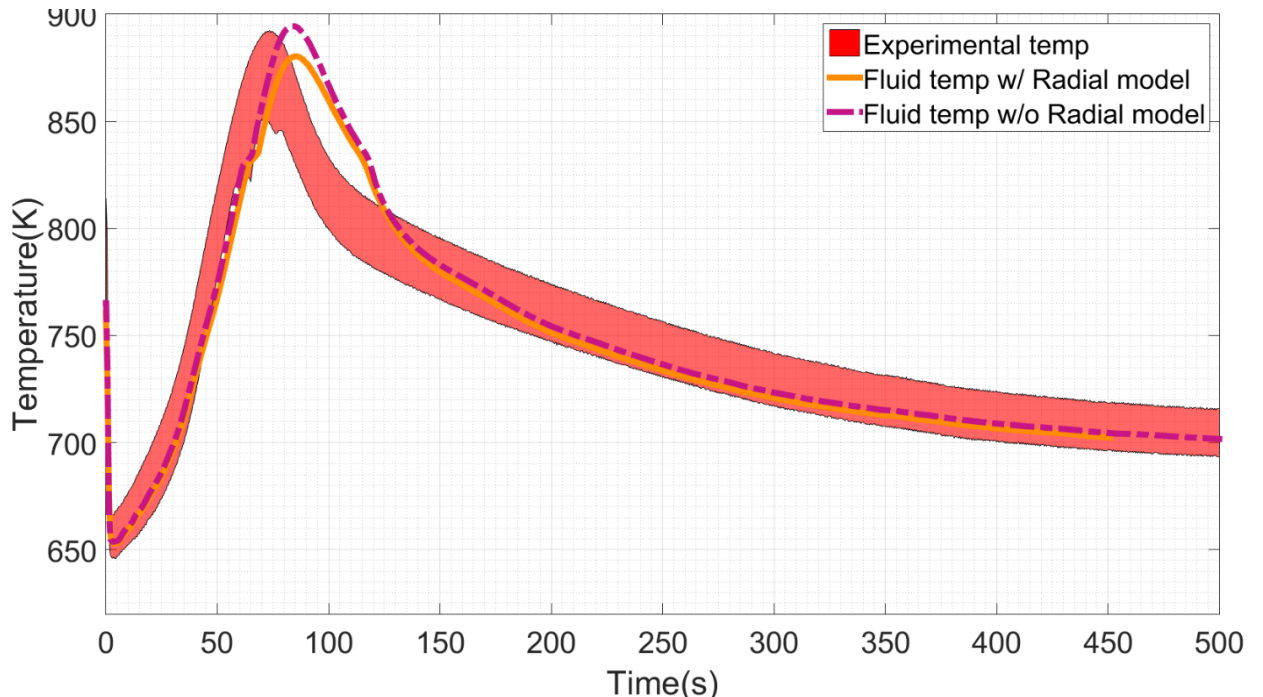


Figure 48. XX09 temperature evolution at Top-of-Core ($z = 0.322$ m): comparison w/ and w/o new radial model.

3.3 Conclusions

The capabilities of the thermal-hydraulic (TH) module of the FRENETIC code have been improved thanks to the addition of new features, such as the “Box-in-the-box” (BIB) and the Pin radial model, which better describe the heat transfer phenomena in the core.

The BIB model brought some improvements to the steady state condition of SHRT-17, while the contribution to the transient evolution was almost negligible. This has been explained with the fact the SHRT-17 is a “scrammed” transient: the absence of the driver leads to a temperature redistribution inside the core that brings neighboring assemblies to be almost in equilibrium during the transient phases, therefore making the presence of the flow in the thimble not a relevant parameter for the analysis. Anyhow the BIB model may be an improvement for those full power transients in which neighboring assemblies will set on different temperature fields depending on the entity of the power deposited.

The radial model, conceived to align the FRENETIC code with current experience and tradition in affirmed fission codes, was shown to have a little impact on foreseeing the coolant temperature due to the fact that the conservation of energy was already achieved in the previous simplified model, but positively affects the quality of the computed average and maximum fuel temperature. The latter is a fundamental parameter to assess the gravity of a nuclear accident and therefore needs accurate prediction by codes.

4 Development of the neutronic module

4.1 Introduction

The neutronic module of the FRENETIC code employs a coarse mesh nodal method to solve the multigroup neutron diffusion equations both for direct and adjoint problems, as well as direct, quasi-static and point kinetics solvers for dynamics problems. In this report, the development and the implementation of additional physics models in the code is documented. The first of which is a model for the decay heat, allowing to account for the time-delay associated with variations of the fission power. Particular attention is given to the development and the implementation of a method of solution for the relevant equations in order to be able to use the decay heat model together with a quasi-static solver.

4.2 Decay heat model and methods of solution

Accounting for the phenomenon of the decay heat, the system of equations which describe the spatial-temporal evolution of the instantaneous fission power density and the concentration of decay heat precursors may be written as

$$\begin{cases} p(\mathbf{r}, t) = (1 - \gamma)\Psi_p(\mathbf{r}, t) + \sum_{i=1}^{R_d} \mu_i d_i(\mathbf{r}, t) \\ \frac{\partial}{\partial t} d_i(\mathbf{r}, t) = \gamma_i \Psi_p(\mathbf{r}, t) - \mu_i d_i(\mathbf{r}, t), \quad i = 1, \dots, R_d, \end{cases} \quad (17)$$

where $d_i(\mathbf{r}, t)$ is the concentration of decay heat precursors in decay heat family i , μ_i is the decay constant of decay heat family i , γ_i is the fraction of the energy produced by fission that appears as decay heat in the decay heat family i such that $\gamma \equiv \sum_{i=1}^{R_d} \gamma_i$ and R_d is the total number of decay heat precursors families. The total fission power density is defined as

$$\Psi_p(\mathbf{r}, t) \equiv \int dE \oint d\Omega \varepsilon \Sigma_f(\mathbf{r}, E, t) \phi(\mathbf{r}, E, \boldsymbol{\Omega}, t), \quad (18)$$

with $\phi(\mathbf{r}, E, \boldsymbol{\Omega}, t)$ the angular neutron flux and $\varepsilon \Sigma_f(\mathbf{r}, E, t)$ the macroscopic cross section for fission energy production. Equations (17) are rendered complete by imposing appropriate initial conditions on the decay heat precursors concentrations, $d_i(\mathbf{r}, 0)$.

In general, Eqs. (17) are solved in a straightforward manner. Once the flux distribution is available, the fission power density becomes a known quantity. It remains then to integrate the decay heat precursors concentrations across the time step. Noting that the form is similar to that of the delayed neutron precursors balance equations, this operation becomes trivial as it may make use of the same techniques used to integrate those equations in whichever temporal integration method is considered (direct, quasi-static or point kinetic). In all cases, the starting point is the expression

$$d_i(\mathbf{r}, t_n + \Delta t_n) = d_i(\mathbf{r}, t_n) e^{-\mu_i \Delta t_n} + \\ + \gamma_i \int_{t_n}^{t_n + \Delta t_n} dt' \Psi_p(\mathbf{r}, t' - t_n) e^{-\mu_i(t_n + \Delta t_n - t')}, \quad (19)$$

which is obtained by directly integrating the second of Eqs. (17) across the time interval $[t_n; t_n + \Delta t_n]$. That which varies depending on the method is the treatment of the integrand.

In the direct solution method, the fission power density is assumed to vary linearly across the time step. Under this assumption, Eq. (19) yields an analytical expression of the form

$$d_i(\mathbf{r}, t_n + \Delta t_n) = d_i(\mathbf{r}, t_n) e^{-\mu_i \Delta t_n} + \\ + \frac{\gamma_i}{\mu_i} [\kappa_{1i} \Psi_p(\mathbf{r}, t_n) + \kappa_{2i} \Psi_p(\mathbf{r}, t_n + \Delta t_n)], \quad (20)$$

in which κ_{1i} and κ_{2i} are dimensionless expressions that depend on the quantity $\mu_i \Delta t_n$.

In quasi-static computations, the fission power density becomes the product of a shape function and an amplitude function, which is a direct consequence of the factorisation of the neutron flux into the product of two such functions. Thus, in order to evaluate the integral in Eq. (19), the time-dependent behaviour of both functions must be specified. Consistent with the quasi-static algorithms implemented in the code [9], the evolution of the amplitude is evaluated analytically on an interval in which the integral kinetics parameters are assumed constant and can therefore be written as the summation of a series of exponential functions whose coefficients depend on the eigenvalues and the eigenvectors of the system of amplitude equations. Likewise, the fission power density per unit amplitude is assumed to vary linearly across the time step. Under these assumptions, Eq. (19) again yields an analytical expression, namely

$$d_i(\mathbf{r}, t_n + \Delta t_n) = d_i(\mathbf{r}, t_n) e^{-\mu_i \Delta t_n} + \\ + \frac{\gamma_i}{\mu_i} [\alpha_{1i}(t_n) \kappa_{1i} \Psi_p(\mathbf{r}, t_n) + \alpha_{2i}(t_n) \kappa_{2i} \Psi_p(\mathbf{r}, t_n + \Delta t_n)], \quad (21)$$

where $\alpha_{1i}(t)$ and $\alpha_{2i}(t)$ are dimensionless expressions which depend on the eigenvalues of the amplitude equations, the eigenvectors of the amplitude equations, the decay heat precursor decay constant and the time step size.

In point kinetics computations, the same general approach as that used in the quasi-static approach is employed, however maintaining constant the fission power density across the time step (as well as throughout the entire computation), consistent with the fundamental hypothesis of the point kinetics method. This is achieved by setting $\Psi_p(\mathbf{r}, t_n) = T(t_n) \Psi_p(\mathbf{r}, 0) / T(0)$ and $\Psi_p(\mathbf{r}, t_n + \Delta t_n) = T(t_n + \Delta t_n) \Psi_p(\mathbf{r}, 0) / T(0)$ in Eq. (21), where $T(t)$ is the amplitude of the fission power density at time t .

4.3 Representative results

The behaviour of the decay heat model is assessed with an example transient evaluated with the neutronic module working in stand-alone mode. The test case involves a divergent transient applied to a two-dimensional slice of a critical reactor in hexagonal geometry and characterised

by cross sections typical of a fast spectrum system cooled by lead-bismuth eutectic. The geometry of the system under consideration is shown in Figure 49. Zero incoming partial current boundary conditions are imposed on all external surfaces. The five materials are described by three group diffusion theory parameters, six delayed neutron precursor families and six decay heat precursor families. A transient is initiated by the instantaneous movement of the control elements indicated in the figure, resulting in a step insertion of reactivity equal to +169.2 pcm compared to an effective delayed neutron fraction of 356.5 pcm.

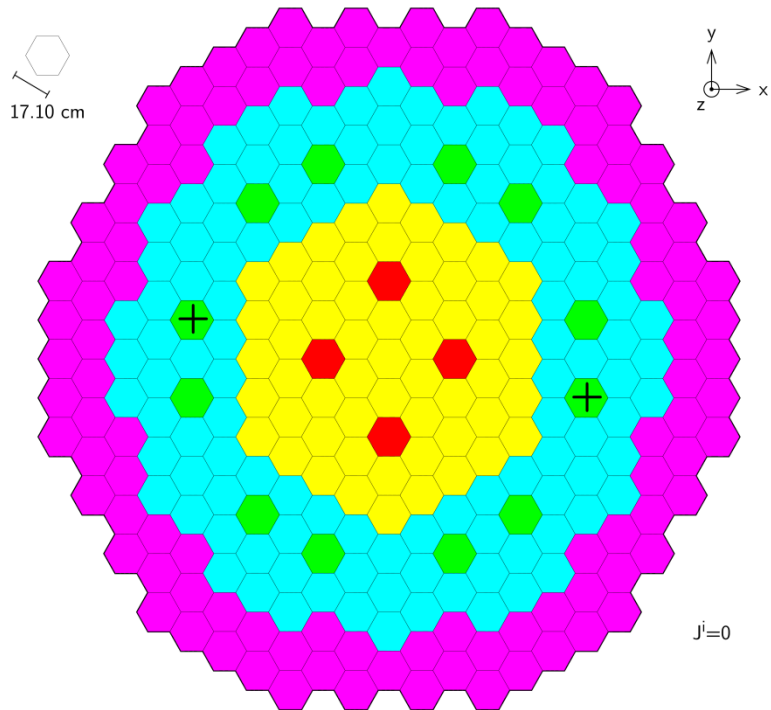


Figure 49. Configuration of the system analysed to assess the decay heat model. The transient is initiated by applying an instantaneous perturbation to the cross sections of the nodes marked with a "+".

The temporal evolution of the total and decay power for the first ten seconds of the transient is shown in Figure 50, both for the cases with and without consideration of the decay heat. For this transient consisting of a positive reactivity insertion, the inclusion of the decay heat phenomenon results in an instantaneous total power that is comparatively less than in the case when it is not considered, due to the accreditation of a part of the total energy generated by fission that is released later in time. As the transient progresses, the fraction of the instantaneous total power which is due to decay heat tends to an asymptotic value which itself is related to the relative rates at which the neutron flux is evolving and the decay heat precursors are decaying.

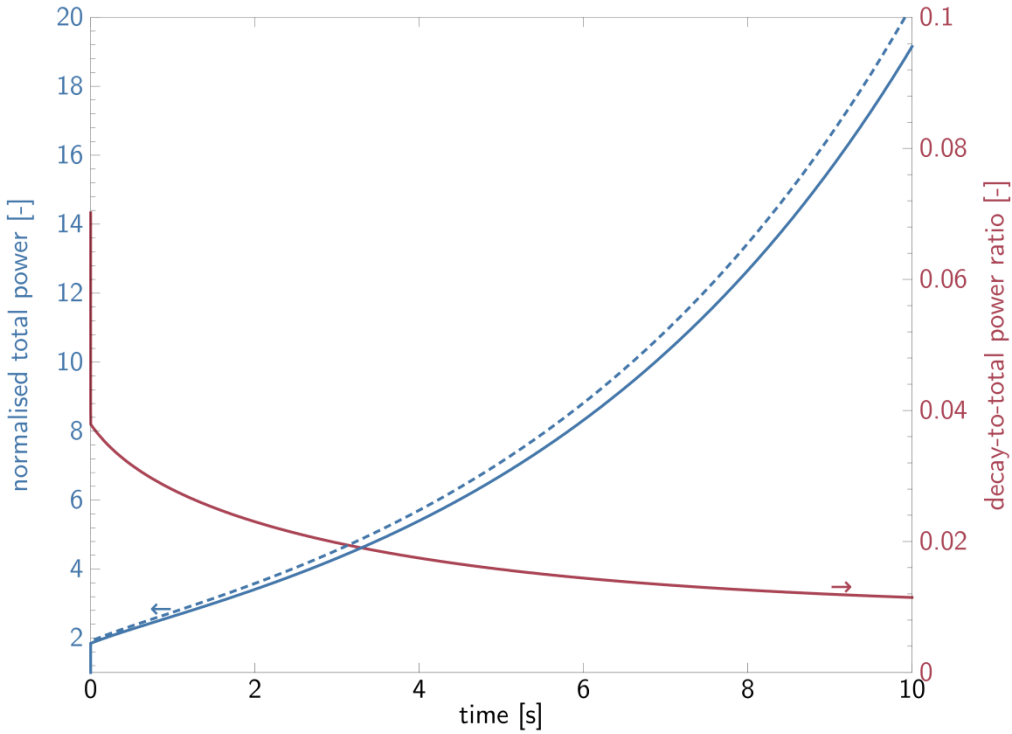


Figure 50. Temporal evolution of the total power and decay power in scenarios in which decay power is considered (solid line) and neglected (dashed line).

The validity of the proposed method for the integration of the power equations in the context of a quasi-static method is assessed through a comparison with the results obtained by a direct solution of the system of neutron flux and delayed neutron precursors balance equations followed by the direct integration of the power equations themselves, both processes using a fine discretisation of the time domain. Although other algorithmic variants are implemented in the code, only the predictor-corrector quasi-static method (PCQM) is selected for demonstration due to its superior accuracy [23]. Moreover, due to the relatively long time scales involved (compared to the effective neutron lifetime of $4.0199 \cdot 10^{-7}$ s), an adaptive time step selection algorithm [9] is employed with the quasi-static method. Results are summarised in Table 2. It is observed that, provided the limitation on the allowed distortion of the shape across a shape time step is restricted, thus assuring the accuracy of the solution of the neutron flux, the accuracy of any derived quantity, in this case the power, is guaranteed by the method as well.

Table 2. Comparison of results obtained by the direct integration and the quasi-static integration methods:
 ξ_ψ : maximum allowed distortion of the shape across a shape time step; $p(t)$: total power; $p_d(t)$: decay power.

t [s]	direct ($\Delta t=5 \cdot 10^{-8}$ s)		$PCQM (\xi_\psi=10^{-3})$		$PCQM (\xi_\psi=10^{-4})$	
	$p(t)/p(0)$ [-]	$p_d(t)/p(t)$ [-]	$p(t)/p(0)$ [-]	$p_d(t)/p(t)$ [-]	$p(t)/p(0)$ [-]	$p_d(t)/p(t)$ [-]
0.000	1.0000e+00	7.0160e-02	1.0000e+00	7.0160e-02	1.0000e+00	7.0160e-02
0.001	1.8390e+00	3.8042e-02	1.8178e+00	3.8491e-02	1.8363e+00	3.8098e-02
0.010	1.8554e+00	3.7718e-02	1.8553e+00	3.7719e-02	1.8554e+00	3.7718e-02
0.100	1.9361e+00	3.6265e-02	1.9361e+00	3.6265e-02	1.9361e+00	3.6265e-02
0.200	2.0208e+00	3.4880e-02	2.0208e+00	3.4880e-02	2.0208e+00	3.4880e-02
0.300	2.1019e+00	3.3677e-02	2.1019e+00	3.3676e-02	2.1019e+00	3.3676e-02
0.400	2.1803e+00	3.2610e-02	2.1803e+00	3.2610e-02	2.1803e+00	3.2610e-02
0.500	2.2569e+00	3.1652e-02	2.2569e+00	3.1651e-02	2.2569e+00	3.1651e-02

4.4 Conclusions

A decay heat model has been implemented in the neutronic module of the FRENETIC code. Representative results demonstrate functionality which is consistent between the direct inversion method and the quasi-static method in autonomous computations.

5 Preliminary validation of the coupled modules of FRENETIC

In order to demonstrate the capability of the FRENETIC code to correctly simulate a coupled neutronic/thermal-hydraulic transient, a preliminary study on the SHRT-45R of EBR-II has been performed. The SHRT-45R test was a test conducted after the SHRT-17 where the protection system of the EBR-II (the SCRAM procedure) was disabled. The goal of this unprotected test was to demonstrate the capability of the reactor to safely shutdown through feedback effects, as a consequence of a simulated LOFA of the primary pumps.

To correctly simulate the relationship between cross sections and temperature, a library of cross sections has been developed at various temperatures to be used with the tabular feedback model of the FRENETIC neutronic module. The library of cross sections was built using the continuous energy Monte Carlo transport code Serpent [24]. To simplify the simulation in terms of computational resources, a homogenization in the spatial domain was made, while in the energy domain the spectrum was collapsed into six groups. Due to the high level of heterogeneity of the core, the spatial homogenization was made taking into account the characteristics of geometry and composition of drivers. The procedure was optimized with a final number of 17 homogenized materials in cylindrical shape (including an axial division), preserving the volume of the original hexagonal domain (see Figure 51).

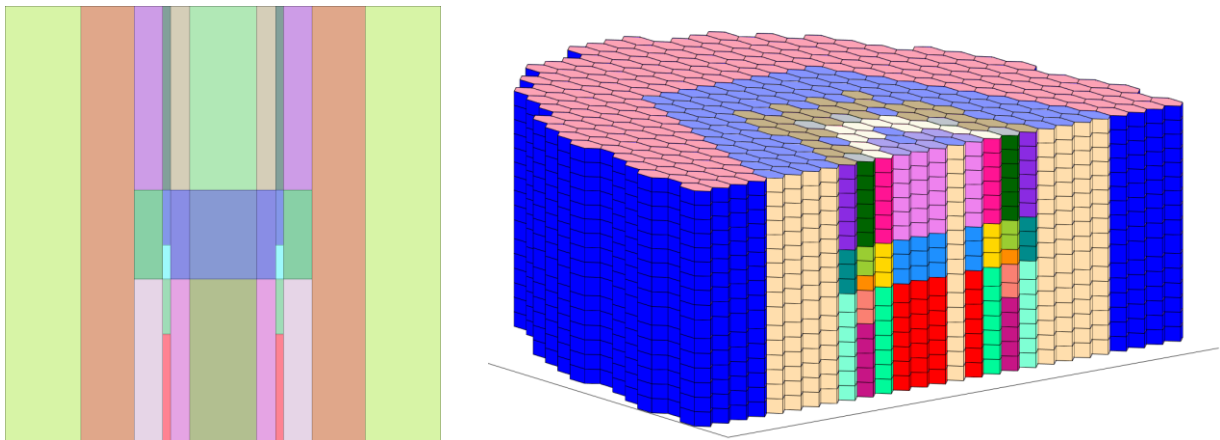


Figure 51. Left: Serpent model in cylindrical geometry with specific axial divisions. Right: FRENETIC mesh in hexagonal geometry with the same spatial division of transport model.

With this model, stationary transport simulations were made changing the temperatures of the fuel, coolant and structural materials, with the condition of coolant temperature lower or equal than fuel temperature. Three points along each temperature axis (that of the fuel, T_f , and that of the coolant, T_c) were selected for evaluation, resulting in a total of six discrete combinations of fuel and coolant temperatures, (T_f, T_c). Although multiple points were computed, an analysis of the resulting data confirmed that the variation of the macroscopic cross sections with respect to each of the individual temperatures was more or less linear.

On the side of the TH module, a proper set of boundary conditions has been prepared according to experimental data. In particular, conditions were imposed on the inlet coolant temperature, the outlet coolant pressure and the coolant flow rates in each hexagonal assembly.

For the inlet temperatures of the coolant, a reasonable hypothesis has been made. They are taken to be uniform for all the assemblies that receive sodium from the same plenum (high pressure for the core and low pressure for reflector/blanket), and they are taken equal to the experimental average temperature of the plena coming from the post-blind phase ANL experimental results.

The outlet pressure has been taken to be equal to the average of the outlet pressures from SHRT-17. This assumption is the weakest one, but it must be reminded that in a LMFBR the pressure of the plays a negligible role.

For the flow rates, the approach has been to scale the steady state distribution provided in the benchmark specification, which is computed by the EBRFLOW code prior to performing the experiment, as follows:

$$\dot{m}_{in,i}(t) = \dot{m}_{in,i}(t=0) \frac{\dot{m}_{pump\#2,exp}(t)}{\dot{m}_{pump\#2,exp}(t=0)} \quad (22)$$

where $\dot{m}_{in,i}$ is the inlet flow rate of the i -th HA and $\dot{m}_{pump\#2,exp}(t)$ is the experimental pumps flow rate provided by ANL in the post-blind phase of the Benchmark. The assumption laying at the base of this approximation is that the ratio between the flow rate entering the i -th HA and the flow rate processed by pump 2 (which feeds the high-pressure plenum) is constant in time. The boundary conditions are summarised in Figure 52.

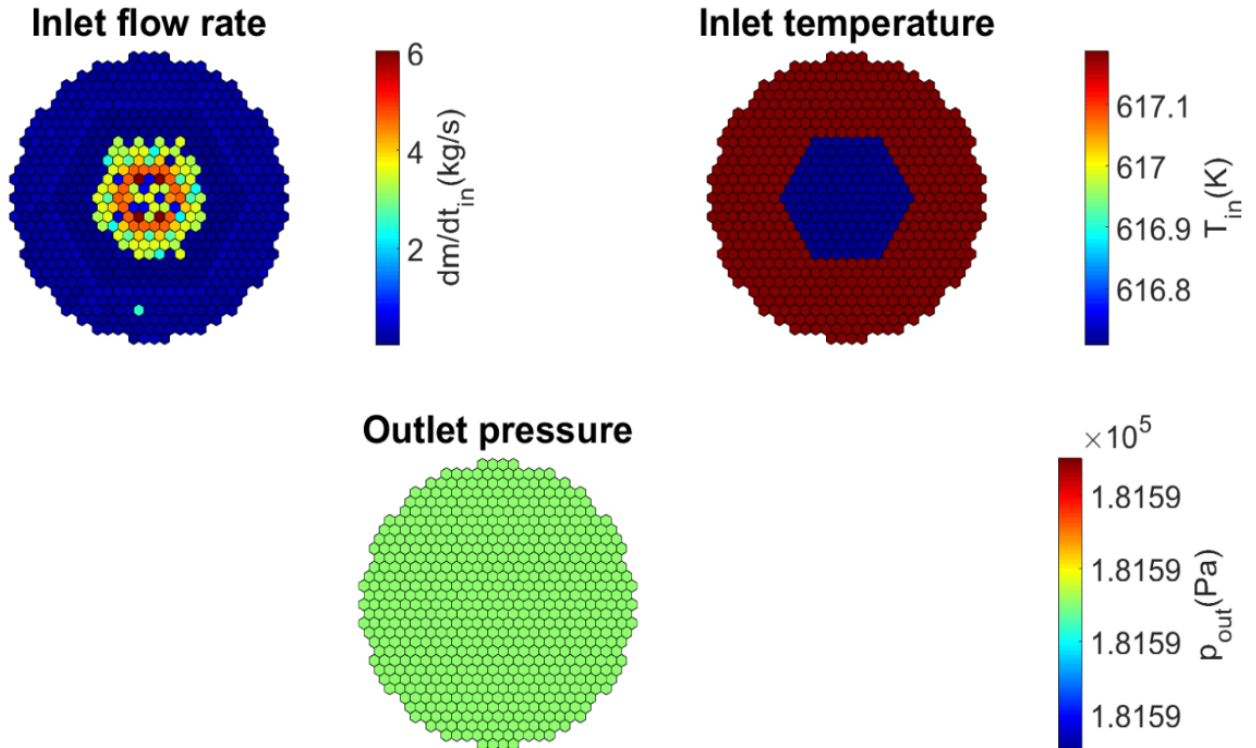


Figure 52. Imposed boundary conditions of the SHRT-45R transient.

5.1 Steady state analysis

The two modules work using different computational meshes, based on solution methods used. The NE module, which uses a nodal method in hexagonal geometry, used an axial division of

approximately 10 cm, although this number may vary slightly by axial region as the node interfaces of the axial mesh in FRENETIC are selected to correspond to the interfaces of the homogeneous materials generated in the Serpent computations. Instead, the TH module, which is based on a finite element solver, required a finer mesh of approximately 0.5 cm. Consequently, the relevant physical quantities generated by each module (power by the NE module and temperatures by the TH module) are redistributed as required on the mesh of the receiving module.

The error check on the solution for the individual modules is done by checking each spatial error for each module. So each interaction happens when the error on the parameter (thermal power or temperatures) becomes lower a certain tolerance. The following convergence criteria were imposed:

On the NE solution there are:

- Relative error on the spatial distribution of the lux: 10^{-5} ;
- Relative error on the eigenvalue: 10^{-6} ;

On the TH solution there are:

- Relative error on temperature distribution: $5 \cdot 10^{-4}$;
- Internal error check to reach the thermal equilibrium: 10^{-6} ;

In addition to the error control for each module, the coupled calculation is ruled by other tolerances that are used to find the steady state solution before to start the transient simulation. In particular:

- Relative error on temperature distribution: 10^{-3} ;
- Relative error on power distribution: 10^{-5} ;
- Relative error on the eigenvalue: 10^{-5} ;

The solution in steady state has been compared with the results of ANL.

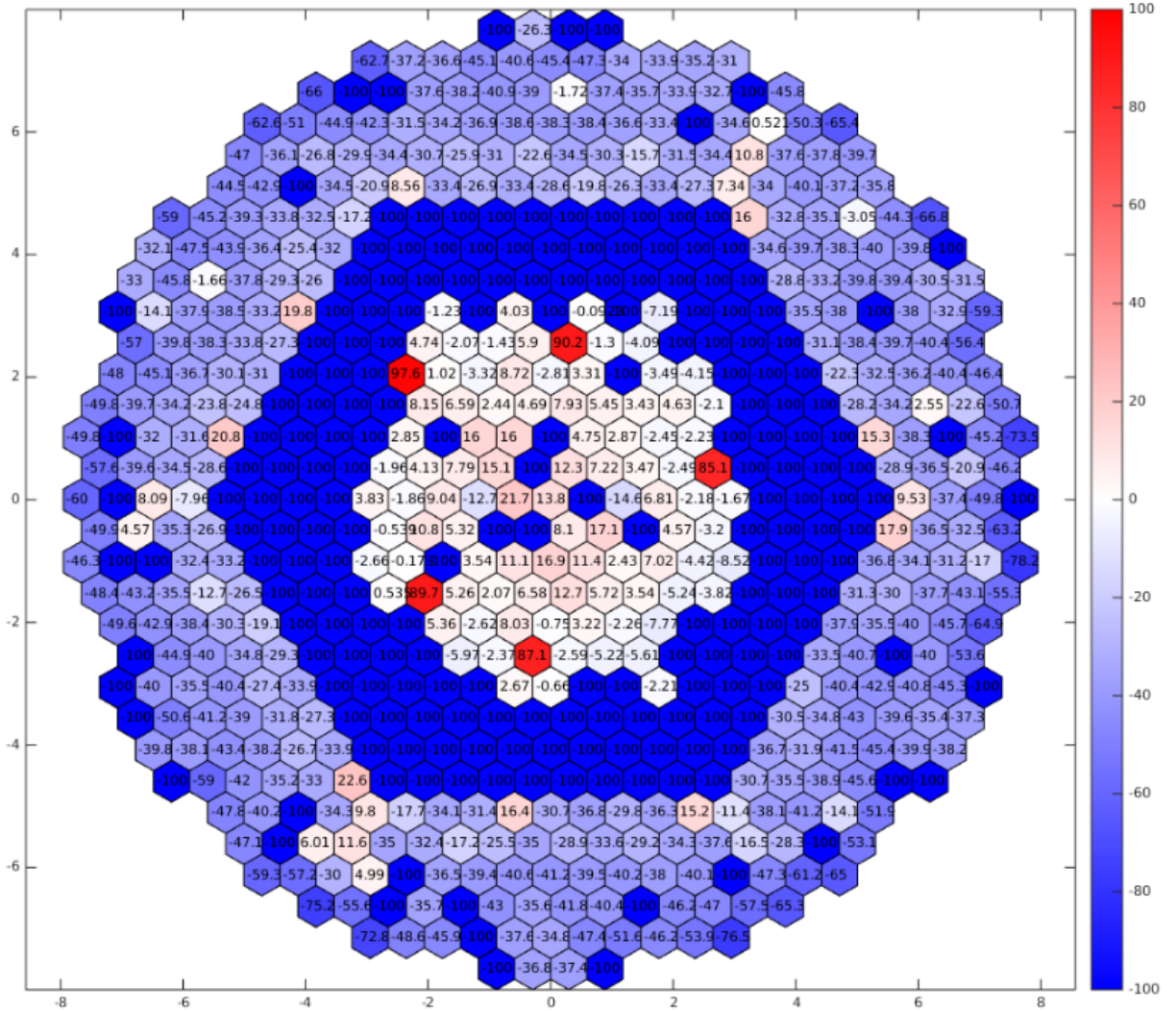


Figure 53. Steady state power distribution in the EBR-II core with FRENETIC compared with the calculation of the ANL full core simulation.

The overall result is good, even if there are errors due to the procedure of the cross sections library in transport calculation. To simplify the transport calculation, a homogenization of materials has been conducted. These approximation are clearly visible in the five drivers in the outer region of the Inner Core (see Figure 54), because in the real situation those assemblies were partial fuel driver (half load of fuel respect others). However, the maximum error in the Inner Core on a nominal fuel driver is almost 20%. The great error in the external reflectors and in the blanket is due to the unavailability, at the moment, of a gamma heat module in the NE module. Consequently, the power calculated in the external regions (radial reflector and blanket) is lower than the real situation where thermal effects of scattering and absorption are present.

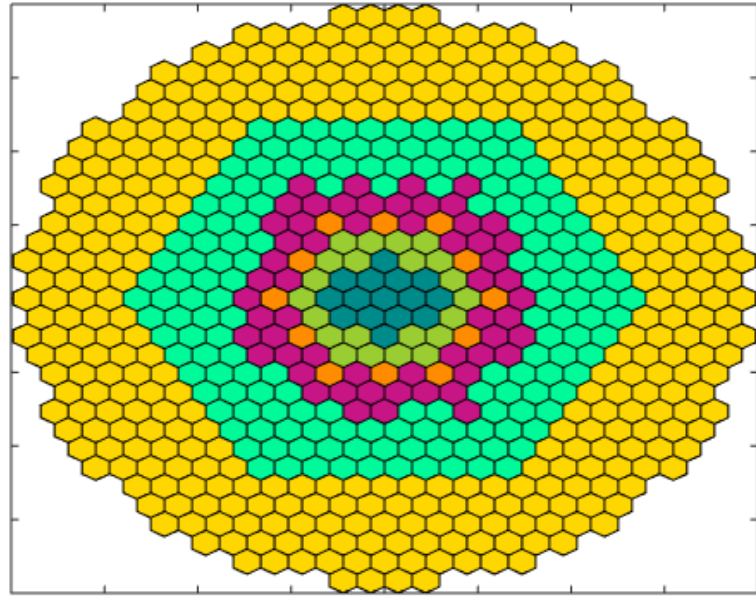


Figure 54. Radial zones. From centre: inner core, medium core, control region, outer core, radial reflector and blanket.

A comparison of the computed coolant temperature distribution with the experimental data in the instrumented assemblies XX09 and XX10 at steady state is shown in Figure 55.

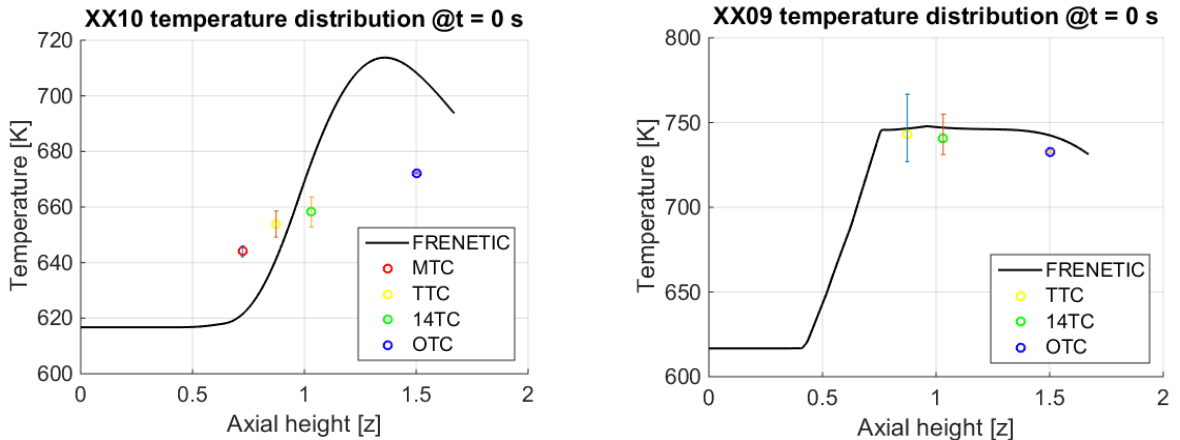


Figure 55. Comparison of computed results and experimental measurements in instrumented assemblies XX10 (left) and XX09 (right) at steady state.

The XX10 presents a great discrepancy as consequence of the impossibility to model the heat of gamma rays, so this assembly is modelled as a reflector assembly where neighbouring drivers provide the heating. Moreover, the presence of heated drivers in its proximity provides more thermal power than the real situation, thanks to the presence of colder sodium in the XX10 driver. For the XX09 the quality is higher because it is a heated assembly, so the cross sections evaluated with Serpent are more similar to the real ones, if compare to the XX10 ones, where the heat is zero. It has to be noted that for this assembly the thermocouple named MTC is switched off so the measurements are available only on the top of the heated region.

5.2 Transient results

A first calculation was made using a point-kinetic algorithm for the dynamic analysis. The choice of the lowest level of resolution was considered good by the nature of the transient itself: could be considered as a reduction of the amplitude of the neutron flux, whereas the shape could

be considered constant in space. After a steady state analysis, the evolution of thermal power has been considered. Among the available experimental data for this comparison there is only the fission thermal power, so the decay heat generation is not considered in the FRENETIC simulation.

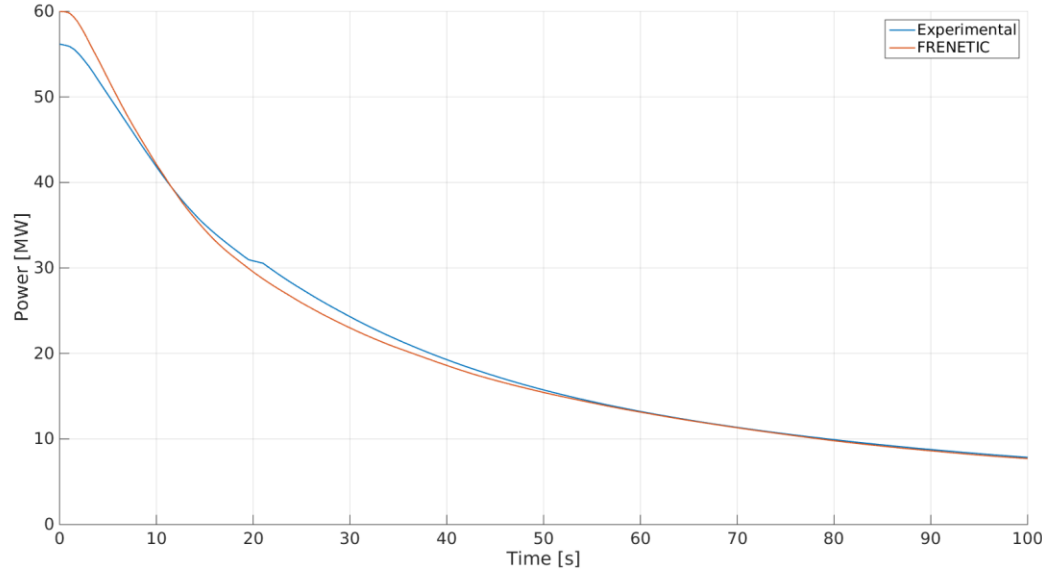


Figure 56. Power evolution in the EBR-II core computed with FRENETIC compared to experimental data (only fission thermal power).

The results are very good because, integrally speaking, the homogenization of cross sections does not introduce strong error since the materials and reaction rate are conserved.

Regarding the reactivity evolution, information of experimental measurements is not available. So a preliminary behaviour is shown, calculated by the NE module, in Figure 57.

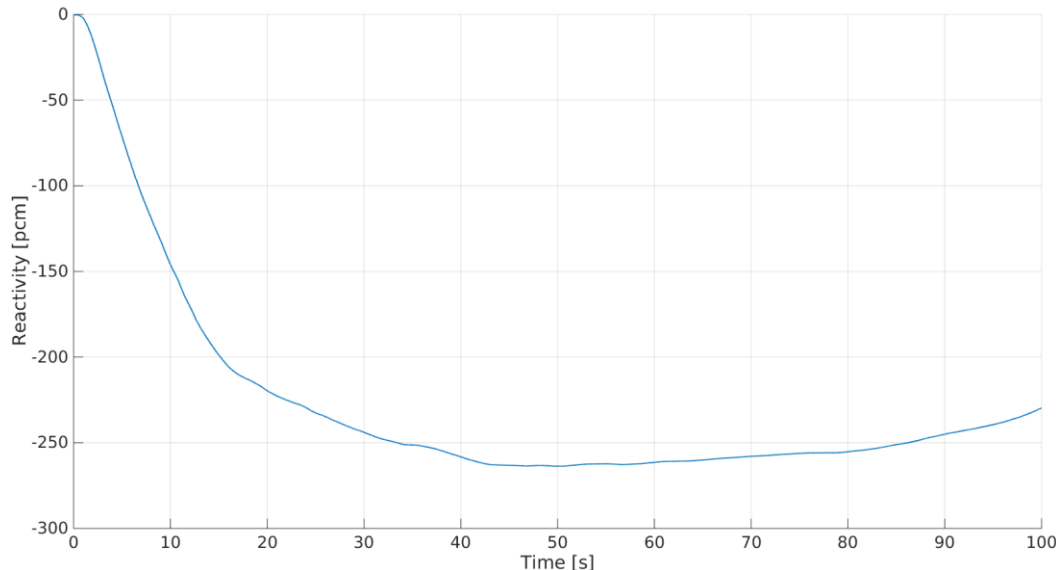


Figure 57. Reactivity evolution in the EBR-II core computed with FRENETIC.

Considering the evolution of coolant temperature inside the XX09 HA, the effects of homogenization are clearly visible (see Figure 58).

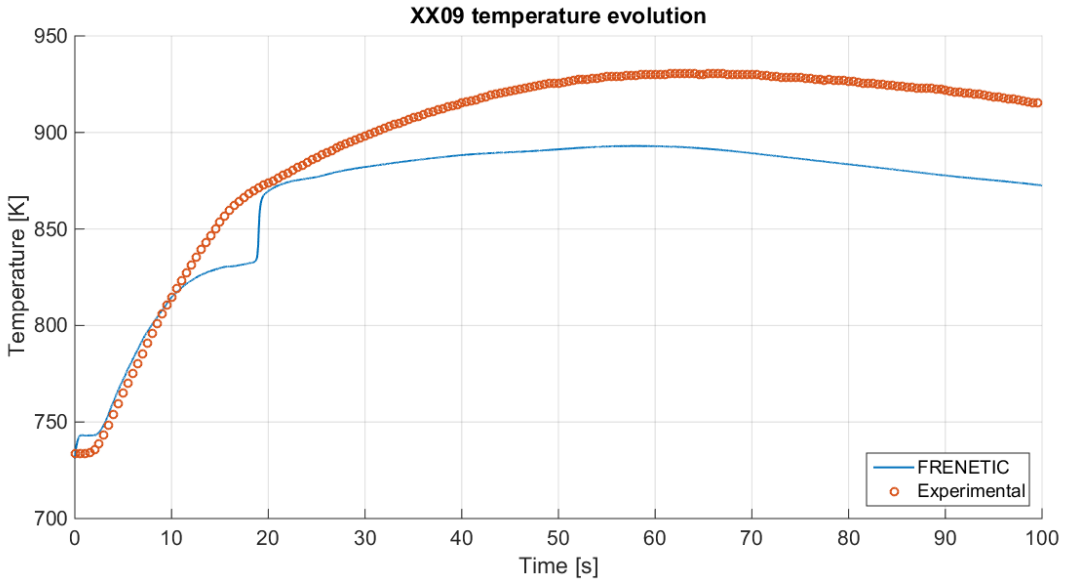


Figure 58. Coolant temperature evolution in XX09 at outlet of driver. Comparison with experimental measurements.

The fission reaction rate is, in fact, lower than the real situation because the homogenization decreases the real material density (and the flux). This implies a lower thermal power during the transient, which is visible in an underestimation of the temperature. However, the steady state distribution of power shows the thermal power is overestimated in the first part of the transient. In fact, for the first 10 seconds, the sodium temperature is greater than the measurement. After the first 10 seconds, the trend of the evolution is captured: this is connected to good approximation of the heated drivers, because the relative error is lower with respect a cold driver. In fact, the effect of non-heating driver is clearly visible in Figure 55 where the steady state distribution is very different with respect to the experimental data: the heat transfer becomes more powerful because the difference of temperature is higher, whereas in reality there is a little thermal power generated which influences the thermal distribution of coolant.

5.3 Parametric study with the quasi-static method

The point kinetic equations are the lowest level of approximation for the dynamics of nuclear reactors. Therefore, to take into account the effects of shape changing together with the amplitude variation, a quasi-static algorithm may be used. The study has been conducted with the predictor-corrector quasi-static method for the first 10 seconds of the transient, in order to demonstrate the convergence of the solution with several shape time steps. Moreover, the capability to model a LOFA with the point kinetic equations is proved by the numerical confirmation with respect to quasi-static simulations. Results of the evolution of the total power are shown in Figure 59 and in Table 3.

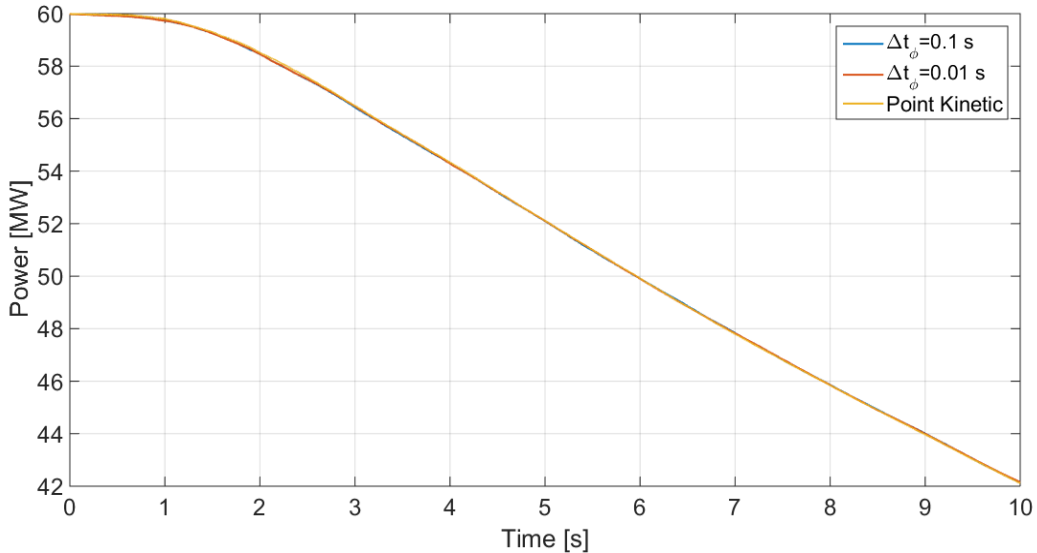


Figure 59. Total power computed by point kinetic and quasi-static algorithms for first 10 s of the transient.

Table 3. Total power computed by point kinetic and quasi-static algorithms for first 10 s of the transient.

Algorithm	Time									
	1 s	2 s	3 s	4 s	5 s	6 s	7 s	8 s	9 s	10 s
PK [MW]	59.80	58.52	56.49	54.34	52.12	49.92	47.80	45.85	43.97	42.11
QS ($\Delta t_\phi = 10^{-1}$ s) [MW]	59.73	58.45	56.44	54.29	52.10	49.91	47.83	45.86	44.01	42.14
QS ($\Delta t_\phi = 10^{-2}$ s) [MW]	59.73	58.46	56.47	54.29	52.10	49.90	47.83	45.85	44.00	42.15

To understand the sensibility of the solution with respect to the variation of the shape, two different shape time steps were adopted: one of 0.1 seconds and 0.01 seconds. The variation among the three simulations is negligible: the reduction of amplitude due to feedbacks is much larger than the shape change, so the results with quasi-static methods was in according with the hypothesis of point kinetic time algorithm. With these hypothesis, the behaviour on 10 seconds, can be extended to the total length of transient, since the effects of shape is negligible.

The reactivity presents a similar trend, as seen in Figure 60 and in Table 4.

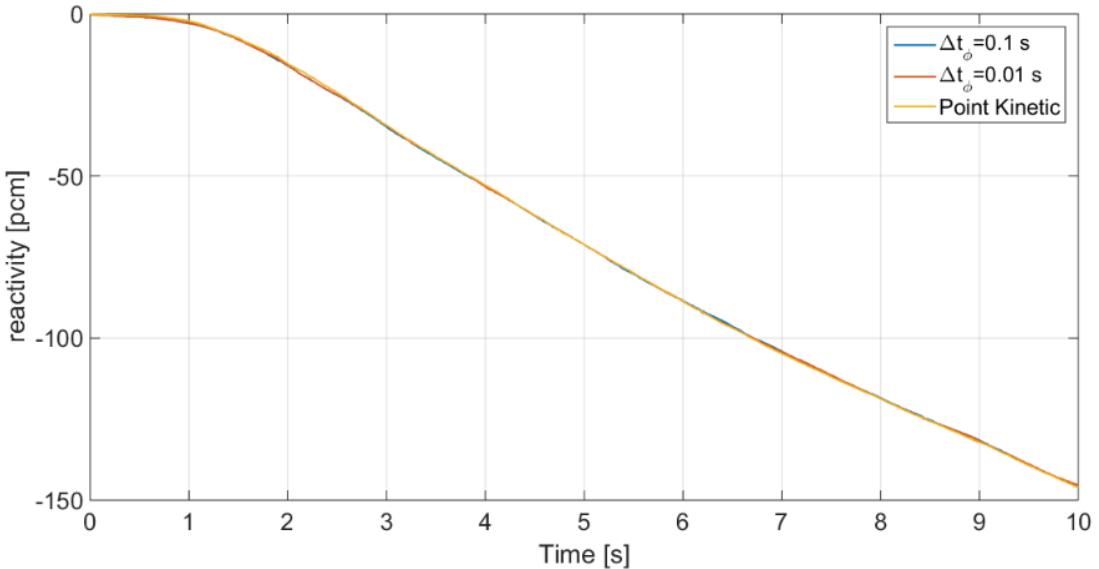


Figure 60. Reactivity computed by point kinetic and quasi-static algorithms for first 10 s of the transient.

Table 4. Reactivity computed by point kinetic and quasi-static algorithms for first 10 s of the transient.

Algorithm	Time									
	1 s	2 s	3 s	4 s	5 s	6 s	7 s	8 s	9 s	10 s
PK [pcm]	-2.2	-15.4	-34.4	-52.9	-71.2	-88.6	-104.8	-118.7	-132.1	-146.0
QS ($\Delta t_\phi = 10^{-1} \text{ s}$) [pcm]	-2.9	-16.0	-35.0	-52.9	-71.2	-88.5	-104.1	-118.5	-131.6	-145.6
QS ($\Delta t_\phi = 10^{-2} \text{ s}$) [pcm]	-2.9	-15.9	-34.5	-52.9	-71.2	-88.7	-104.2	-118.7	-131.7	-145.3

On the TH framework, a comparison on two assemblies with a small relative error on power generation has been performed. The partial driver 01A01 situated in the centre of the core has been compared with experimental measurements made at the outlet of the HA. The same approach has been adopted for a full driver 04C03 located near the neutron shield. Results are presented in Figure 61. This study demonstrates how the error on the power results in non-negligible effects on the temperature of the coolant since the homogenization affects the fission rate. In fact, the error changes from 13% to 3%, showing how the temperature is overestimated. The flow rates error does not contributes in significant way because the hypothesis on the trend is consistent with the experimental behaviour.

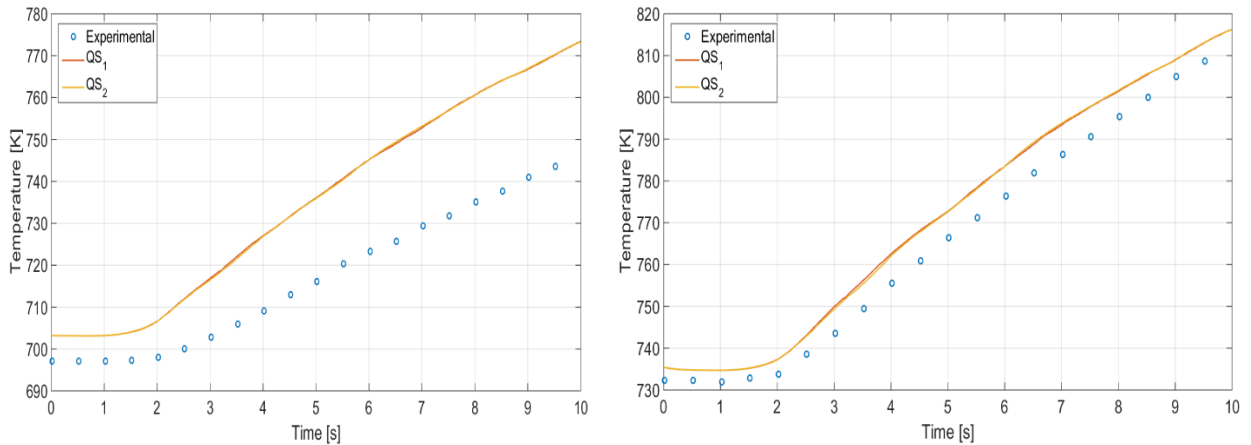


Figure 61. Coolant temperature evolution in 01A01 (left) and 04C03 (right) for different simulation in quasi static. Comparison with experimental measurements.

5.4 Conclusions

The preliminary analysis conducted on the SHRT-45R with the FRENETIC code shows promising results. The approximations are introduced by the transport simulation due to the spatial homogenization since where cross sections are closer to the real ones, the code is able to reproduce the real behaviour of the temperature. The capability of FRENETIC to simulate the transient, compared with other experimental data, are promising: even if the power generation was affected by the inaccuracy due to homogenization in transport calculation, the distribution of temperature inside the instrumented assemblies were under the safety limit foreseen by the experimental results. Moreover, the phenomena were well described by the thermal-hydraulic model during the transient. Finally, to better improve the quality of the simulation for the benchmark on the SHRT, a solution could be a complete full core simulations with Serpent to generate cross sections for each assemblies (or a representative one for similar ones) in hexagonal geometry, preserving as much as possible the heterogeneity in space.

6 Conclusions

In the areas of development and validation of the FRENETIC code, progress has been made during this year activity. The thermal-hydraulic module is furnished with two new models: the first better models the box-in-the-box geometry for hexagonal assemblies while the second explicitly describes the radial conduction of heat in the fuel pins. Both contribute improvements in their own respects. A model for decay heat is implemented in the neutronic module, thus allowing it to describe the time delay that accompanies variations in the fission power. As an overall code, FRENETIC is undergoing validation for coupled neutronic/thermal-hydraulic transients in the framework of a coordinated research project of the International Atomic Energy Agency which focuses on modelling the shutdown heat removal tests of the Experimental Breeder Reactor-II reactor. Results thus far obtained, although preliminary, demonstrate that the code is capable of describing the evolution of the power and the temperatures of the reactor during the transient.

7 References

- [1] USDOE Nuclear Energy Research Advisory Committee and the Generation IV International Forum, "A Technology Roadmap for Generation IV Nuclear Energy Systems," GIF-002-00, 2002. [Online]. Available: <http://www.gen-4.org/PDFs/GenIVRoadmap.pdf>. [Accessed 28 February 2013].
- [2] A. Alemberti, "The European lead fast reactor: design, safety approach and safety characteristics," Presented at the IAEA Technical Meeting on Impact of Fukushima Event on Current and Future FR Designs, Dresden, Germany, March 19-23, 2012. [Online]. Available: <http://www.iaea.org/NuclearPower/Meetings/2012/2012-03-19-03-23-TM-NPTD.html>. [Accessed 02 April 2014].
- [3] A. Alemberti, D. De Bruyn, G. Grasso, L. Mansani, D. Mattioli and F. Roelofs, "The lead fast reactor e demonstrator (ALFRED) and ELFR design," Presented at the International Conference on Fast Reactor and Nuclear Fuel Cycle (FR13), Paris, France, March 4-7, 2013. [Online]. Available: <http://www.iaea.org/NuclearPower/Meetings/2013/2013-03-04-03-07-CF-NPTD.html>. [Accessed 31 January 2014].
- [4] H. Aït Abderrahim, P. Baeten, D. De Bruyn and R. Fernandez, "MYRRHA – A multi-purpose fast spectrum research reactor," *Energy Conversion and Management*, vol. 63, pp. 4-10, 2012.
- [5] R. Bonifetto, S. Dulla, P. Ravetto, L. Savoldi Richard and R. Zanino, "A full-core coupled neutronic/thermal-hydraulic code for the modeling of lead-cooled nuclear fast reactors," *Nuclear Engineering and Design*, vol. 261, pp. 85-94, 2013.
- [6] R. Bonifetto, S. Dulla, P. Ravetto, L. Savoldi Richard and R. Zanino, "Progress in multi-physics modeling of innovative lead-cooled fast reactors," *Transactions of Fusion Science and Technology*, vol. 61, pp. 293-297, 2012.
- [7] R. Bonifetto, S. Dulla, P. Ravetto, L. Savoldi Richard and R. Zanino, "Full-Core Coupled Neutronic/Thermal-Hydraulic Model of Innovative Lead-Cooled Fast Reactors," *Transactions of the American Nuclear Society*, vol. 106, pp. 630-632, 2012.
- [8] R. Bonifetto, D. Caron, S. Dulla, P. Ravetto, L. Savoldi Richard and R. Zanino, *Extension of the FRENETIC code capabilities to the three-dimensional coupled dynamic simulation of LFR*, Madrid (Spain): Presented at the 16th International Conference on Emerging Nuclear Energy Systems (ICENES), May 26-30, 2013.
- [9] D. Caron, S. Dulla and P. Ravetto, "New aspects in the implementation of the quasi-static method for the solution of neutron diffusion problems in the framework of a nodal method," *Annals of Nuclear Energy*, vol. In press, 2015.
- [10] R. Zanino, R. Bonifetto, A. Ciampichetti, I. Di Piazza, L. Savoldi Richard and M. Tarantino, "First Validation of the FRENETIC Code Thermal-Hydraulic Model against the ENEA Integral Circulation Experiment," *Transactions of the American Nuclear Society*, vol. 107, pp. 1395-1398, 2012.
- [11] R. Zanino, R. Bonifetto, A. Del Nevo, E. Martelli and L. Savoldi Richard, "Thermal-hydraulic code-to-code benchmark in a simplified EBR-II geometry," *Transactions of the American Nuclear Society*, vol. 109, pp. 1759-1761, 2013.
- [12] R. Zanino, R. Bonifetto, A. Del Nevo and L. Savoldi, "Benchmark and preliminary validation of the thermal-hydraulic module of the FRENETIC code against EBR-II data," *Proceedings of the International Topical Meeting on Advances in Thermal Hydraulics (ATH), Reno, Nevada, 15-19 June 2014*, pp. 173-187, 2014.
- [13] T. Sumner and T. Wei, "Benchmark Specifications and Data Requirements for EBR II

- Shutdown Heat Removal Tests SHRT-17 and SHRT-45R,” Nuclear Engineering Division, Argonne National Laboratory, ANL-ARC-226 (Rev 1), 2012.
- [14] C. Westfall, “Vision and reality: The EBR-II story,” *Nuclear News*, vol. 47, no. 2, pp. 25-34.
- [15] T. Fei, A. Mohamed and T. Kim, “Neutronics Benchmark Specifications for EBR-II Shutdown Heat Removal Test SHRT-45R – Revision 1,” Nuclear Engineering Division, Argonne National Laboratory, ANL-ARC-228 (Rev 1), 2013.
- [16] D. Porter, G. Hofman, B. Seidel and L. Walters, “Factors controlling metal fuel lifetime,” in *International Conference on Reliable Fuels for Liquid Metal Reactors*, Tucson, Arizona, 7-11 September 1986.
- [17] J. Fink and L. Leibowitz, “Thermodynamic and Transport Properties of Sodium Liquid and Vapor,” ANL/RE-95/2, 1995.
- [18] “Experimental data released to participants to IAEA-CRP on EBR-II, unpublished, restricted,” Nuclear Engineering Division, Argonne National Laboratory.
- [19] The RELAP5-3D© Code Development Team, “RELAP5-3D© Code Manual Volume II: User’s Guide and Input Requirements,” INEEL-EXT-98-00834 Rev. 4.0, June 2012.
- [20] L. Savoldi Richard and R. Zanino, “M&M: multi-conductor mithrandir code for the simulation of thermal-hydraulic transients in super-conducting magnets,” *Cryogenics*, vol. 40, pp. 179-189, 2000.
- [21] T. Bergman, A. Lavine, F. Incropera and D. Dewitt, *Fundamentals of Heat and Mass Transfer*, John Wiley & Sons, 2012.
- [22] L. Savoldi Richard, F. Casella, B. Fiori and R. Zanino, “The 4C Code for the Cryogenic Circuit Conductor and Coil modeling in ITER,” *Cryogenics*, vol. 50, pp. 167-176, 2010.
- [23] S. Dulla, E. H. Mund and P. Ravetto, “The quasi-static method revisited,” *Progress in Nuclear Energy*, vol. 50, pp. 908-920, 2008.
- [24] J. Leppänen, *Development of a new Monte Carlo reactor physics code*, PhD Thesis, VTT Technical Research Centre of Finland, 2007.

8 Breve CV del gruppo di lavoro

Il gruppo di lavoro impegnato nell'attività opera presso il Dipartimento Energia del Politecnico di Torino ed è costituito da due professori ordinari (Piero Ravetto, fisica dei reattori nucleari e Roberto Zanino, impianti nucleari), due ricercatori confermati (Sandra Dulla, fisica dei reattori nucleari e Laura Savoldi, impianti nucleari), da un post-doc (Roberto Bonifetto) e da un dottorando (Dominic Caron) iscritto al II anno di Dottorato in Energetica.

Il gruppo ha una lunga esperienza nella ricerca nel campo dell'ingegneria nucleare, sia nel settore della fissione (S. Dulla e P. Ravetto) che nel settore della fusione (L. Savoldi e R. Zanino).

Nel settore della fissione l'attività ha riguardato lo sviluppo di metodi per il trasporto neutronico e per la dinamica dei reattori, in particolare per applicazioni ai sistemi nucleari avanzati (ADS e reattori innovativi). Nel settore della fusione il gruppo si è occupato dell'analisi termofluidodinamica di componenti di reattori a confinamento magnetico e in particolare dello sviluppo di codici per la modellazione del sistema dei magneti superconduttori e dell'applicazione di software CFD per l'analisi di blanket, first wall e vacuum vessel.

L'attività di Roberto Bonifetto comprende lo sviluppo e l'applicazione di codici per la modellazione di reattori nucleari a fissione (il codice presentato in questo lavoro) e a fusione (il codice 4C per l'analisi termofluidodinamica dei magneti superconduttori).

Nel lavoro presentato in questo rapporto sono state utilizzate le metodologie di simulazione termoidraulica messe a punto nel settore della fusione per lo sviluppo di un codice di multifisica per la dinamica di un reattore veloce refrigerato a piombo.

Maggiori dettagli e l'elenco delle pubblicazioni più recenti dei membri del gruppo si possono trovare sul sito Web del Politecnico di Torino:

<http://porto.polito.it/view/creators/Ravetto=3APiero=3A000919=3A.html>
<http://porto.polito.it/view/creators/Zanino=3ARoberto=3A001876=3A.html>
<http://porto.polito.it/view/creators/Dulla=3ASandra=3A011663=3A.html>
<http://porto.polito.it/view/creators/Savoldi=3ALaura=3A003575=3A.html>
<http://porto.polito.it/view/creators/Bonifetto=3ARoberto=3A026979=3A.html>